JWST Observations of Young protoStars (JOYS) Overview of program and early results

Citation for the original published paper (version of record):
van Dishoeck, E., Tychoniec, Ł., Rocha, W. et al (2025). JWST Observations of Young protoStars (JOYS) Overview of program and early results. Astronomy and Astrophysics, 699.
http://dx.doi.org/10.1051/0004-6361/202554444

A&A, 699, A361 (2025)
https://doi.org/10.1051/0004-6361/202554444

Astronomy & Astrophysics

JWST Observations of Young protoStars (JOYS)

Overview of program and early results

E. F. van Dishoeck[1,2,⋆], Ł. Tychoniec[1], W. R. M. Rocha[1,3], K. Slavicinska[1,3], L. Francis[1], M. L. van Gelder[1], T. P. Ray[4], H. Beuther[5], A. Caratti o Garatti[6], N. G. C. Brunken[1], Y. Chen[1], R. Devaraj[4], V. C. Geers[7], C. Gieser[5,2], T. P. Greene[8], K. Justtanont[9], V. J. M. Le Gouellec[8,10,11], P. J. Kavanagh[12], P. D. Klaassen[7], A. G. M. Janssen[1], M. G. Navarro[13], P. Nazari[14], S. Notsu[15,16], G. Perotti[5,17], M. E. Ressler[18], S. D. Reyes[5], A. D. Sellek[1], B. Tabone[19], C. Tap[1], N. C. M. A. Theijssen[1], L. Colina[20], M. Güdel[21,22], Th. Henning[5], P.-O. Lagage[23], G. Östlin[24], B. Vandenbussche[25], and G. S. Wright[7]

(Affiliations can be found after the references)

Received 10 March 2025 / Accepted 5 May 2025

ABSTRACT

Context. The embedded phase of star formation is a crucial period in the development of a young star when the system still accretes matter, emerges from its natal cloud with assistance from powerful jets and outflows, and forms a disk, thus setting the stage for the birth of a planetary system. The mid-infrared spectral line observations now possible with unprecedented sensitivity, spectral resolution, and sharpness from the *James Webb Space Telescope* (JWST) are key for probing many of the physical and chemical processes on sub-arcsecond scales that occur in highly extincted regions. They provide unique diagnostics and complement millimeter observations.

Aims. The aim of the JWST Observations of Young protoStars (JOYS) program is to address a wide variety of topics ranging from protostellar accretion and the nature of primeval jets, winds, and outflows to the chemistry of gas and ice in hot cores and cold dense protostellar environments to the characteristics of the embedded disks. We introduce the JOYS program and show representative results.

Methods. The JWST Mid-InfraRed Instrument (MIRI) Medium Resolution Spectrometer (MRS) Integral Field Unit (IFU) 5–28 μm maps of 17 low-mass targets (23 if binary components are counted individually) and six high-mass protostellar sources were taken with resolving powers $R = \lambda/\Delta\lambda$ = 1500–4000. We used small mosaics ranging from 1 × 1 to 3 × 3 MRS tiles to cover ~4″ to 20″ fields of view, providing spectral imaging on spatial scales down to ~30 au (low mass) and ~600 au (high mass). For HH 211, the complete ~1′ blue outflow lobe was mapped with the MRS. Atomic lines were interpreted with published shock models, whereas molecular lines were analyzed with simple rotation diagrams and local thermodynamic equilibrium slab models. We stress the importance of taking infrared pumping into account. Inferred abundance ratios were compared with detailed hot core chemical models including X-rays, whereas ice spectra were fit through comparison with laboratory spectra.

Results. The JWST MIRI-MRS spectra show a wide variety of features, with their spatial distribution providing key insight into their physical origin. The atomic line maps differ among refractory (e.g., Fe), semi-refractory (e.g., S), and volatile elements (e.g., Ne) and are linked to their different levels of depletion and local (shock) conditions. Jets are prominently seen in lines of [Fe II] and other refractory elements, whereas the pure rotational H_2 lines probe hot (~1000 K) and warm (few $\times 10^2$ K) gas inside the cavity, as well as gas associated with jets, entrained outflows, and cavity walls for both low- and high-mass sources. Wide-angle winds are found in low-J H_2 lines. Nested stratified jet structures containing an inner ionized core with an outer molecular layer are commonly seen in the youngest sources. While [S I] follows the jet as seen in [Fe II] in the youngest protostars, it is different in more evolved sources, where it is concentrated on source. Noble gas lines such as [Ne II] 12.8 μm reveal a mix of jet shock and photoionized emission. The H I recombination lines serve as a measure of protostellar accretion rates but are also associated with more extended jets. Gaseous molecular emission (CO_2, C_2H_2, HCN, H_2O, CH_4, SO_2, SiO) is seen toward several sources, but it is cool compared with what is found in more evolved disks, with excitation temperatures of only 100–250 K, and likely associated with the warm inner envelopes (“hot cores”) . Along the outflow, CO_2 is often extended, thus contrasting with C_2H_2, which is usually centered on source. Water emission is commonly detected on source, even if relatively weak. Off source, it is seen only in the highest density shocks, such as those associated with NGC 1333 IRAS4B. Some sources show gaseous molecular lines in absorption, including NH_3 in one case. Deep ice features are seen toward the protostars, revealing not just the major ice components but also ions (as part of salts) and complex organic molecules, with comparable abundances from low- to high-mass sources. The relative abundances of some gas and ice species are similar, which is consistent with ice sublimation in hot cores. We present a second detection of HDO ice in a solar-mass source, with an HDO/H_2O ice ratio of ~0.4%, thus providing a link with HDO/H_2O in disks and comets. A deep search for solid O_2 suggests that it is not a significant oxygen reservoir. Only a few embedded Class I disks show the same forest of water lines as Class II disks. This may be due to significant dust extinction of the upper layers in young disks caused by less settling of small dust as well as radial drift bringing in fresh dust.

Conclusions. This paper illustrates the wide range of science questions that a single MIRI-MRS IFU data set can address. Our data suggest many similarities between low- and high-mass sources. Large source samples across evolutionary stages and luminosities are needed to further develop these diagnostics of the physics and chemistry of protostellar systems.

Key words. methods: laboratory: solid state – stars: formation – ISM: atoms – ISM: jets and outflows – ISM: molecules

---

⋆ Corresponding author: `ewine@strw.leidenuniv.nl`

1. Introduction

The embedded phase of star formation, which is typically up to a few $\times 10^5$ yr after cloud collapse, is a critical and highly active period in the evolution of a protostellar system. It represents the moment when the source gathers most of its mass and is emerging from its dense environment (André et al. 2000; Evans et al. 2009; Dunham et al. 2014; Fischer et al. 2017). In addition to accretion onto the protostar itself, many other physical processes occur simultaneously in its immediate surroundings: infall from the natal cloud and collapsing envelope onto the young disk; jets and winds being ejected from the star-disk system; outflows sweeping up and shocking the material; and ultraviolet (UV) photons and X-rays heating, ionizing, and dissociating the gas (e.g., Arce et al. 2007; Bally 2016; Tobin & Sheehan 2024). Young disks are massive and still spreading radially (e.g., Hueso & Guillot 2005; Ohashi et al. 2023). Notably, planet formation has already started at this early stage (Manara et al. 2018; Tychoniec et al. 2020). Chemical processes range from freeze-out and ice chemistry in the cold outer parts to ice sublimation and high temperature chemistry in "hot cores" and shocks (e.g., van Dishoeck & Blake 1998; Jørgensen et al. 2020; Ceccarelli et al. 2023). Ultimately, the early pre- and protostellar stages provide the chemical building blocks of disks, comets, and planets (e.g., Caselli et al. 2012; Öberg & Bergin 2021).

However, because of tens to hundreds of magnitudes of visual extinction in the inner regions, these processes and materials can often only be probed at infrared and millimeter-centimeter wavelengths. The Atacama Large Millimeter/submillimeter Array (ALMA) has allowed protostellar systems to be imaged in the warm and cold(er) molecular gas and dust continuum at subarcsec scales, thus enabling their physical and chemical structure to be probed (e.g., Tobin & Sheehan 2024). However, many key processes, as traced by diagnostic lines of warm-to-hot (shocked) gas and of solid state material, can only be observed at mid- and far-infrared wavelengths.

Pre-JWST observations with the *Infrared Space Observatory* (ISO), the *Spitzer Space Telescope*, the *Herschel Space Observatory*, and ground-based facilities (e.g., VLT, Keck, IRTF) have made great progress in finding and characterizing protostars (e.g., Furlan et al. 2008; Evans et al. 2009; Dunham et al. 2014); in using atomic, H_2, and CO lines to probe shock physics (e.g., Rosenthal et al. 2000; Dionatos et al. 2009; Watson et al. 2016; Karska et al. 2018); in tracing H_2O from clouds to disks (e.g., van Dishoeck et al. 2021); and in making an inventory of interstellar ices (e.g., Boogert et al. 2015). However, all of these observations have so far been hampered by either poor spatial resolution, poor spectral resolution, and/or low sensitivity. Optical and near-infrared imaging and spectroscopic data from the ground and with HST have provided high spatial and spectral resolution information on jets and outflows but only in a limited number of tracers at positions with low extinction further away from the source (e.g., McCaughrean et al. 1994; Giannini et al. 2015). While radio observations can probe ionized jets and masers in the inner regions of deeply embedded sources (e.g., Anglada et al. 2018; Ray & Ferreira 2021; Moscadelli et al. 2022), they lack many other diagnostics. As a result, our understanding of the physical and chemical structure of this early deeply embedded protostellar phase is still incomplete.

The *James Webb Space Telescope* (JWST) (Rigby et al. 2023; Gardner et al. 2023), in particular its Mid-InfraRed Instrument (MIRI) (Rieke et al. 2015; Wright et al. 2023), allows for the next big leap in star formation and protostellar research by bridging the millimeter and near-infrared wavelength regime and providing unique information. The spatial resolution of MIRI of 0.19, 0.58, and 0.96″ at 5, 15, and 25 μm, respectively, corresponds to 29, 87, and 144 au at typical distances of low-mass protostars (~150 pc, $< 10^2$ $L_\odot$) and 570, 1740, and 2800 au at that of high-mass protostars (~ 3 kpc, $> 10^4$ $L_\odot$). These scales are well matched to the sizes of their envelopes and disks. The Medium Resolution Spectrometer (MRS) enables mapping of the inner parts of jets and outflows through its Integral Field Unit (IFU) (Wells et al. 2015; Argyriou et al. 2023). The MRS spectral resolving power of $R = \lambda/\Delta\lambda \sim 1500$–4000 is much higher than that of *Spitzer* (which had R=50–100 at <10 μm; R = 600 at >10 μm), thus boosting line-to-continuum ratios of gas-phase lines and allowing solid-state bands to be fully resolved. Combined with mJy sensitivity for IFU spectroscopy, this means that the inner parts of collapsing envelopes and the outflows of protostars can be dissected on subarcsec scales in the mid-infrared for the first time. Nearly all previous mid-infrared spectral line studies were based on single pointings with 5–40″ aperture sizes.

The near-infrared spectrograph NIRSpec on JWST (Böker et al. 2023) has similar capabilities as MIRI-MRS, but it covers the 1–5 μm range at R up to 2700. Its IFU spectrometer is also well suited for studying the inner regions of protostars at greatly enhanced sensitivity than was possible before (e.g., Federman et al. 2024). Several protostellar studies with JWST, including our program, therefore include both MIRI-MRS 5–28 μm and NIRSpec-IFU 3–5 μm data (see references below). This paper, however, focuses almost exclusively on the MIRI data.

In this paper, we outline the MIRI Guaranteed Time Observations (GTO) "JWST Observations of Young protoStars" (JOYS) program centered on MIRI-MRS 5–28 μm observations of protostellar sources from low (<1 $L_\odot$) to high luminosity (>10^4 $L_\odot$) and from the earliest deeply embedded stages where the envelope mass is much larger than the stellar mass – Class 0 for low-mass and infrared dark clouds (IRDCs) for high-mass protostars – to the transitional stage where the star and disk are fully assembled and only a tenuous envelope is left (Class I/II for low-mass protostars) (van Dishoeck et al. 2023; Beuther et al. 2023). Our program 1290 (PI: E.F. van Dishoeck) uses a single observational approach for a set of 23 (17 low-mass plus 6 high-mass) protostellar targets (the total is 32 if resolved low- and high-mass binary components are counted individually) in order to address the scientific topics listed in Sect. 2.3. For each source, single IFU images or small mosaics (up to 3 × 3) were taken covering the central protostar, its immediate envelope structure, and the inner region of the jets, winds, and outflows (Fig. 1). The field of view (FoV) of the IFU varies from the shortest to the longest wavelengths between 3.2″ × 3.7″ and 6.6″ × 7.7″, so the 3 × 3 mosaic covers a 10–20″ region depending on wavelength, thus corresponding to scales of ~1000 (low-mass) to ~10 000 (high-mass) au. One source, Herbig-Haro (HH) 211, is covered over the full extent of its blue outflow lobe and part of the red lobe, ~1′ in length, by the MRS in program 1257 (PI: T. Ray) (Ray et al. 2023; Caratti o Garatti et al. 2024). The resulting spectral images provide a spatially resolved census of the molecular, atomic, and ionized species covered in the 5–28 μm range (Fig. 2). Nearly all IFU pixels have a rich mid-infrared spectrum, making this program ideally suited for the IFU.

The 56-hr JOYS MIRI European Consortium GTO program (PIDs 1290 + 1257)[1] is being carried out in close collaboration with three other programs: the MIRI GTO program 1236 (PI: M. Ressler) covering ten protostellar Class 0 and I binaries in Perseus (12.7 hr), the GTO program 1186 (PI: T. Greene)

---

[1] `miri.strw.leidenuniv.nl`

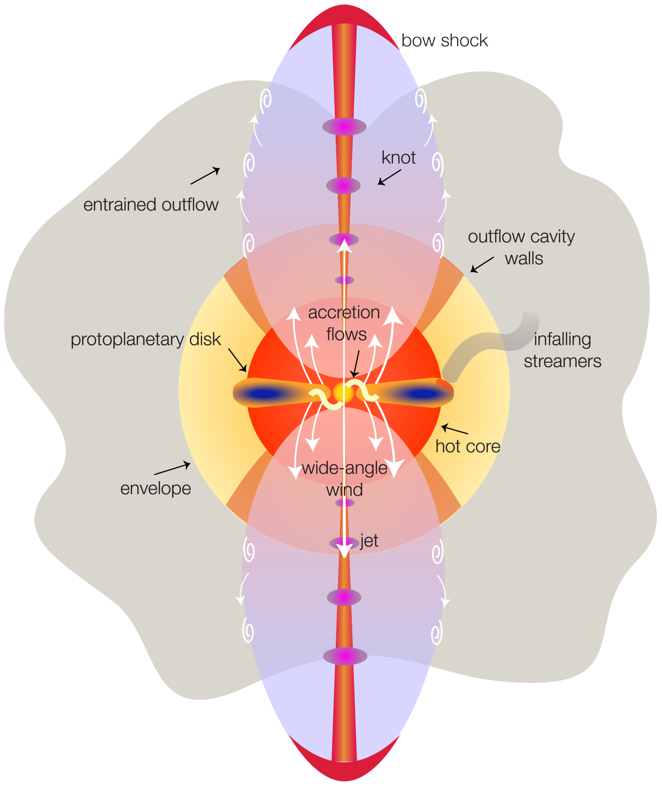

Fig. 1. Schematic of a protostellar source with the various physical components studied in this work indicated.

obtaining NIRSpec IFU 1–5 μm observations of two Class 0 protostars in Serpens (11.9 hr) that are part of JOYS, and the General Observer (GO) program 1960 (PI: E.F. van Dishoeck) targeting most of the low-mass protostars with NIRSpec IFU spectroscopy (21.5 hr). Together, these five programs are denoted as JOYS+. In this paper, we only focus on the program overview and representative results from MIRI observations taken within the JOYS program (PIDs 1290 + 1257), but we note opportunities for future studies with the full JOYS+ data set.

Several other JWST MIRI and NIRSpec GO programs focused on protostars have been carried out in JWST Cycle 1, most notably the Investigating Protostellar Accretion (IPA) program (PI: T. Megeath, PID 1802, 65.1 hr) (Federman et al. 2024; Rubinstein et al. 2024; Narang et al. 2024; Brunken et al. 2024a; Tyagi et al. 2025); the CORINOS program (PI: Y. Yang, PID 2151, 24.6 hr) (Yang et al. 2022; Salyk et al. 2024; Okoda et al. 2025); PROJECT-J (PI: B. Nisini, PID 1706, 23.1 hr) (Nisini et al. 2024); a deep MIRI+NIRSpec spectrum of L1527, a source that is also contained in JOYS (PI: J. Tobin, PID 1798, 7.6 hr); the IceAge Early Release Science (ERS; PI: M. McClure, PID 1309, 33.9 hr) (McClure et al. 2023; Rocha et al. 2025); and It'sCOMplicated GO programs (PI: M. McClure, PID 1854, 17.7 hr) (McClure et al. 2025). We fold the initial publications from these programs into the discussion of the JOYS program results. We also make a comparison of young disks studied within JOYS with the more mature Class II disks studied in the MIRI mid-INfrared Disk Survey (MINDS) GTO program (PI: Th. Henning, PID 1282) (Kamp et al. 2023; van Dishoeck et al. 2023; Henning et al. 2024). In addition, we make a link with the rich molecular spectroscopy now seen in extragalactic sources such as part of the Mid-Infrared Characterisation of Nearby Iconic galaxy Centers (MICONIC) MIRI GTO program (Buiten et al. 2025).

The outline of this paper is as follows. Sect. 2 summarizes the science cases and terminology used in this paper as well as the different diagnostic features at mid-infrared wavelengths. Sect. 3 presents the observational strategy and data reduction details. The subsequent sections present early and new results concerning the different science topics highlighted in Sect. 2 and Fig. 1. Sect. 4 focuses on protostellar accretion rates and variability, while Sect. 5 centers on images of jets, winds, and outflows as traced by different volatile, semi-refractory, and refractory species, and it presents a comparison of different derivations of mass-loss rates. Sect. 6 summarizes the gas-phase molecules seen in warm envelopes (hot cores), dense molecular shocks, and winds in the context of different chemical models. Sect. 7 highlights the detection of ices in the cold outer envelopes, including the detection of icy complex molecules and HDO as well as a deep search for O_2 ice. Sect. 8 focuses on the lack of clear signatures of emission from young embedded disks in most sources. The low-mass Class 0 sources Serpens SMM3 and B1-c and the high-mass source IRAS 18089-1732 are used as representative examples to illustrate the various results. Figure 2 provides example protostellar spectra with different gas and ice features identified in the two low-mass sources; the spectrum of the high-mass source IRAS 18089-1732 (hereafter IRAS 18089) is presented in Sect. 7. More detailed background information on each of these science cases is presented in Sect. 2.3 and Appendix B in order to avoid interrupting the flow of the results. Appendix C provides an example of science that can be done with the parallel imaging obtained in this program.

The overall aim of this paper is to highlight the rich and diverse science that a single MIRI-MRS data set can address. Future papers will go into more depth regarding each individual topic across the full JOYS(+) sample, as is done for the gas-phase molecular lines in van Gelder et al. (2024a).

2. Infrared spectroscopy of protostellar systems

2.1. Terminology

Figure 1 summarizes the different components of a protostellar system. In this paper, we use the term "jet" to refer to the high-velocity ($\gtrsim$50 km s^{-1}) and highly collimated (an opening angle of less than a few degrees) material that is directly ejected from the immediate vicinity of the protostellar embryo by MHD winds and recollimated into a jet. The term "outflow" is mainly used to describe the cold entrained outflow material that is imaged in low-J CO millimeter lines. However, the term "outflow" is sometimes also loosely adopted to refer to the entire jet+wind+(entrained-)outflow system, both in this paper and in the literature. The term "wind" refers to lower velocity ($\sim$10 km s^{-1}), wide-angle material that, similarly to the jet, is directly launched from the star-disk system. There is considerable discussion in the literature on the different types of winds: stellar winds versus disk winds, with the latter category containing both photoevaporative, X- and MHD disk winds depending on the launching mechanism. The jet and wind can be part of a single physical phenomenon that produces a velocity, temperature and ionization gradient that decreases away from the jet axis and is therefore revealed in different tracers. Some wind material can also be mixed in from the surrounding slower-moving outflow.

Internally in the jet, varying ejection velocities may lead to shocks that manifest themselves as "knots," also called "internal working surfaces." At the tip of the outflow when the jet impacts the interstellar medium at rest, they are usually called "bow shocks," although such curved structures can also be found

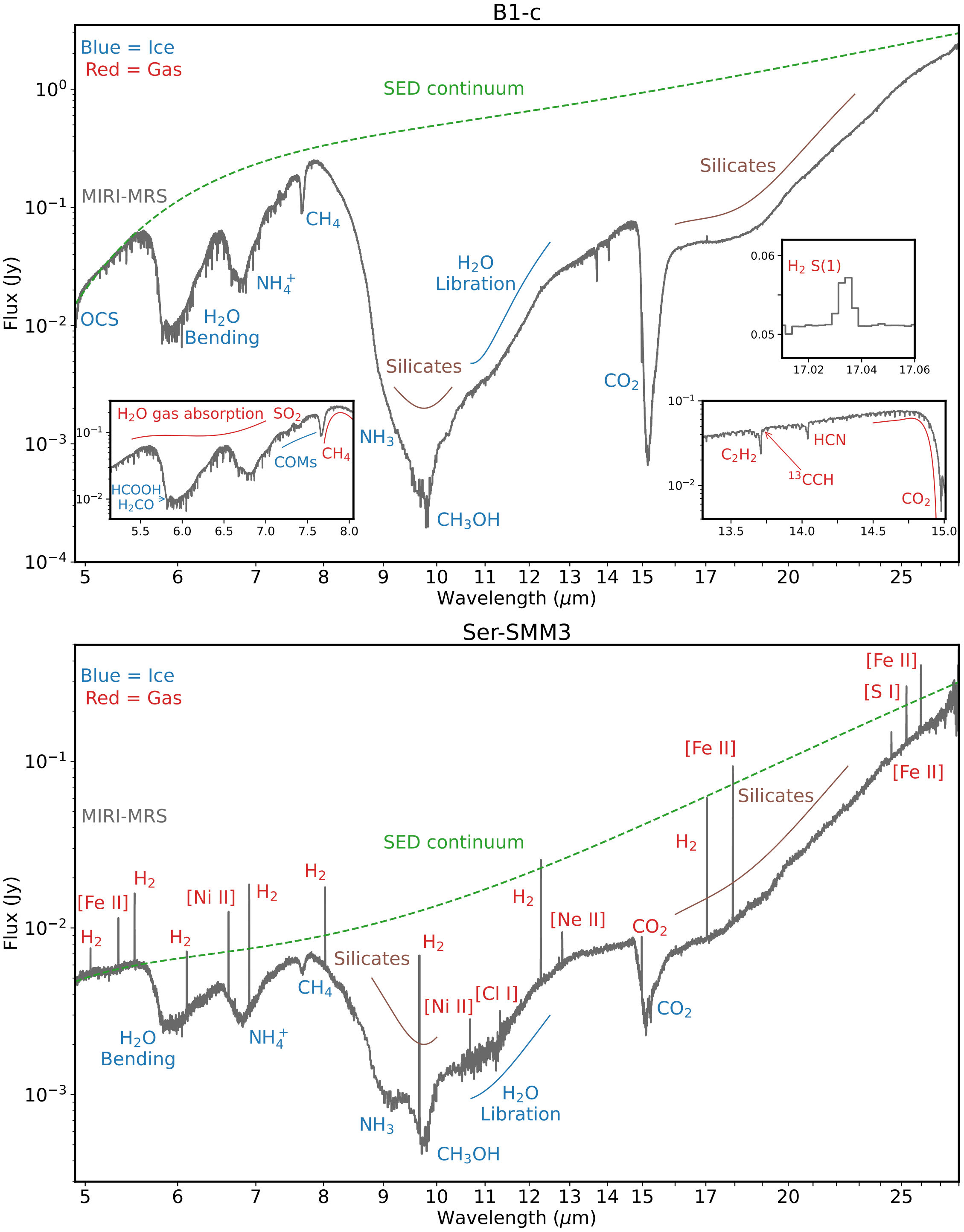

Fig. 2. Spectra obtained with JWST MIRI-MRS of the low-mass Class 0 protostars B1-c (top) and Serpens SMM3 (bottom) illustrating the different molecular gas (red) and ice (blue) features that can be observed and analyzed. Different components of the protostellar system are enhanced in the panels. The B1-c spectrum (top) highlights the gas-phase molecular lines in this source. Atomic emission lines are present but not very strong. In contrast, both H_2 and atomic emission lines are very prominent for Serpens SMM3 (bottom). At the bottom of the silicate feature at 10 µm, close to the noise limit, the spectra have been binned by a factor of four to enhance the S/N. (See Figs. B.3 and B.11 of van Gelder et al. (2024a) for individual MIRI-MRS sub-bands.)

along the jet. The term "shell" indicates a curved paraboloidal structure produced when a wind propagates into the surrounding medium, but we do not use it here because of the possible confusion with internal working surfaces and bow shocks.

The term "protostellar embryo" is used to indicate the young forming star itself, whereas the term "core" is reserved for the interstellar cloud core out of which the system forms. Strictly speaking, the term "protostar" refers to the protostellar embryo only, but is often used loosely in the literature (and in this paper) to refer to the entire "protostellar system" consisting of embryo + jet + wind + outflow + envelope system. For more evolved Class II (T Tauri) sources, the young star is indicated with the term "pre-main sequence star" (see papers and reviews by Ferreira et al. 2006; Arce et al. 2007; Frank et al. 2014; Bally 2016; Ray & Ferreira 2021; Pascucci et al. 2023; Bacciotti et al. 2025 for further descriptions of these terms).

The protostellar embryo is surrounded by a centrally concentrated collapsing envelope extending to thousands of au consisting of dense gas and dust that is heated by the protostellar luminosity and thus has a decreasing temperature and density with radius (Jørgensen et al. 2002; Tobin & Sheehan 2024). "Streamers" are velocity-coherent elongated narrow gas structures that may provide fresh material to the protostellar system (e.g., Valdivia-Mena et al. 2024). The inner warm part of the envelope where ices sublimate ($T \gtrsim 100$ K) is called the "hot core," sometimes also named "hot corino" for low-mass sources. It is distinguished from dense shock-heated or UV-heated gas. The term "disk" is reserved for disk-like elongated structures for which the gas has close to Keplerian rotation. Elongated structures seen in dust emission on larger scales are called "tori." If infalling material reaches the disk, for example through streamers, this may create a slow, dense "accretion shock."

2.2. Mid-infrared spectroscopy

The mid-infrared regime is very rich spectroscopically, containing a wealth of atomic, ionic and molecular gas lines, as well as Polycyclic Aromatic Hydrocarbon (PAH), ice and silicate bands that cannot be observed at any other wavelength (Fig. 2) (see review by van Dishoeck 2004). Early JWST summaries are by Yang et al. (2022); Nisini et al. (2024, their Table 1) and van Gelder et al. (2024a). The MIRI spatial and spectral resolution allows one to distinguish the physical processes producing them: spatially extended outflows and jets can readily be separated from compact hot cores and disks, and gas-phase lines can be distinguished from ices. Key diagnostics in the MIRI 5–28 μm range are described in the following paragraphs (see more detailed background information and references in individual subsections of Sect. 2.3 and Appendix B).

H_2: The mid-infrared pure rotational lines within v=0 and 1 are excited in warm gas up to 2000 K and down to ~100 K, probing and imaging its temperature structure and mass. In contrast, near-infrared ro-vibrational H_2 lines at 2 μm only probe the hottest gas and are often too extincted to be observed in these regions. Combined with NIRSpec observations at 2.5–5 μm, the H_2 excitation can also be used to distinguish shocks versus UV photon-dominated regions (PDRs).

Atomic lines: Several [Fe II], [Fe I], [S I], [Ne II], and [Ne III] lines are commonly seen and cover refractory, semi-refractory, and volatile elements. Together with H_2, they are important diagnostics of dissociative $J-$ versus non-dissociative $C-$ type shocks (including shock speed and density) and whether or not dust destruction has taken place. The [Ne III]/[Ne II] ratio is a diagnostic of ionization state and thus the ionizing source. Lines from lower abundance elements such as [Ar II], [Ar III], [Ni II], [Co II], and [Cl I] provide additional information on the physical structure and elemental depletion of refractory and more volatile elements.

H I recombination lines: These lines provide one of the few possibilities to measure the accretion rate of hot (5000–15 000 K) gas onto the growing protostellar embryo in deeply embedded sources (e.g., H I 7–6 (Humphries α), 6–5 and 8–6). They can also trace extended jet emission, especially the high-energy transitions such as 4–3 (Paschen β) and 7–4 (Brackett γ).

Symmetric molecules: Molecules without a permanent dipole moment such as CH_4, C_2H_2, $CH_3^{(+)}$, and CO_2 cannot be studied by traditional millimeter techniques but are uniquely accessible to infrared studies. These are also among the most abundant C- and O-containing species and are thus important to assess the C and O chemistry and budgets.

Other molecular lines: In addition to the symmetric molecules, gaseous CO, H_2O, HCN, SO_2, CS, NH_3, and SiO emission or absorption can be detected. Their lines arise from the inner regions of embedded disks, from the inner warm envelopes ("hot cores") or from non-dissociative shocks. In particular, H_2O, a molecule that is difficult to observe from the ground due to the Earth's atmosphere, can be probed with MIRI through both its ro-vibrational band at 6 μm as well as the high-lying pure rotational lines at 12–28 μm. The excitation of these molecules provides a good indicator of gas temperature, whereas their abundances probe high temperature gas-phase chemistry and ice sublimation. Radiative pumping by infrared continuum radiation from warm dust also plays a role in producing these lines.

OH: The OH molecule represents a special case since its mid-infrared lines at 9–11 μm originate from very high energy levels that are being populated following water photodissociation. This so-called prompt emission provides a measure of the UV field combined with the number of photodissociating water molecules. At longer mid-infrared wavelengths, OH emission is produced by chemical pumping through the O + H_2 reaction.

HD: Several HD lines are covered by MIRI, which together with H_2 allow the [D]/[H] ratio in dense protostellar environments to be determined and compared to the more diffuse ISM studied with ultraviolet absorption lines, thereby providing information on the amount of D locked up in grains. By targeting sources at different galactocentric radii, constraints on the [D]/[H] gradient across the Galaxy can be obtained.

Ices: All dominant ice components in the cold outer envelope are probed by JWST (MIRI + NIRSpec) at 2.3–20 μm. Narrow ice bands such as that of CH_4 can now be fully resolved, in contrast with *Spitzer*. MIRI also enables the identification of weak absorption bands in the critical 5–9 μm region due to complex organic molecules and ammonium salts. The ice profiles of molecules such as $^{(13)}CO_2$ provide information on the ice environment and temperature history, whereas the gas/ice ratio of species such as CH_4, H_2O and CO_2 can be used to test hot core scenarios of ice sublimation at their snowlines. With the sensitivity of JWST, ice mapping against the extended mid-infrared continuum is possible.

Solids: The vibrational bands of silicates, oxides and carbides occur uniquely at mid-infrared wavelengths. Their band profiles are sensitive to grain composition and whether or not they have been crystallized due to heating. The silicate optical depth provides an independent measure of extinction to the source. See Appendix G for a more in-depth summary of extinction determinations.

PAHs: The PAH features are commonly seen in PDRs associated with high-mass star-forming regions, where they measure the strength of the local UV field. In contrast, PAH bands are weak or absent from embedded protostellar sources, both low- and high mass, with only a very low level of PAH emission seen in the surrounding cloud. Likely explanations include freeze-out into ices and coagulation to larger PAH systems that do not emit, rather than a lack of UV radiation to excite them (Geers et al. 2009). PAHs are not further discussed in this paper except briefly in Appendix C.

Mid-infrared SED: The infrared part of the spectral energy distribution (SED) of a protostellar system is most sensitive to geometry and the presence of disks. JWST allows for detection of more deeply embedded sources that were too weak for *Spitzer*. The wavelength regions on both sides of the 10 μm silicate feature are particular transparent, allowing one to peer deep into the protostellar source. Scattering rather than thermal emission dominates at shorter wavelengths: its contribution as function of wavelength can now be constrained thanks to the combined spatial and spectral information of MIRI's and NIRSpec's IFUs.

The NIRSpec 1–5 μm data are not analyzed here but they add higher lying atomic (e.g., [Fe II]) and H I recombination lines as well as a forest of H_2 and CO ro-vibrational lines that together probe hotter gas than studied in the MIRI range (see Federman et al. 2024; Rubinstein et al. 2024, for IPA program). As noted above, several key ice features also occur in the NIRSpec range, most notably H_2O, CO and CO_2 (e.g., Brunken et al. 2024b; Tyagi et al. 2025).

2.3. Science drivers and background

This section describes the main science drivers and unique contributions that JWST MIRI can bring to studies of each of the protostellar components labeled in Figure 1. Detailed results from related JWST programs mentioned in Sect. 1 are cited throughout Sects. 4–8. The terminology used is that of Sect. 2.1, whereas more detailed background information and references can be found in Appendix B.

2.3.1. Protostellar accretion

The young protostar itself is still growing in the embedded phase but the rate at which accretion from disk to protostellar embryo occurs is uncertain and difficult to measure, yet it is a crucial missing parameter in many protostellar evolution studies. The optical lines such as Hα and Brγ, traditionally used to measure accretion rates for Class II sources (Hartmann et al. 2016; Manara et al. 2023), are often too extincted, although a few Class 0 sources have been detected at 2 μm (Le Gouellec et al. 2024), sometimes assisted by looking down outflow cavities. The mid-infrared H I recombination lines have been proposed as one of the few direct measurements of accretion rates of deeply embedded sources, in particular the H I 7–6 line at 12.37 μm (Rigliaco et al. 2015). These H I lines can now be surveyed by JWST with unprecedented sensitivity (Beuther et al. 2023; Tofflemire et al. 2025).

The accretion process is known to be episodic with rates varying by orders of magnitude over relatively short timescales (e.g., Fischer et al. 2023). This variability can manifest itself through "bullets" or "knots" in the jets that are caused by varying ejection velocities linked to discrete peaks in accretion activity. JWST provides opportunities to observe these knots and their movements much closer to the protostar than before (Ray et al. 2023; Federman et al. 2024).

2.3.2. Protostellar jets, winds, and outflows

Jets and outflows are detected in all embedded protostellar systems, from low- to high-mass protostars (e.g., Beuther et al. 2002; Ray et al. 2007; Frank et al. 2014; Bally 2016; Pascucci et al. 2023). Outflow- and accretion activity are linked, so outflows are expected to be most powerful in the earliest highly extincted stages, i.e., the Class 0 phase for low-mass protostars and the IRDCs for high-mass sources. JWST is unique in its ability to probe the physics of these earliest protostellar outflows at mid-infrared wavelengths, especially the highly collimated underlying jet driving the outflow, as illustrated by the many atomic, H_2 and other diagnostics highlighted in Sect. 2.2 and seen in Figure 2.

The ISO-SWS (e.g., Cernicharo et al. 2000), *Spitzer*-IRS (e.g., Maret et al. 2009; Dionatos et al. 2009; Watson et al. 2016) and *Herschel*-HIFI and PACS (e.g., Karska et al. 2018; van Dishoeck et al. 2021) data have illustrated the potential of mid- and far-infrared studies to probe the warm (few hundred K) and hot (1000–2000 K) gas associated with jets, winds, and outflows but were limited to spatial resolutions of 5–10″ or larger. Two temperature components have typically been found in the H_2 and CO excitation. For low-mass protostars, a transition from molecular to atomic to ionized jets appears as the sources evolve from the Class 0 to the Class II stage (Nisini et al. 2015). JWST MIRI improves the spatial resolution by factors of >10–100 and can now study the base of the wind on <100 au scales, most notably with H_2, showing whether it is collimated or not.

A related area of interest concerns identifying the physical processes that actually heat the gas as seen in H_2, as they have not been identified. At bow-shock and jet knot positions it is clear that mechanical heating through high-velocity shocks is responsible (e.g., Hollenbach & McKee 1989). However, winds launched from the disk close to the protostar can be heated by other mechanisms. For MHD winds, the ambipolar ion-neutral friction dominates (e.g., Panoglou et al. 2012), whereas for photoevaporative winds, (E)UV radiation and X-rays heat the gas (Pascucci et al. 2023). Ultraviolet heating can also be important for gas within or at outflow cavity walls at larger distance from the protostar (e.g., Spaans et al. 1995), whereas winds can impact those walls and create local shocks. Thus, the dominant heating mechanisms of warm and hot H_2 can change from position to position in outflows, and a combination of mechanisms can contribute at any position.

Both JWST MIRI and NIRSpec have the ability to image the stratification of the different velocity and temperature components of jets, winds, and outflows at different evolutionary stages and thereby probe the different physical processes (e.g., Caratti o Garatti et al. 2024; Federman et al. 2024; Tychoniec et al. 2024; Delabrosse et al. 2024; Pascucci et al. 2025). MIRI can also address the question whether dust is launched in jets and winds in the youngest protostars, and whether those dust grains are subsequently destroyed by shocks, enriching the gas in refractory elements (Podio et al. 2006; Anderson et al. 2013; Giannini et al. 2015; Delabrosse et al. 2024). This, in turn, provides information on the launching mechanisms and disk radius where the jet or wind is launched.

2.3.3. Hot cores and dense molecular shocks: Chemistry

In the inner regions of dense protostellar envelopes, ices sublimate into the gas at temperatures dictated by their binding energies. Above ~100 K, the temperature of the H_2O snowline, most molecules are in the gas where they may be processed further by high temperature gas-phase reactions. In contrast with ALMA, JWST can probe molecules like CO_2, C_2H_2 and CH_4 that have no permanent dipole moment but that are key molecules in gas-ice chemistry. Together with other simple molecules (see Sect. 2.2), they can test hot core chemistry models consisting of ice sublimation and high temperature gas-phase chemistry (e.g., Doty et al. 2002), including irradiation by UV and X-rays (Bruderer et al. 2009; Notsu et al. 2021). Early pioneering high spectral resolution ground-based data (e.g., Lacy et al. 1989; Evans et al. 1991; Barr et al. 2020) and space-based observations (e.g., Lahuis & van Dishoeck 2000; Sonnentrucker et al. 2007; Indriolo et al. 2015) were limited mostly to high-mass protostars. JWST MIRI-MRS now opens the possibility to study gas-phase lines in nearby low-mass sources with high enough spectral resolution to detect weak emission lines on top of a strong continuum, and with high enough spatial resolution to locate the emission either with the hot core or with the more extended outflow. The detection of isotopologs such as $^{13}CO_2$ and $^{13}CCH_2$ allow for more accurate determinations of the optical depth of the lines and thus column densities (see van Gelder et al. (2024a) for protostars and Grant et al. (2023); Tabone et al. (2023); Colmenares et al. (2024) for disks). A particularly interesting question is the chemistry of C_2H_2 in hot gas and its sensitivity to both temperature, carbon abundance and X-rays (Walsh et al. 2015), also in connection with high abundances of C_2H_2 and other hydrocarbon molecules found with JWST in warm gas in Class II protoplanetary disks, especially those around very low-mass stars (Tabone et al. 2023).

At positions offset from the protostellar source, bright emission from simple molecules can also be found, especially at bow-shock positions (e.g., Tappe et al. 2012) and at dense jet-knot positions (e.g., Neufeld et al. 2024). Indeed, JWST has demonstrated that the so-called green fuzzies detected with *Spitzer*-IRAC Band 2 at 4.6 μm in both low- and high-mass protostars (e.g., Noriega-Crespo et al. 2004; Cyganowski et al. 2008) may well be dominated by CO ro-vibrational emission rather than H_2 (Ray et al. 2023). Thus, JWST can now test models of molecular infrared emission from dense molecular shocks (e.g., Hollenbach & McKee 1989; Kaufman & Neufeld 1996) and investigate differences between high temperature hot core and shock chemistry. JWST also opens up the possibility to investigate the chemistry of wide-angle winds close to the protostar.

2.3.4. Cold outer envelopes: Ices

The bulk of protostellar envelopes is cold enough that most molecules are frozen out as ices onto the dust grains. These ices are therefore a major reservoir of the heavy elements (see review by Boogert et al. 2015). ISO-SWS, *Spitzer* and ground-based telescopes have provided ice inventories toward the brightest, usually more evolved, protostellar sources, both low- and high-mass. JWST MIRI and NIRSpec can now survey the coldest and ice-richest protostars (e.g., Brunken et al. 2024a) as well as dense pre-stellar clouds (McClure et al. 2023).

The higher spectral resolution of JWST allows ice band profiles to be fully resolved, especially of molecules like CH_4 in the critical 5–10 μm range where *Spitzer*-IRS lacked resolution; these bands in turn provide diagnostic information on ice environment and heating (e.g., Pontoppidan et al. 2008; Öberg et al. 2011). JWST's sensitivity results in high S/N spectra on weak sources in which not only simple but also more complex organic molecules can be identified (Rocha et al. 2024), as hinted at in earlier data (e.g., Schutte et al. 1999). This in turn allows for tests of their formation, especially whether complex molecules are formed in ices or whether they are mostly the product of high-temperature gas-phase chemistry. Other species in ices that are well suited for renewed studies with JWST include ammonium salts, O_2 and HDO (Slavicinska et al. 2024; Slavicinska et al. 2025a). The HDO/H_2O ice ratio is particularly interesting as a tracer of the inheritance of water from clouds to comets (Altwegg et al. 2019; Aikawa et al. 2024), but has so far been tested only indirectly with gas-phase water in hot cores that is thought to represent sublimated ices (Persson et al. 2014; Jensen et al. 2019).

2.3.5. Embedded disks

The physical and chemical properties of disks in the protostellar phase are still poorly constrained (Tobin & Sheehan 2024). Due to their higher accretion rates, embedded disks are warmer and therefore have more molecules in the gas (van't Hoff et al. 2020). Also, infall of envelope material onto the disk through streamers may still take place causing weak shocks (e.g., Pineda et al. 2023; Podio et al. 2024). JWST MIRI can search for signatures of these accretion shocks, especially through sulfur-bearing species such as SO_2 and [S I] lines.

ALMA is making great strides in studying embedded disks (e.g., Harsono et al. 2018; Ohashi et al. 2023) but cannot probe the inner few au of disks. Mid-infrared observations are particularly well suited for studying the gas in the planet-forming zones of disks, as is being amply demonstrated by the rich and diverse spectra obtained in early JWST observations of Class II disks (e.g., Gasman et al. 2023; Banzatti et al. 2023; Xie et al. 2023; Arabhavi et al. 2024; Temmink et al. 2024a). Pioneering ground-based CO 4.7 μm high spectral resolution data have revealed Keplerian rotation from the inner parts of Class II disks (e.g., Najita et al. 2003; Brown et al. 2013; Banzatti et al. 2022) as well as from several Class I protostars (Herczeg et al. 2011) and from embedded high-mass sources (e.g., Ilee et al. 2014, at 2.3 μm). These data demonstrate that gas in the upper layers of disks in the inner few au can be detected. A main question that MIRI-MRS can address is whether these young disks show a similarly rich chemistry as their more mature counterparts. MIRI and NIRSpec can also detect other interesting lines such as H_2 and [Ne II] to study the role of winds in the mass loss from young disks (e.g., Tychoniec et al. 2024; Delabrosse et al. 2024).

3. Observations and methods

3.1. Source sample

Table 1 summarizes the main properties of the sources observed with MIRI-MRS in the JOYS program. All low- and high-mass sources have been well studied and characterized in great detail prior to JWST, including with *Spitzer*, *Herschel* and submillimeter (ALMA, NOEMA) ground-based data. For example, many of them were part of the *Herschel* WISH program studying water from pre-stellar cores to disks (van Dishoeck et al. 2021). They were chosen for their ability to address the different science cases outlined in Sects. 2 and 4–8.

The low-mass sample consists of nearby sources at distances <500 pc that cover both the deeply embedded Class 0 and more evolved Class I phases with bolometric luminosities ranging from 0.2 to >100 $L_\odot$ and bolometric temperatures from <30 K to 200 K (van Gelder et al. 2024a). They were furthermore selected to belong to only three star-forming regions – Perseus, Taurus and Serpens – to minimize slew overheads, with two pointings in the isolated BHR 71 cloud added. Some sources were chosen because they have prominent outflows and jets (e.g., L1448-mm, Ser-SMM1, BHR71). To further study outflow physics, two dedicated pointings at "knot" positions in the blue-shifted outflow lobes well offset from NGC 1333 IRAS4A and Ser-emb8(N) were added. The protostar position of NGC 1333 IRAS4A is

Table 1. JOYS source sample and physical properties.

Source	RA^a [J2000]	Dec^a [J2000]	d (pc)	$L_{\rm bol}$ ($L_\odot$)	$T_{\rm bol}$ (K)	Class	$M_{\rm env}$ ($M_\odot$)	Binary ″	Other names	Ref.
IRAS4B	03:29:12.02	+31:13:08.0	293	6.8	28	0	4.7	10.7	Per-emb 13	1–5
IRAS4A1^b	03:29:10.54	+31:13:30.9	293	14.1	34	0	8.7	1.8	Per-emb 12	1–5
IRAS4A2^b	03:29:10.43	+31:13:32.1	293	14.1	34	0	8.7	1.8	Per-emb 12	1–5
B1-c	03:33:17.88	+31:09:31.8	293	5.0	48	0	5.3	–	Per-emb 29	1–5
B1-b	03:33:20.34	+31:07:21.4	293	0.23	157	I	2.1	14	Per-emb 41	1, 2, 5
B1-a-1	03:33:16.67	+31:07:54.9	293	2.3	113	I	1.5	0.4	Per-emb 40	1–3, 5
B1-a-2	03:33:16.68	+31:07:55.3	293	2.3	113	I	1.5	0.4	Per-emb 40	1–3, 5
L1448-mm	03:25:38.88	+30:44:05.3	293	8.5	49	0	3.9	8.1	Per-emb 26	1–5
Per-emb 8	03:44:43.98	+32:01:35.2	321	4.5	45	0	1.0	9.6	–	1–5
TMC1-W	04:41:12.69	+25:46:34.7	142	0.7	161	I	0.2	0.6	IRAS 04381+2540	3 ,4, 6, 7
TMC1-E	04:41:12.73	+25:46:34.8	142	0.7	161	I	0.2	0.6	IRAS 04381+2540	3, 4, 6, 7
TMC1A	04:39:35.20	+25:41:44.2	142	2.7	189	I	0.2	–	IRAS 04365+2535	3, 4, 6,7
L1527 IRS	04:39:53.88	+26:03:09.5	142	3.1	79	I	0.9	–	IRAS 04368+2557	3, 4, 6, 7
BHR71 IRS1	12:01:36.50	–65:08:49.4	200	14.7	68	0	19	15.7	IRAS 11590–6452	8–11
BHR71 IRS2	12:01:34.01	–65:08:48.0	200	1.7	38	0	19	15.7	–	8–11
Ser-SMM1-a	18:29:49.81	+1:15:20.4	436	109	39	0	58	2.0	Ser-emb 6	2, 3, 4, 12, 13
Ser-SMM1-b1	18:29:49.68	+1:15:21.1	436	109	39	0	58	0.3	-	2, 3, 4, 12, 13
Ser-SMM1-b2	18:29:49.66	+1:15:21.2	436	109	39	0	58	0.3	–	2,3,4,12,13
Ser-SMM3	18:29:59.31	+1:14:00.3	436	27.5	37	0	11.5	–	–	2, 3, 4, 14
Ser-S68N-N	18:29:48.13	+1:16:44.6	436	>6.0	58	0	10.4	1.4	–	2, 5, 15, 16
Ser-S68N-S	18:29:48.09	+1:16:43.3	436	>6.0	58	0	10.4	1.4	Ser-emb 8	2, 5, 15, 16
Ser-emb-8(N)^b	18:29:48.73	+1:16:55.6	436	1.8	–	0	–	6.6	SerpM-S68Nb	2, 15, 17, 18, 19
HH 211	03:43:56.81	+32:00:50.2	321	4.1	27	0	2.4	–	Per-emb 1	1, 2, 25
G28IRS2	18:42:51.99	–3:59:54.0	4510	10120	– –	IRDC/ HMPO	3288	–	G28P2	22, 23
G28P1	18:42:50.59	–4:03:16.3	4510	682	–	IRDC	4276	–	–	22, 23
G28S	18:42:46.45	–4:04:15.2	4510	364	–	IRDC	2296	–	–	22, 23
IRAS 23385	23:40:54.49	+61:10:27.4	4900	3170	–	HMPO	220	–	Mol160	20, 21
IRAS 18089	18:11:51.24	–17:31:30.4	2340	15 723*	–	HMC	1100*	–	G12.89+0.49	23, 24
G31	18:47:34.33	–1:12:45.5	5160	69 984	–	HMC	7889	–	–	22, 23

Notes. 1- Tobin et al. (2016), 2- Ortiz-León et al. (2018) , 3- Karska et al. (2018), 4- Kristensen et al. (2012), 5- Enoch et al. (2009), 6- Krolikowski et al. (2021), 7- van't Hoff et al. (2020), 8- Yang et al. (2020), 9- Seidensticker & Schmidt-Kaler (1989), 10- Tobin et al. (2019), 11- Yang et al. (2017), 12- Hull et al. (2017), 13- ALMA 2015.1.00354.S, 14- 2017.1.01350.S, 15- Le Gouellec et al. (2019), 16 - 2015.1.00768.S, 17- Tychoniec et al. (2021), 18- Podio et al. (2021), 19- 2019.1.00931.S, 20- Beuther et al. (2023), 21- Molinari et al. (2008), 22- Wang et al. (2008), 23- Urquhart et al. (2018), 24- Xu et al. (2011), 25- Sadavoy et al. (2014). *Distance corrected. Properties scalable with distance are corrected according to updated distance measurement. ^{a} Coordinates of millimeter interferometry source position; MIRI IFU pointing is usually offset from source toward blue outflow lobe, see Table A.1 for IFU pointings. ^{b} Source continuum center not covered in MIRI 1290 observations.

covered in PID 1236 as part of JOYS+; hence this source is not further included in the analysis here. Moreover, the entire blue outflow lobe and a small portion of the red lobe of HH 211 were imaged with MIRI-MRS in program 1257. These three Class 0 sources (HH 211, NGC 1333 IRAS4A and Ser-emb8(N)) are so deeply embedded that they are not detected even with JWST. Other sources were selected because of their very deep ice features facilitating the search for new minor ice species (e.g., B1-c). SVS4-5 is a special case because it is a "background" Class I/II source behind or inside the envelope of the Class 0 source Ser-SMM4 probing ices at very high densities (Pontoppidan et al. 2004; Perotti et al. 2020) and is not included in Table 1. A number of sources with confirmed young disks based on Keplerian rotation were included as well (e.g., L1527, TMC1, TMC1A).

Several sources are close binaries that can be resolved by MIRI at its shortest wavelengths, allowing for comparison of their outflow and ice properties on scales of <1000 au. In total 17 low-mass sources (23 sources counting binaries individually) were targeted. Of these 17 (23) sources, four (six) are Class I and one source is borderline Class 0/I (L1527). We note that program 1236 (PI: M. Ressler) is focused on binary sources in Perseus so the comparison of binary properties will be part of future JOYS+ publications.

For the high-mass sources, three Infrared Dark Clouds and three High-Mass Protostellar Objects (HMPOs) and hot molecular cores (HMCs) were chosen. Their properties and distances are included in Table 1. The MIRI-MRS data reveal several of these sources to be binaries or multiples: there are at least nine mid-IR sources detected in the six high-mass MRS target fields: IRAS 23385+6053 (hereafter IRAS 23385) displays a binary (Beuther et al. 2023), G28 P1 two distant sources, IRAS 18089-1732 (hereafter IRAS 18089) at least three sources, and G28S shows no sources at 5 µm. G28 IRS2 and G31 show one source each. As for the low-mass sources, the high-mass set has been selected to cover a broad range of masses and evolutionary stages

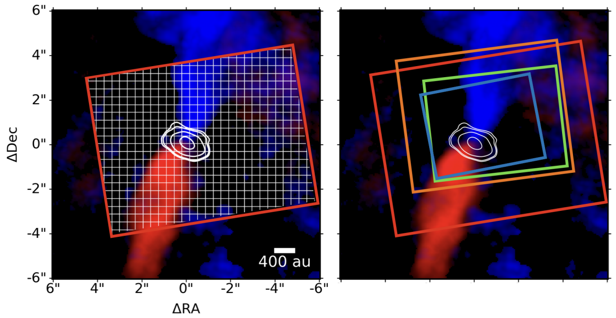

Fig. 3. Right: MIRI-MRS IFU footprint for channels 1 (blue), 2 (green), 3 (orange), and 4 (red) overlaid on the ALMA Serpens SMM3 CO 2–1 outflow map using data from Tychoniec et al. (2021). Two dithers were used. The positions of the IFU have been chosen on purpose to be slightly offset toward the blue outflow lobe for the shortest wavelength channels, but still covering some part of the red outflow lobe. The white contours indicate the 1.3 millimeter continuum showing the dust disk. Left: Illustration of the grid of individual spaxels for channel 4.

without saturating the MIRI-MRS. We note that many nearby well-known high-mass protostars studied with the ISO-SWS are too bright for JWST.

3.2. MIRI-IFU observations

The coordinates in Table 1 represent those of the protostellar source positions as found from millimeter interferometry. For the low-mass protostars, the actual MIRI-MRS IFU pointing positions are on purpose slightly offset from the millimeter continuum source position to cover a larger fraction of the less-extincted blue-shifted part of the outflow in the IFU, in addition to still catching some part of the red-shifted outflow. For TMC1A, the IFU has a larger offset from the source position to capture a larger fraction of its blue wind as imaged by ALMA (Bjerkeli et al. 2016). All MRS IFU pointing coordinates are summarized in Table A.1. The mid-infrared peak positions of the low-mass sources derived from the MRS data are listed in Table B.1 of van Gelder et al. (2024a). A single NIRSpec IFU spectrum of the source B1-c with the G395M mode is taken as well within program 1290 to obtain a full inventory of this ice-rich source including HDO ice.

The sources within one cloud were observed in a single uninterrupted sequence with one background (dark) position observed in each cloud to characterize detector artifacts and subtract the telescope background. For Perseus, this background was taken to be the position of the millimeter source B1-bS which is so deeply embedded that it is undetected with JWST. For Taurus, the background was taken with a single dither position, whereas for the other three cases a 2-point dither was used.

All sources have been observed with the full MIRI-MRS spectral coverage using the three grating settings (A, B, C) to observe the 5–28 µm range spread over four channels (1–4) of the MIRI IFU (Wells et al. 2015; Wright et al. 2023). A 2-point dither pattern for extended sources was adopted for most sources, except for B1-c and Ser-SMM1A for which a 4-point dither pattern was used. The typical integration time is 200 s per grating setting, except for L1527 which used 1000 s per grating and B1-c which had 2000 s in gratings A and C and 4000 s in grating B. This latter setting was chosen because grating B covers the deep silicate absorption around 10 µm where the source flux is much lower. The IFU FoV varies between 3.2″ × 3.7″ (channel 1) and 6.6″ × 7.7″ (channel 4). Figure 3 illustrates the IFU footprint of the different channels for Serpens SMM3, covering the central object, its immediate envelope structure and the inner region of the blue outflow and jet.

For some sources, we made small mosaics of the blue outflow lobe ranging from 1×2 to 3 × 3, thus mapping regions up to 12–20″ in size. These observational details are provided in Table A.1 in Appendix A; we note that they are sometimes listed as separate pointings in the archive. The total extent of the HH 211 blue lobe and a small portion of its red-shifted one (0.95′ × 0.22′) has been observed with 12 × 2 spatial settings (Caratti o Garatti et al. 2024). More details of the observations and mid-infrared continuum images of all low-mass sources in each of the four IFU channels are presented in Figures B.1–B.18 of van Gelder et al. (2024a) and in Caratti o Garatti et al. (2024) for HH 211.

Most of the JOYS sources were observed in Fall 2023. Only the high-mass source IRAS 23385+6053 (3000 $L_\odot$, 9 $M_\odot$) was observed early in the JWST mission, in August 2022. Hence, most of the early JOYS analysis has focused on this source (Beuther et al. 2023; Gieser et al. 2023b; Francis et al. 2024). Located at a distance of 4.9 kpc in the direction of the outer Galaxy, this puts the source at a galactocentric radius of 11 kpc, making IRAS 23385 a unique laboratory for studying star formation in the outer Galaxy. This paper provides one of the first opportunities to look at similarities and differences among the larger JOYS sample from low to high mass.

3.3. MIRI-MRS data reduction

The MIRI-MRS data were reduced and calibrated using the JWST calibration pipeline version 1.13.4 (Bushouse et al. 2024) using reference context `jwst_1188.pmap`. The steps adopted are the same as those in van Gelder et al. (2024a) of which only a short summary is provided here. The raw data were processed through all three steps of the JWST calibration pipeline. This included the subtraction of the dedicated background on the detector level, where astronomical emission in the background was masked so that it was not subtracted in the science data. Furthermore, the fringe flat for extended sources (Crouzet et al. 2025) and the 2D residual fringe correction (Kavanagh et al. in prep.) were also applied on the detector level. Prior to building the cubes, an additional bad pixel map was created using the Vortex Imaging Package (VIP) version 4.1 (Christiaens et al. 2023). Last, the final data cubes were constructed for each channel and sub-band separately with the outlier rejection and master background steps switched off. Spectra were extracted manually from selected positions in the datacubes using either an aperture with a constant diameter as function of wavelength (“circle”) or an aperture with its diameter increasing with wavelength (“cone”) following the size of the point spread function (PSF; Law et al. 2023).

Table C.1 of van Gelder et al. (2024a) provides 1σ noise level estimates in each of the MRS sub-bands for the JOYS low-mass targets at the continuum source position(s). They typically range from 0.1 mJy in channels 1–3 to several mJy in channel 4, with some sources (e.g., B1-a-NS and TMC1A) having higher noise levels due to their strong continuum or being located at the edge of the FoV. Noise levels are similar for the high-mass sources because of their similar integration times.

3.4. Simultaneous imaging

During the MIRI-MRS observations, the imager was turned on to simultaneously observe a field of 74″ × 113″ offset by ∼1′

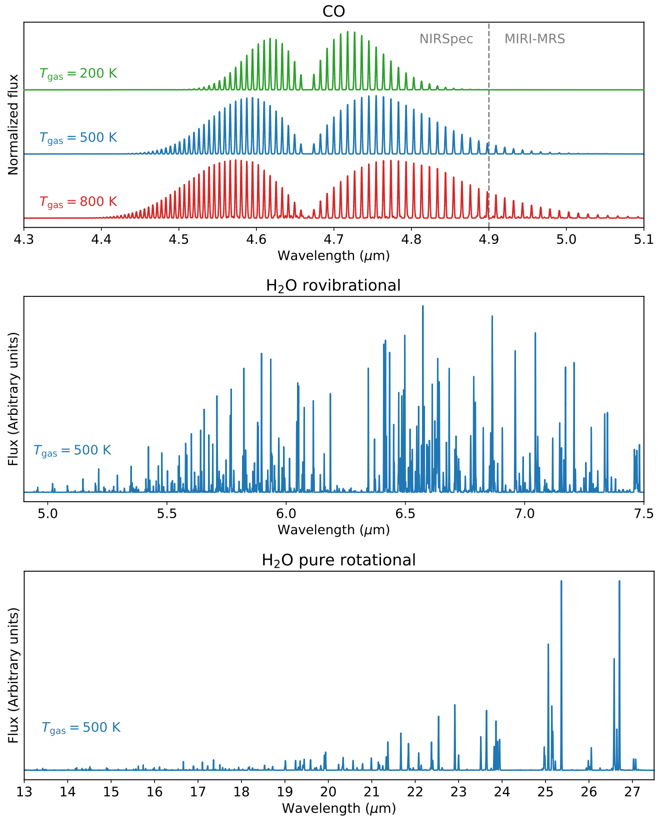

Fig. 4. Examples of normalized mid-infrared slab model molecular emission spectra in the optically thin regime. From top to bottom, CO at 500 K compared with 200 and 800 K, H_2O ro-vibrational lines at 5–7 μm, and H_2O pure rotational lines at 13–28 μm, both at 500 K.

from the MRS position at a position angle determined by the time of observations. This simultaneous imaging provides not only serendipitous science such as finding new deeply embedded protostars in the cloud, but it also serves as the absolute astrometric calibration of the MRS data by comparing with the positions of field stars that are in the Gaia catalog. Indeed, for the initial JOYS source IRAS 23385+6053, for which the source position was well known, an adjustment of 1.61″ in RA and 0.35″ in Dec in the telescope coordinates was needed based on comparison with the Gaia stars.

The imager has a plate scale of 0.11″ (Bouchet et al. 2015) and provides diffraction-limited imaging in a number of broadband filters. For the JOYS program, simultaneous imaging was obtained in the F1500W broadband filter centered at 15.0 μm (FWHM 2.92 μm) (Beuther et al. 2023). At that wavelength, the MIRI PSF is 0.49″ FWHM, providing nearly an order of magnitude sharper images than was possible with previous space instruments. The 15 μm filter was chosen to be away from PAH features, and to be intermediate between the *Spitzer* IRAS 8 μm and MIPS 24 μm bands to fill in that part of the SED. Being at a wavelength where the telescope background does not yet contribute, it also provides a good compromise between high angular resolution and good sensitivity at the longer MIRI wavelengths that can probe most deeply into the clouds. We note, however, that this filter is centered at the CO_2 ice band, which can absorb a significant fraction of the protostellar continuum along the line of sight through the envelope.

The MIRI images were processed through all three steps of the JWST calibration pipeline using reference context `jwst_1235.pmap` adopting the default parameters in each step. In the final step, the `tweakreg` step was switched off since very few Gaia stars are available in the FoV. The background level was estimated and subtracted by setting the `skymethod` option to local in the `skymatch` step. An example of the science that can be done with these simultaneous images to find new protostars in the outer Galaxy is provided in Appendix C.

3.5. Analysis of gas-phase spectra

The analysis of atomic lines and ices seen in the MIRI spectra is described in the various scientific sections. Here we summarize the analysis of gas-phase molecular lines to infer column densities and temperatures, following Francis et al. (2024); van Gelder et al. (2024a); Salyk et al. (2024) and papers studying molecular emission lines from disks (e.g., Salyk et al. 2011; Banzatti et al. 2025; Temmink et al. 2024a, and refs cited).

In the simplest case of spectrally resolved pure absorption and assuming an isothermal slab model, the measured optical depths are directly related to column densities. For unresolved lines such as with JWST, an intrinsic line width needs to be assumed and a curve-of-growth type of analysis to be performed (Boonman et al. 2003a; Barr et al. 2020); typical values are a FWHM of a few km s^{-1} up to 10–20 km s^{-1} (van Gelder et al. 2024a; McClure et al. 2025). It is usually assumed that the covering fraction of the absorbers against the continuum is unity and that the gas is at a single temperature, but this does not need to be the case (Knez et al. 2009; Li et al. 2024). Proper radiative transfer may therefore be needed (González-Alfonso et al. 2002; Lacy 2013).

Mid-infrared emission lines are also usually interpreted with isothermal slab models fitted to continuum-subtracted spectra. The emission is assumed to originate in a plane-parallel cylindrical slab of radius R and column density N. The radius R should not be viewed as a disk or envelope radius but rather represents the emitting area πR^2 having any shape at any location in the beam. The gas is taken to be at a single excitation temperature T_{ex}, and Figure 4 shows typical ro-vibrational spectra of CO and H_2O at 200–800 K. We note that MIRI only probes the tail of the CO v=1–0 P branch at high temperatures, and that the 5–28 μm range covers both the H_2O ro-vibrational bending mode lines as well as a forest of pure rotational water lines. Figure 5 illustrates how the CO_2 spectrum changes with temperature and optical depth (see also Cami et al. 2000; Bosman et al. 2017). Emission lines can be strongly affected by extinction from ices and dust (see Sect. 6 and Appendix G for details).

If collisions dominate the excitation, T_{ex} will approach the kinetic gas temperature T_{kin}, but the critical densities for this assumption to be valid are high, typically greater than 10^{12} cm^{-3} for vibrational lines (e.g., Bruderer et al. 2015). Such high densities may only be achieved in the inner few au of disks (Salyk et al. 2009; Carr & Najita 2011). Non-LTE effects will be important for regions with lower densities such as in shocks or in hot cores, where densities are typically 10^6 to 10^8 cm^{-3} on scales of 50 au (Kristensen et al. 2012; Notsu et al. 2021). However, in this case strong infrared radiative pumping through ro-vibrational transitions, by a radiation field whose intensity at the pumping wavelengths can be characterized by a temperature T_{rad}, can boost the vibrational emission (see e.g., Bruderer et al. 2015; van Gelder et al. 2024b, for the cases of HCN and SO_2).

In contrast, the rotational distribution within the $v = 0$ vibrational ground state can be thermalized by collisions at lower densities, and this rotational distribution, characterized by T_{rot}, is largely conserved in the vibrationally excited states through

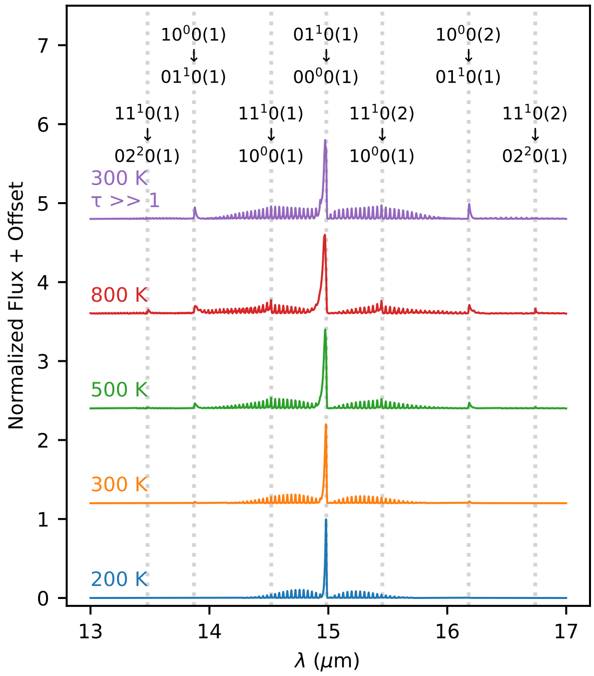

Fig. 5. Simulated normalized CO_2 mid-infrared spectra at different temperatures for optically thin emission (blue to red). Notable are the broadening of the Q branch and the appearance of hot bands (i.e., transitions between vibrationally excited states) with increasing temperature. These hot bands also become visible at lower temperatures when the CO_2 Q−branch emission becomes optically thick (purple).

infrared pumping and can thus reflect the kinetic temperature $T_{\rm kin}$. For molecules with a dipole moment, the density to achieve $T_{\rm rot}$ close to $T_{\rm kin}$ is around 10^8–10^9 cm^{-3}, whereas the rotational level populations of molecules without a dipole moment such as CO_2 are thermalized at much lower densities. In other words, $T_{\rm vib}$ is usually larger than $T_{\rm rot}$, with the former being controlled by radiative pumping at $T_{\rm rad}$ and the latter being closer to the gas temperature $T_{\rm kin}$.

4. Onset of star formation: Protostars and accretion

4.1. Probing the fossil accretion record from imaging

JWST's ability to probe the deeply embedded Class 0 stage is illustrated by the HH 211 outflow (d=321 pc, Ortiz-León et al. 2018). Despite the extent and power of this outflow, as highlighted by prominent shocked atomic, H_2 and CO emission at infrared and millimeter wavelengths (e.g., McCaughrean et al. 1994; Gueth & Guilloteau 1999; Lee et al. 2009; Dionatos et al. 2018), the current stellar mass as determined from kinematic studies is still comparable to that of a brown dwarf, only 0.08 M$_\odot$ (Lee 2015).

JWST-NIRCam infrared imaging of HH 211, taken as part of JOYS, has revealed its jet and outflow structure with unprecedented detail in both molecular (H_2, CO) and atomic ([Fe II]) lines (Ray et al. 2023). Because of its youth, the outflow is still compact and can readily be imaged in its entirety with JWST. The NIRCam images reveal an abundance of H_2 knots in the innermost highly extincted collimated jet which were previously undetected and/or unresolved (see Figure 6). The central source of HH 211, i.e., the protostar itself, remains undetected even with JWST's sensitivity, hidden behind A_V > 100 mag of extinction.

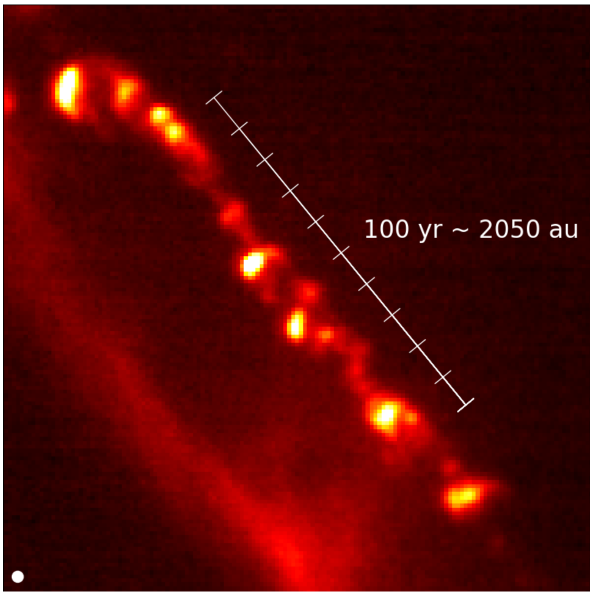

Fig. 6. Blow-up of the H_2 knots in part of the HH 211 jet in the blue outflow lobe imaged with the NIRCam F212N filter (Ray et al. 2023). This figure illustrates the typical separation between knots and thus implicitly the timescales between accretion bursts. The ruler shows the distance of jet gas covered in 100 yr when traveling at 100 km s^{-1}, in 10 sections of 10 yr each.

These H_2 knots provide a fossil record of the recent accretion history of the protostar. Comparison with archival VLT-ISAAC K-band images taken 20 years earlier demonstrates JWST's capabilities to measure the proper motions and thus the 3D kinematics of the outflow of this very young protostar (Ray et al. 2023). The tangential flow velocity has been measured to be ~100 km s^{-1} so the timescale to cross the entire length of the blue outflow lobe (1′ ~ 18300 au at 321 pc) is only ~1000 years. Here we use the data from Ray et al. (2023) to show in Figure 6 that the spacing and structure of the jet knots is as short as ~ 5 yr. Taken together, this seems to imply that this protostar has built up its current mass of 0.08 M$_\odot$ over a period of ~1000 yr in multiple bursts every 5–10 yr, and is still growing in mass.

4.2. H I recombination lines as a tracer of accretion

High mass protostars: MIRI's potential to measure accretion rates for high-mass protostars has been provided by the analysis of IRAS 23385+6053 (d=4.9 kpc, Table 1) (Beuther et al. 2023; Gieser et al. 2023b), a region forming a 9 M$_\odot$ high-mass protostar (Cesaroni et al. 2019). The high spatial resolution of MIRI reveals that this source is actually a binary system (labeled A and B) with a projected linear separation of ~3300 au that can be resolved in the MRS short wavelength channels. Only the A source coincides with the extension of the millimeter continuum peak. The H I 7–6 Humphreys α line is detected at a 3–4σ level toward sources A+B. Follow up analyses reveal that most of the ionization comes from source A (Reyes et al., in prep.). Using the Rigliaco et al. (2015) relation for this line calibrated for low-mass T Tauri stars, an accretion luminosity of 140 L$_\odot$ can be inferred, which in turn gives an accretion rate of 2.6×10^{-6} M$_\odot$ yr^{-1}. Correcting this number for an estimated visual extinction of 30–40 mag based on the depth of the silicate feature, and using the McClure (2009) extinction law, increases the rate to ~10^{-4} M$_\odot$ yr^{-1}. For such a high extinction, the bulk

Table 2. Hydrogen line measurements and accretion rates.

Source	A_V	$L_{\rm bol}$	$M_\star$	$R_\star$	$L_{\rm acc}/L_{\rm bol}$	Flux H I 7–6	$L_{\rm acc}$ from H I 7–6	$\dot{M}_{\rm acc}$ from H I 7–6	$\dot{M}_{\rm acc}$ from $L_{\rm bol}$
	(mag)	($L_\odot$)	($M_\odot$)	($R_\odot$)		(erg cm^{-2} s^{-1})	($L_\odot$)	($M_\odot$ yr^{-1})	($M_\odot$ yr^{-1})
TMC1-W	18	0.35	0.20	2.5	0.5	$4.0 \pm 1.1 \times 10^{-15}$	1.2×10^{-2}	4.9×10^{-9}	7.2×10^{-8}
TMC1A	33	2.70	0.56	2.5	0.5	$6.8 \pm 2.7 \times 10^{-14}$	4.5×10^{0}	6.6×10^{-7}	2.0×10^{-7}
SerpSMM3	50	27.5	0.50	4.0	1.0	$<5.4 \times 10^{-16}$	$<2.0 \times 10^{-2}$	$<5.2 \times 10^{-9}$	7.2×10^{-6}

Notes. A_V is measured from the silicate feature using $\tau_{9.7} \times 18.5$. $L_{\rm bol}$ is divided by the number of components in multiple systems. For TMC1A and TMC1-W the measured values of stellar properties are used, for SMM3 fiducial Class 0 values are adopted. $L_{\rm acc}/L_{\rm bol}$ is not a measured value but an assumption that goes into estimating $\dot{M}_{\rm acc}$ from $L_{\rm bol}$. All values have been corrected for extinction.

of the A+B sources' luminosity of 3×10^3 $L_\odot$ is indeed due to accretion. An analysis of H I in the full JOYS high-mass sample will be presented in Reyes et al. (in prep.).

Low-mass protostars: An early JOYS example for low-mass protostars is provided by TMC1, a Class I binary located in Taurus at 142 pc distance (Tychoniec et al. 2024). Several H I recombination lines are detected toward both sources, with the strongest lines seen toward TMC1-W. The fact that these lines are only seen on top of the infrared continuum, i.e., at the source position, suggests that there is no or little jet contribution. Table 2 lists the inferred accretion rate, using the relation by Rigliaco et al. (2015) and correcting for extinction and contamination by water lines (see below and update by Tychoniec, in prep.). The value of 5×10^{-9} $M_\odot$ yr^{-1} is an order of magnitude lower than that derived from the bolometric luminosity $L_{\rm bol}$ also listed in Table 2 obtained assuming the relation $\dot{M}_{\rm acc} = fR_* L_{\rm bol}/GM_*$ holds. Here $f = L_{\rm acc}/L_{\rm bol}$ is the fraction of the luminosity that is ascribed to accretion. The low value found for TMC1-W suggests that it is currently in a low accretion state, perhaps similar to the low-mass Class 0 source IRAS 16253-2429 studied with JWST in the IPA program (Narang et al. 2024).

Another well-studied nearby Class I source in Taurus within the JOYS sample is TMC1A (IRAS 04365+2535). This ~0.5 $M_\odot$ protostar has a striking blue-sided molecular disk wind imaged with ALMA (Bjerkeli et al. 2016) and has recently been studied with JWST-NIRSpec by Harsono et al. (2023) revealing a collimated jet in [Fe II] 1.644 µm. Using the NIRSpec Paβ and Brγ lines and assuming that all the luminosity comes from protostellar accretion, very low rates of 2×10^{-12} and 3×10^{-9} $M_\odot$ yr^{-1} have been reported (Harsono et al. 2023). We note that neither value is corrected for extinction, which may also be responsible for the differences between the two diagnostics.

We can revisit the TMC1A case with our MIRI data since the 7–6 Humphreys α line at 12.37 µm is detected and suffers much less from extinction (Fig. 7). Moreover, the extinction can be estimated, albeit with considerable uncertainty, to be $A_V \approx 30$ mag from the silicate optical depth using $A_V = 18.5 \times \tau_{9.7}$. Using the same relation of Rigliaco et al. (2015) and correcting for extinction and water, a mass accretion rate of 6.6×10^{-7} $M_\odot$ yr^{-1} is found for TMC1A. This value is much higher than inferred from the uncorrected NIRSpec data and consistent with those estimated from the bolometric luminosity of the source and the need to build up a ~1 $M_\odot$ star in less than 1 Myr. It agrees well with accretion rates found by Fiorellino et al. (2023) for a large sample of much less extincted Class I sources based on Brγ data. The case of SMM3 is discussed below in Sect. 5.1. We stress that all accretion rate determinations depend strongly on the assumed extinction toward the protostellar embryo; a detailed discussion of the different extinction diagnostics is presented in Appendix G.

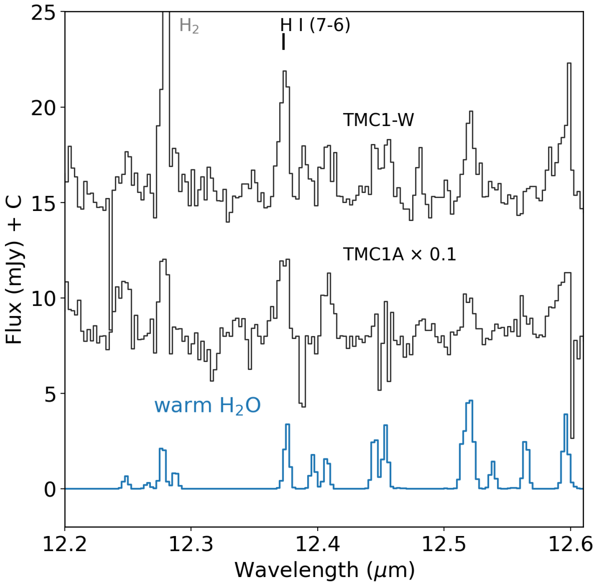

Fig. 7. Comparison of the H I 7–6 Humphreys α line detected in the JWST-MIRI spectrum of the Class I source TMC1A with that seen toward TMC1-W (Tychoniec et al. 2024). A warm water spectrum at T=485 K is also shown (best fit for TMC1-W, van Gelder et al. 2024a) to illustrate that water emission can contribute to the H I 7–6 feature.

The H I 7–6 line at 12.372 µm used to determine these accretion rates is actually located near another recombination line, the H I 11–8 transition at 12.387 µm. The *Spitzer*-IRS could not resolve these lines, but MIRI-MRS can (Franceschi et al. 2024); the empirical relation of Rigliaco et al. (2015) is therefore taken to refer to the sum of both components. Also, as Figure 7 shows, the H I flux can be contaminated by warm water emission. However, the fluxes of TMC1-W and TMC1A cannot be fully explained by water: H I still dominates the 12.37 µm emission. Any water contribution can be subtracted using a fit to the H$_2$O emission over a larger wavelength range, as has been done for the values listed in Table 2 (Rigliaco et al. 2015; van Gelder et al. 2024a). An updated water-corrected relation is presented in a recent JWST-based study by Tofflemire et al. (2025), which gives consistent results for our sources.

Another complication is that not all H I recombination line emission need to originate from accretion onto the protostars and that scattering can complicate the extinction correction at shorter wavelengths (Delabrosse et al. 2024). Brackett α NIRSpec

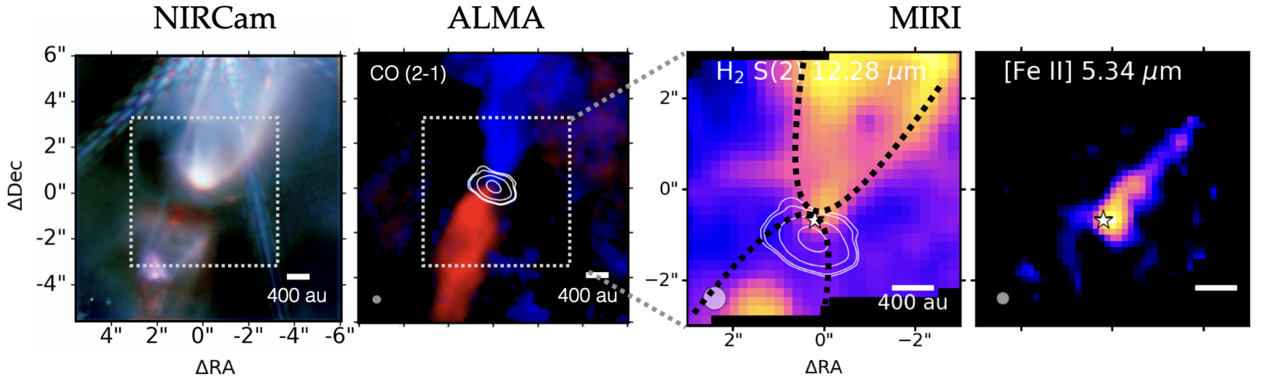

Fig. 8. Comparison of JWST and ALMA data for the Class 0 protostar Serpens SMM3. From left to right, (1) JWST NIRCam image of SMM3 using a combination of the F210M (blue), F360M (green), and F480M (red) filters from archival data of PID 1611; (2) ALMA image of the CO J=2–1 red and blue outflow lobes in the inner 10″ × 10″ together with the dust disk at 1.3 millimeter continuum emission (contours) (Tychoniec et al. 2021); (3) JOYS MIRI-MRS maps of the H_2 S(2) line at 12.28 μm, with the dotted line outlining the scattered light cavity seen with NIRCam; and (4) the [Fe II] line 5.34 μm, both in a zoomed-in region of 6″ × 6″. Beam sizes are indicated in the lower-left corner of each panel.

imaging shows bright extended emission in some sources that is clearly associated with shocks in protostellar jets (Federman et al. 2024; Neufeld et al. 2024). VLTI-Gravity observations that resolve the Brackett γ emission in Class I/II T Tauri systems also demonstrate that winds and outflows commonly contribute to the H I emission at the scale of the inner disk (GRAVITY Collaboration 2023). Also, the Rigliaco et al. (2015) relation was derived from *Spitzer* data in large apertures that could have included extended H I emission, thereby assigning all the H I to accretion rather than a mix of accretion and ejection. Thus, the inferred accretion rates from H I should be considered as upper limits. A combination of spatially and spectrally resolved H I lines observable with MIRI and NIRSpec tracing a range of temperatures and densities, combined with H I excitation calculations (Kwan & Fischer 2011), is needed to disentangle the components.

5. Protostellar jets, winds, and outflows

Studies on the MIRI-MRS jet, wind, and outflow have been published within JOYS for the high-mass protobinary IRAS 23385+6053 (Beuther et al. 2023; Gieser et al. 2023b) and for the low-mass protobinary system TMC1 (Tychoniec et al. 2024). Moreover, the entire blue outflow lobe and part of the red lobe of HH 211, 1′ in extent, has been mapped with the MRS (Caratti o Garatti et al. 2024). The latter study thus includes also the bow shocks at the tip of the outflow, in addition to the jets and winds closer to the protostar. Figure 1, Sect. 2 and Appendix B.2 provide definitions of these terms as used in this paper and scientific background.

5.1. The Class 0 source Serpens SMM3 as an example

Here we present the case of the Class 0 source Serpens SMM3 (d=439 pc, Table 1) to illustrate typical findings in MRS maps. SMM3 is, with 28 $L_{\odot}$, among the most luminous of the low-mass sources in the JOYS sample. It has been imaged by ALMA in various molecular lines (Tychoniec et al. 2021, and refs cited) and has a relatively narrow CO outflow opening angle of $<20^o$. It is one of the few Class 0 sources with clear “knots” seen in CO and SiO about 8″ offset from the source along the jet (also called extremely high velocity (EHV) “bullets”). It also shows hints of a large embedded rotating disk, further discussed in Sect. 8. Finally, NIRSpec IFU data exist as part of JOYS+ (PID 1186) that can enhance the analysis in future studies, especially by observing more accretion tracers and ro-vibrational H_2 and CO lines (Le Gouellec et al. 2025).

MRS maps: Figure 8 (left) presents a NIRCam image of SMM3 over the inner 10″ × 10″ region together with an ALMA image showing the swept-up CO outflow as well as the SMM3 dust disk in millimeter continuum. The two right-hand panels highlight the inner 6″ × 6″ in the H_2 S(2) line at 12.28 μm and the [Fe II] line 5.34 μm. Only a single MRS pointing was obtained for this source, thus covering only part of the outflow. The [Fe II] image clearly reveals the collimated jet, whereas the H_2 line shows the wider-angle warm molecular gas inside the outflow cavity outlined by the NIRCam scattered light image. Mid-infrared emission is stronger in the blue lobe than in the red lobe due to enhanced extinction in the latter close to the source (see also below).

The MIRI images of various other atomic lines and of H_2 covered in the MRS data are presented in Figures 9 and 10, with the spatial resolution decreasing with wavelength from ~0.2″ at 5 μm to ~0.7″ at 25 μm. All four [Fe II] lines trace the blue part of the jet, even at the longest wavelength of 25.99 μm, but interestingly, the [S I] 25.25 μm line, which is close in wavelength, shows a more prominent peak on the red side of the outflow. This demonstrates that the lack of [Fe II] emission on the red side is real, and not just due to extinction; it could be due to lower excitation and shock conditions along the red-shifted jet. The intensity of all four [Fe II] lines is sensitive to density and shock velocity, although to different degrees (Hartigan et al. 1987; Hollenbach & McKee 1989). In particular, the [Fe II] 25.99 μm line is a fine-structure transition within the ground electronic state with the lowest critical density, similar to that of the observed [S I] 25.2 μm, yet this [Fe II] line is also not detected. This suggests that in addition to excitation, abundance differences also play a role: less Fe may have been returned to the gas phase on the red side by the shocks.

The [Ni II] and [Ne II] lines peak close to the source in the blue part of the jet (Fig. 9). For [Ni II] its limited extent in SMM3 may be due to its lower S/N, since in other still-unpublished JOYS sources it usually follows [Fe II]. In contrast, [Ne II] often shows more central emission, although it has a weak jet component as well for SMM3.

Figure 10 presents images of the various H_2 lines covered by the MIRI-MRS. Whereas the low-lying S(1) and S(2) lines trace the wide-angle wind, the images of the higher H_2 lines are much

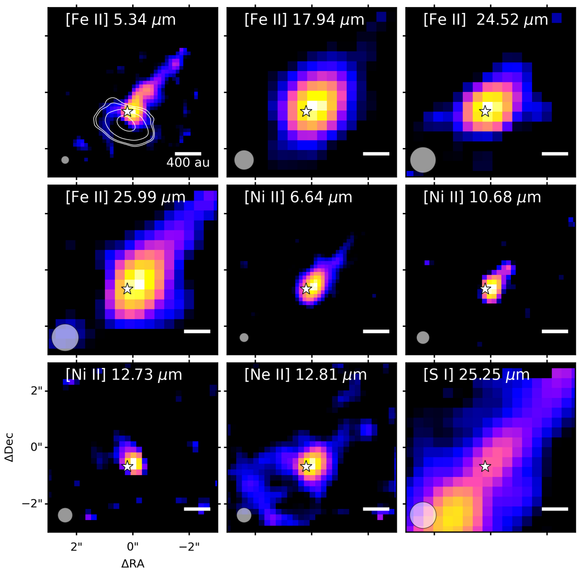

Fig. 9. Maps from MIRI-MRS of various atoms and ions toward the Class 0 protostar Serpens SMM3. The white contours in the top-left panel outline the dust disk seen in millimeter continuum. Beam sizes are indicated in the lower left corner of each panel. Each panel is scaled to the maximum emission of that species. The maximum and minimum colors are (in Jy km s^{-1}), from top left to bottom right: [Fe II] 5.34 (0.033, 0.003); [Fe II] 17.94 (0.84, 0.017); [Fe II] 24.52 (0.62, 0.025); [Fe II] 25.99 (1.86, 0.075); [Ni II] 6.64 (0.05, 0.002); [Ni II] 10.68 (0.006, 0.001); [Ni II] 12.73 (0.005, 0.001); [Ne II] 12.81 (0.017, 0.003); [S I] 25.25 (3.27, 0.033).

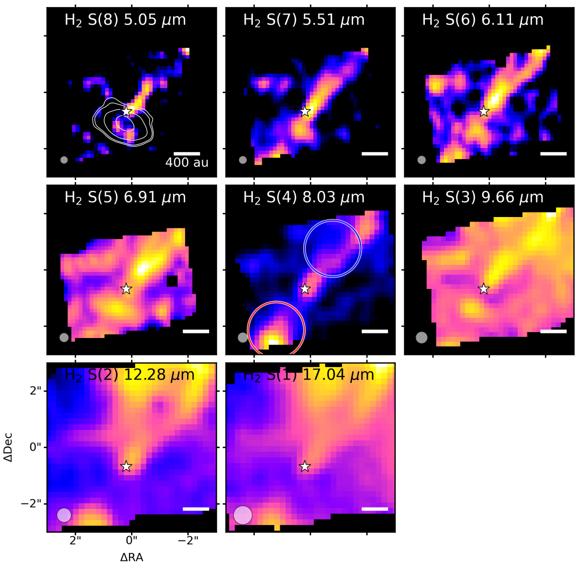

Fig. 10. Maps from MIRI-MRS of the various H_2 lines toward the Class 0 protostar Serpens SMM3. The white contours in the top-left panel indicate the dust disk seen in millimeter continuum. The red and blue circles on the S(4) image indicate the positions where the H_2 spectra and rotational diagrams have been extracted. The S(3) image at 9.66 μm is strongly affected by silicate extinction and the S(5) line at 6.9 μm by ice extinction; hence, their maps are more noisy. Beam sizes are indicated in the lower left corner of each panel. Each panel is scaled to the maximum emission of that species. The maximum and minimum colors are (in Jy km s^{-1}), from top left to bottom right: S(8) (0.008, 0.003); S(7) (0.033, 0.007); S(6) (0.013, 0.003); S(5) (0.026, 0.003); S(4) (0.089, 0.009); S(3) (0.035, 0.005); S(2) (0.090, 0.009); S(1) (0.084, 0.008).

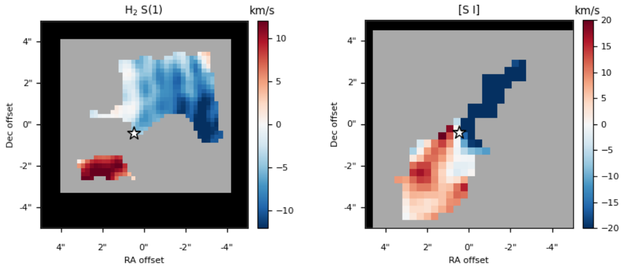

Fig. 11. MIRI-MRS moment-1 maps of the H_2 S(1) 17.0 μm and [S I] 25.25 μm lines toward Serpens SMM3 showing the ability of the MRS to distinguish the red- and blue-shifted gas. The velocities are relative to the source velocity of V_{LSR} = 7.6 km s^{-1}.

narrower and clearly trace the jet, as seen most prominently in the H_2 S(7) and S(8) lines at the shortest MIRI wavelengths of 5.51 and 5.05 μm. Here the images are sharpest and comparable in resolution to those of the [Fe II] 5.34 μm. Moreover, as also seen in Fig. 8, H_2 is clearly detected in the red outflow lobe as well, even at 5.5 μm. In fact, the H_2 S(4) line reveals two new "knots" on opposite sides of the source. Interestingly, there appears to be a slight tilt between the warm H_2 low-J images and that of the hot H_2 and atomic lines. No HD is detected at either position, consistent with the fact that the H_2 lines in SMM3 are not as bright as those in HH 211 where several HD lines are seen (Francis et al. 2025, see also Appendix B). Figure 11 presents the moment-1 map of the H_2 S(1) and [S I] 25 μm lines, clearly separating the red and blue parts in [S I]. Radial velocities of ~20 km s^{-1} are seen for H_2 and [S I].

Taken together, these data suggest that – like for HH 211 – the SMM3 jet has a "nested" structure with an ionized core surrounded by a molecular layer. This ionized core, however, appears on just one side of the outflow. Evidence of a wide-angle wind is found as well in low-J H_2 lines. This example also shows that the full suite of atomic, ionic and molecular lines is needed to reveal the physical and chemical structure of the outflow.

H_2 excitation and extinction determination: H_2 line fluxes have been extracted near two "knot" positions in a ~1″ aperture and put in a rotational diagram. The results for the blue and red positions are presented in Figure 12. As has been commonly found, also from ISO and *Spitzer* data (e.g., van Dishoeck 2004; Neufeld et al. 2006; Maret et al. 2009; Giannini et al. 2011; Gieser et al. 2023b), the upper level column densities derived from the S(3) line clearly fall below the trend of the other lines due to additional extinction by the silicate feature in the envelope. This deficit can therefore be used to infer the overall extinction in combination with an assumed overall extinction curve. Here the KP5 extinction curve of Pontoppidan et al. (2024a) has been used which has a somewhat stronger silicate feature than the McClure (2009) extinction curve.

At least two temperature components are needed to fit the remainder of the H_2 lines, consistent with previous findings (see above references). Using a procedure to obtain a simultaneous best fit for the two temperatures plus ortho-to-para ratio (OPR) and extinction results in the values indicated in the panels (Francis et al. 2025). The warm temperature is typically ~600 K, whereas the hot temperature is ~2000–3000 K. The OPR ratio is 2.0–2.5, close to the high temperature value of three. Interestingly, the extinction is found to be only slightly higher for the red lobe, A_V ≈ 25 mag, versus 15 mag for the blue lobe (Fig. 12).

The temperature structure as derived from H_2 can vary along the outflow axis, but also across it. Indeed, the fact that the

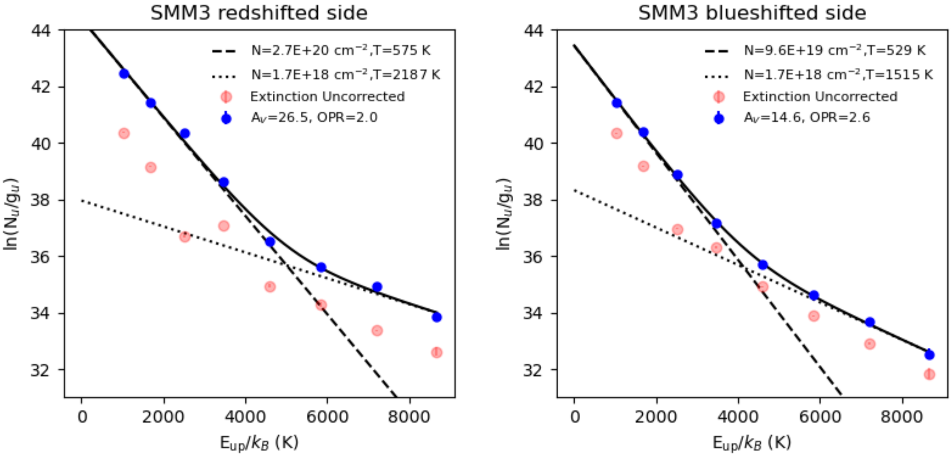

Fig. 12. Rotational diagrams of H_2 at the blue (left) and red (right) lobes using spectra extracted at the positions indicated in Fig. 10. The light red points indicate the values before extinction correction, the full blue points after extinction correction. Two temperatures and an OPR have been fitted to the extinction-corrected fluxes.

low-J H_2 lines have a wider opening angle than the high-J lines indicates that gas temperatures decrease away from the jet axis (Tychoniec et al. 2024; Caratti o Garatti et al. 2024; Delabrosse et al. 2024). For the case of Serpens SMM3, the temperature of the warm component decreases from 600 K by about 100–150 K in an aperture centered close to the outflow cavity wall. Ultimately, mapping of the temperature structure of the wind may put constraints on the heating mechanisms and thereby also its launching mechanisms.

Mass loss rates: The H_2 column densities found from the rotational diagrams can be used to calculate mass loss rates through

$$\dot{M}_{\rm H_2} = 2\mu m_{\rm H}(\overline{N}A)(v_{\rm tg}l_{\rm tg}), \tag{1}$$

where $\overline{N}$ is the warm H_2 column density averaged over the emission area A (assumed to be circular and equal to the area over which the spectrum has been extracted, Figs. 10 and 12), v_{tg} is the tangential velocity and $l_{\rm tg}$ is the projected knot size. The width of the blue-shifted knot $l_{\rm tg}$ is measured to be 625 au at the position of the extracted spectrum from the lowest J lines, whereas the line-of-sight velocity is –18 km s^{-1} based on the average of the velocity shifts from the H_2 S(1) to S(4) lines that best trace the warm component (Fig. 11). Assuming an inclination of 50^o estimated from CO millimeter maps (Yıldız et al. 2015) and taking the extinction corrected warm H_2 column of 9.6×10^{19} cm^{-2} derived from the rotation diagram (Fig. 10), gives a mass loss rate from the warm H_2 component of $\dot{M}_{\rm H_2} = 1.4 \times 10^{-7}$ $M_\odot$ yr^{-1}. The uncertainty is a factor of around two due to uncertainties in inclination and extinction. This value is a factor of a few lower than the mass loss rate of 7×10^{-7} $M_\odot$ yr^{-1} found for HH 211 from warm H_2.

The advantage of using H_2 is that the total column of hydrogen nuclei is measured directly, as is its velocity, so no density or velocity needs to be inferred indirectly from diagnostics and models. Mass loss rates can also be derived from the atomic lines, as shown in detail for the case of HH 211 by Caratti o Garatti et al. (2024). Appendix D describes slightly different methods used here to estimate ejection rates from the extinction-corrected [Fe II] 26 µm line (Watson et al. 2016), the [Ne II]+[S I] lines combined with shock models from Hollenbach & McKee (1989) (Tychoniec et al., in prep.) and from the [O I] 63 µm line (Hollenbach 1985).

These atomic diagnostics give values of $\dot{M}_{\rm jet}$ that are slightly lower than derived from H_2 by a factor of two to three when applied to one outflow lobe (Appendix D). Taking into account the factor of roughly three higher velocities of the atomic component compared with H_2, the atomic and molecular jets seem to provide comparable thrust (momentum flux) $\dot{M} \times v_{\rm tot}$ to drive the material in the SMM3 system; the molecular component is not as dominant here as it has been found to be for HH 211 (Caratti o Garatti et al. 2024).

When summed over the entire MRS channel 4 $7'' \times 7''$ FoV, the [Fe II] 26 µm mass loss rate is $\dot{M}_{\rm jet} = 4.0 \times 10^{-7}$ $M_\odot$ yr^{-1}. This value is within a factor of two of that based on the *Herschel*-PACS [O I] 63 µm luminosity in a ∼9″ spaxel (Mottram et al. 2017). We note that the [Fe II] 26 µm relation of Watson et al. (2016) has been calibrated against [O I] 63 µm for a large sample of sources and that in general the [O I] value should be considered as an upper limit (see Appendix D).

It is interesting to compare these mass outflow values with mass accretion rates. No hydrogen recombination lines are detected for SMM3 but the upper limit on the H I 7–6 line constrains the mass accretion rate to a low value of $< 5 \times 10^{-9}$ $M_\odot$ yr^{-1}, assuming an extinction of 50 mag (see Table 2). An alternative rough estimate can be obtained assuming that the observed bolometric luminosity is mainly due to accretion for Class 0 sources like SMM3. Using the relation given in Sect. 4, Mottram et al. (2017) find 1.2×10^{-5} $M_\odot$ yr^{-1}, close to our value in Table 2. The large difference with the upper limit from H I is either caused by an underestimate of the H I extinction due to the big massive disk of SMM3 making it more difficult to peer close to the star, or by the magnetospheric accretion mode not being applicable to Class 0 sources (and thus the H I relations). Alternatively, not all luminosity needs to come from accretion. If it does, the inferred $\dot{M}_{\rm jet}/\dot{M}_{\rm accretion} \approx 0.01$. This value is on the low side of previous determinations for other Class 0 and I sources (Watson et al. 2016).

Taken together, this SMM3 example and the comparison of various methods to derive mass outflow and accretion rates emphasize the need for high quality spatially resolved observations of each of the atomic, ionic and molecular components that are now available with JWST, not only with MIRI but also with NIRSpec (Le Gouellec et al. 2025). They also indicate that earlier rates based on large aperture data need to be used with caution, especially based on [O I]. Similar comparisons for other

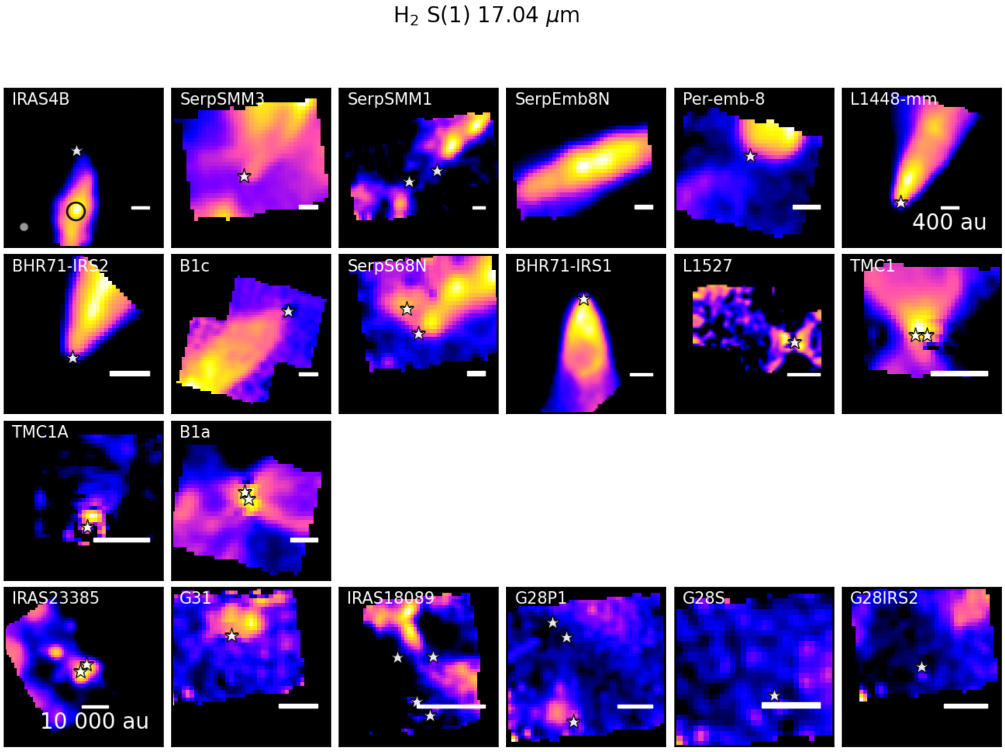

Fig. 13. Maps from MIRI-MRS of the H_2 S(1) line at 17.03 μm toward all JOYS sources. The top three rows show the low-mass protostars in order of increasing $T_{\rm bol}$, whereas the bottom row shows the high-mass protostars. The white star(s) or arrow in each panel indicate the position of the protostar(s); for low-mass protostars those are derived from millimeter interferometry. A scale bar of 400 au is shown in each low-mass protostar panel, and a bar of 10 000 au in each high-mass protostar panel. The beam size is indicated in the lower left corner of the first panel. The maximum colors in each panel (in Jy km s^{-1}) from the top left to bottom right for low mass are as follows: 0.59, 0.12, 0.03, 0.14, 0.08, 0.25, 0.08, 0.025, 0.041, 0.11, 0.006, 0.18, 0.31, 0.064. For high mass, they are 0.21, 0.02. 0.06, 0.021, 0.023, 0.027.

Class 0 sources are needed to assess the usefulness of each of the methods and calibrate them better to trace mass loss and accretion.

5.2. Morphologies: Which line traces what?

The next step is to compare the Serpens SMM3 results with those of other sources studied with JWST. Table D.1 in Appendix E summarizes the main atomic and molecular lines that are seen in the MIRI spectra of protostars, together with their origin. It is well known that elements can be divided into volatile (e.g., noble gases), moderately volatile or semi-refractory (e.g., S, Cl), and refractory elements (e.g., Fe, Ni, Co) depending on their condensation temperatures (Lodders 2003). Observations of elemental abundances in diffuse clouds using UV absorption lines show that the amount of depletion strongly varies between these categories, with volatile elements like Ne and Ar basically undepleted and refractory elements like Fe, Ni and Co heavily depleted by up to two orders of magnitude due to their incorporation into dust (Savage & Sembach 1996; Jenkins 2009). The semi-refractories are somewhere in between. The MIRI-MRS line images can indeed be divided along these different categories.

Figures 13 and 14 provide an overview of the H_2 S(1) line and one low-excitation fine-structure line of a refractory element, [Fe II] 25.99 μm, for the entire JOYS low- and high-mass protostar sample. In these figures, the low-mass sources NGC 1333 IRAS4A, SVS4-5 and HH 211 have not been included (see Sect. 3); hence there are 14 rather than 17 low-mass panels. The full set of all line images will be presented in future papers, but the trends for low-mass sources are similar to those presented for Serpens SMM3.

A common theme is that a narrow jet is seen prominently in the [Fe II] lines at 5.34, 17.92, 24.52 and 25.99 μm, as well as in other refractory species, such as [Ni II] 6.63 μm and [Co II] 10.52 μm, which have been returned to the gas phase by shocks. Notably, [Fe I] 24.04 μm is exclusively detected in some Class 0 sources, not in Class I sources, and always in the jet. This finding is consistent with jets becoming more ionized with protostellar evolution (Nisini et al. 2015). The detection of both Fe and Ni in jets points to the presence of iron/nickel grains which do not have spectral features: this is the only way to discover the nature of Ni-containing dust (Henning 2010; Manfroid et al. 2021).

Among the semi-refractories, the [S I] 25.24 μm line is bright and always elongated in the jet direction for Class 0 sources, where it also shows up prominently in bow shocks, like in SMM3. As for the refractories, it has been returned to the gas by shocks but it usually follows H_2 more closely than [Fe II]. If detected in Class I sources, [S I] emission is always compact on disk scales, and no longer associated with any jet (e.g., Tychoniec et al. 2024). In this context it has been suggested that sulfur-bearing species trace accretion shocks onto the disk (e.g., Sakai et al. 2014), but no convincing indications have yet been found that this is the case for [S I] (see Sect. 8). A similar trend is seen with the other moderately volatile element [Cl I] 11.33 μm, but this line is much fainter so its detection is not clear for many targets.

Lines of the noble gases Ne and Ar show a mixed behavior: the strong [Ne II] 12.81 μm line often follows the jet, but it may also have a compact, spatially broader component centered close

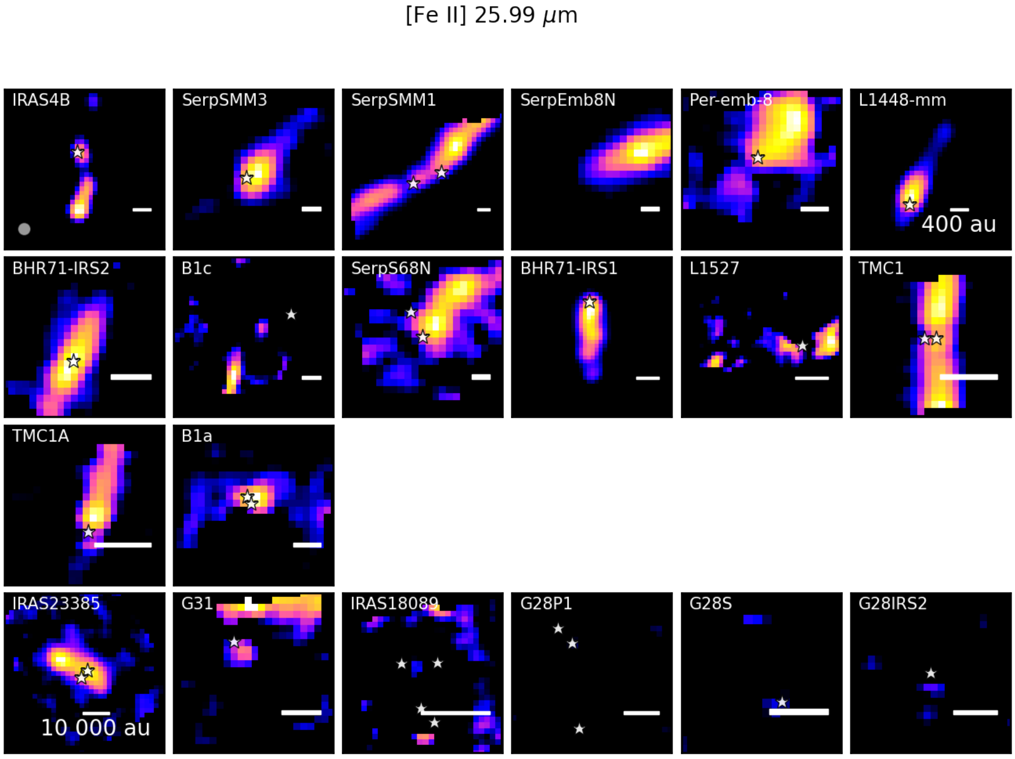

Fig. 14. Maps from MIRI-MRS of the [Fe II] $^4F_{7/2}$–$^4F_{9/2}$ line at 25.99 μm toward all JOYS sources. The top three rows show the low-mass protostars in order of increasing $T_{\rm bol}$, whereas the bottom row shows the high-mass protostars. The white star(s) or arrow in each panel indicate the position of the protostar(s); for low-mass protostars those are derived from millimeter interferometry. A scale bar of 400 au is shown in each low-mass protostar panel, and a bar of 10 000 au in each high-mass protostar panel. The bright [Fe II] emission seen at the edges of some of the high-mass images are real. The beam size is indicated in the lower left corner of the first panel. The maximum colors in each panel (in Jy km s^{-1}) from top left to bottom right for low mass are as follows: 1.18, 1.89, 15.65, 2.85, 0.62, 6.97, 1.41, 0.21, 0.56, 42.63, 0.17, 2.00, 3.72, 1.26. For high mass, they are 0.79, 0.80, 0.80, 0.80, 0.80, 0.80.

to the source, likely tracing the X-ray or (E)UV-irradiated cavities and cavity walls (see Figure 9 and Gieser et al. 2023b for the high-mass source IRAS 23385). The same holds for [Ar II] at 6.98 μm, but since its line is weaker than that of [Ne II] it is more difficult to separate the components. In contrast, [Ne III] 15.56 μm and [Ar III] 8.99 μm are primarily detected in Class I sources where they show only a moderately extended component, plausibly tracing the ionizing radiation (see also Gieser et al. 2023b; Tychoniec et al. 2024). The images of the noble gases demonstrate that not just elemental depletion but also local conditions (e.g., what is required to ionize Ne and Ar) determine the emission pattern.

Heated dust is detected through 20 μm continuum emission in some Class 0 sources such as HH 211, indicating that dust is launched in the jet (Caratti o Garatti et al. 2024). The question whether that dust is subsequently destroyed or not by shocks requires comparison of one of the refractory elements with a non-refractory one. Typically, sulfur lines are used for the latter (Nisini et al. 2002). However, the depletion behaviors of S and Cl are not yet well understood (see also above discussion): both species are undepleted in diffuse clouds with A_V <1 mag (Jenkins 2009), but in dense clouds the bulk of S has been transformed into a more refractory component (e.g., Kama et al. 2019). Depletion of chlorine appears to be more modest in dense clouds based on observations of HCl (Blake et al. 1986). Thus, it is not clear a priori which element to take as the undepleted reference in determining the amount of depletion of elements in shocks. One of the noble gases (e.g., neon) that does not suffer any depletion could be a cleaner reference probe for abundances, as long as their line flux does not depend sensitively on other physical parameters. Another possibility for the case of S is to take H_2 itself (Anderson et al. 2013).

In the youngest Class 0 protostars, H_2 shows a mix of wide-angle wind and jet emission. The narrow jet is seen in the higher excitation H_2 lines such as S(5) and S(7), whereas emission from the lower-lying H_2 lines is dominated by the wide-angle wind (Fig. 10). For Class I sources, all H_2 lines fill the outflow cavity with the opening angle of the disk wind increasing with decreasing excitation (i.e., J level) (Tychoniec et al. 2024). Molecular lines from CO, OH, HCO^+ and CO_2 are also detected associated with the outflow (Tychoniec et al. 2024; Narang et al. 2024; van Gelder et al. 2024a) (see also Sect. 6).

In conclusion, warm molecular gas is clearly present within the outflow cavity, not just as part of the cavity wall, and its velocity structure indicates that the gas is moving in the red- or blue-shifted directions. Whether H_2 lines are indeed tracing disk winds close to the source or simply gas inside the cavity that is heated and put in motion otherwise (e.g., by internal jet shocks or shocks with ambient material) would require velocity resolved line profiles and spatially resolved H_2 temperature and column density maps. Farther removed from the source, H_2 may also be mixed in by turbulence from the entrained outflow gas, and that gas may also be heated by UV radiation along the outflow cavity walls (e.g., Yıldız et al. 2015).

The atomic and molecular line images for the high-mass source IRAS 23385 +6053 show similar trends, both in refractories, volatiles and H_2 (Beuther et al. 2023; Gieser et al. 2023b). The patterns for the other high-mass sources are less clear from the images presented here: IRAS 18089 -1732 has a cluster of high-mass sources resulting in bright H_2 emission throughout the region, whereas the IRDC G28 positions show much weaker emission. The high-mass outflows and accretion will be studied in future papers.

5.3. Comparison with other JWST studies

The JOYS findings are consistent with results of low-mass Class 0 protostars from a number of other JWST programs. Early MIRI-MRS examples are the low-mass Class 0 sources IRAS 15398-3359 (CORINOS program; Yang et al. 2022; Salyk et al. 2024) (1.5 $L_\odot$) and IRAS 16253-2429 (0.2 $L_\odot$) (IPA program; Narang et al. 2024). Also, NIRSpec images of [Fe II] and H_2 (Federman et al. 2024) as well as CO (Rubinstein et al. 2024) ro-vibrational lines have been presented for all five IPA sources from low to high mass, for the Class 0 binary Serpens S68N (Le Gouellec et al. 2024) and for the Class I source TMC1A (Harsono et al. 2023). MIRI and NIRSpec images of the Class I source HH 46 IRS (16 $L_\odot$) have been published by Nisini et al. (2024) as part of PROJECT-J; their Table 1 provides a useful overview of all atomic lines detected in HH 46.

A common finding of all of these early MIRI and NIRSpec results across low-mass Class 0 and I sources as well as high-mass protostars, is the presence of highly collimated jets, most notably seen in the various [Fe II] lines and in the highest excitation H_2 pure rotational and ro-vibrational lines. Wider angle winds are traced by the lowest H_2 pure rotational lines, as found within JOYS (Tychoniec et al. 2024). Lines of other refractory species as well as noble gas (Ne, Ar) lines are also commonly detected, with the latter species often showing a different distribution from either [Fe II] or H_2, consistent with what is found in JOYS. Analyses of the nested physical structure of the Class I source DG Tau B and a small sample of young Class II jets and winds are presented in Delabrosse et al. (2024); Pascucci et al. (2025). Some H I emission is seen also off source in both NIRSpec and MIRI data (e.g., Neufeld et al. 2024), demonstrating that not all the H I recombination line luminosity is due to the accretion column onto the star.

6. Hot cores and dense molecular shocks: Chemistry

MIRI-MRS spectra of the first observed JOYS target, the high-mass binary protostar IRAS 23385+6053, demonstrated that many gas-phase molecular lines can be detected at the source positions and that not just *Q* branches but also individual *P*- and *R*- branches (see Figs. 4 and 5) can be seen (Francis et al. 2024). The MIRI-MRS spectra at central positions of the low-mass JOYS sources have been analyzed in a recent overview paper of molecular lines by van Gelder et al. (2024a). Rich spectra containing lines of up to 13 different molecules (including isotopologs) are seen toward three out of 16 sources with mid-infrared continuum, two in emission (L1448-mm and BHR71-IRS1) and one in absorption (B1-c). Other sources show primarily H_2O, CO, CO_2 and/or OH, but not C_2H_2, HCN, SO_2 or SiO. The Serpens SMM3 source, discussed extensively in Sect. 5 as an example protostellar source, shows only CO_2 emission (Fig. 15) but no H_2O. For most sources and molecules, no significant (>10 km s^{-1}) velocity offsets are seen, except for BHR71-IRS1 (all lines) and L1448-mm (H_2O and SiO). We here highlight the main results for both low- and high-mass sources and put them in the context of the various scenarios of hot core chemistry, dense molecular shocks, and winds (see Sect. 2.3 and Appendix B.2 for background information).

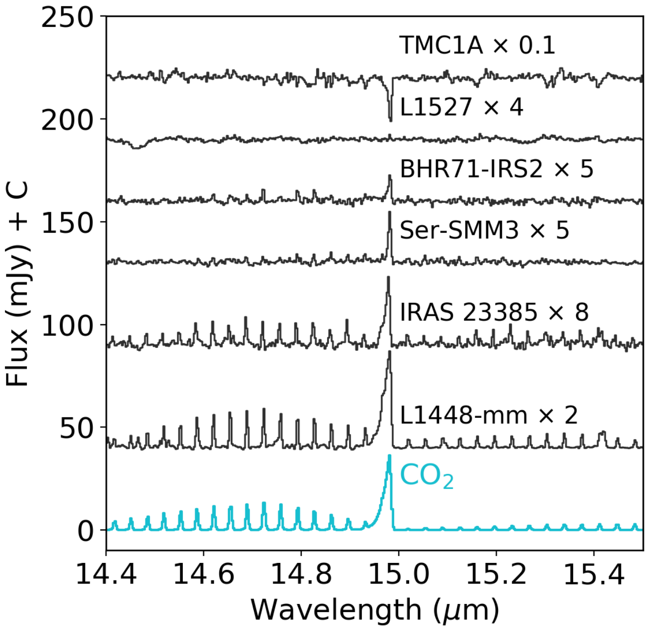

Fig. 15. Comparison of CO_2 15 μm emission and absorption toward several low- and high-mass protostars. The bottom panel shows a model spectrum at *T*=120 K (best fit for L1448-mm), with the *P*-branch extincted by CO_2 ice.

6.1. From CO_2 to SO_2: Cool emission

CO_2: Gas-phase lines of CO_2 at 15 μm are seen in emission toward IRAS 23385+6053 (Beuther et al. 2023), rather than in absorption as found for the sample of high-mass protostars surveyed with ISO-SWS (Boonman et al. 2003b). This difference is likely due to the much higher spatial resolution of JWST, being able to detect the weak emission on source, whereas any emission in the large ISO-SWS beam was overwhelmed by the larger scale absorption against the extended infrared continuum. For IRAS 23385, the resolved *R*− and *Q*− branches provide an accurate temperature of ∼120±10 K (Francis et al. 2024). One early lesson is that gas-phase lines can be differentially affected by foreground ice absorption; this holds in particular for the *P*−branch lines of CO_2 being obscured by CO_2 ice, but the same effect is also seen for other species such as SO_2 and H_2O in the 6–8 μm range, in addition to the overall extinction (van Gelder et al. 2024b). This finding also puts direct constraints on the location of the emission: it must originate from behind where the bulk of the ice is located.

Figure 15 shows a blow-up of the gas-phase CO_2 detections in several low-mass sources at their central position in comparison with IRAS 23385. CO_2 is seen in 11 out of the 16 sources studied in van Gelder et al. (2024a), with four out of 11 in absorption (see also Tychoniec et al. 2024). Where detected, the CO_2 emission is cool, as in IRAS 23385, with typical rotational temperatures of 100–200 K (compare with Fig. 5). For CO_2 in absorption, the temperatures are somewhat higher, up to 300 K. The temperatures derived from CO_2 emission in protostars are lower than the values up to ∼400 K found in protoplanetary disks (e.g., Grant et al. 2023; Vlasblom et al. 2024). Also, the

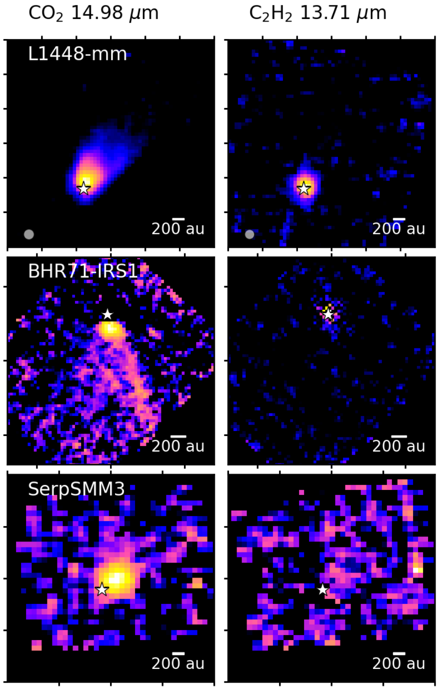

Fig. 16. Maps of CO_2 15 μm and C_2H_2 13.7 μm emission toward three low-mass sources. CO_2 is generally extended along the outflow, whereas C_2H_2 is centered on source, whose location is indicated by the white star. The beam size is indicated in the lower left corner of the top panels.

hot bands are never detected in protostars, consistent with low temperatures and lower densities (see Fig. 5).

Since CO_2 does not have a permanent dipole moment, the rotational populations in $\upsilon = 0$ should be thermalized and reflect the kinetic temperature of the gas. The rotational populations in $\upsilon = 1$, measured with JWST, should be similar if infrared pumping is indeed the main mechanism for exciting the molecule (see Sect. 3.5). Several findings therefore argue in favor of a hot core origin of CO_2 rather than in shocks (van Gelder et al. 2024a): (1) temperatures of 100–200 K consistent with ice sublimation; (2) lack of a velocity shift compared with the source velocity; (3) similar gas and ice CO_2/H_2O abundance ratios, and (4) location of the emission behind the ice absorption, i.e., closer to the protostar.

We note, however, that in some sources with prominent outflows CO_2 emission is also found to be extended along the outflow over distances up to 1000 au, as illustrated in Figure 16 (see also Boonman et al. 2003c; Sonnentrucker et al. 2007). One likely scenario is that the observed gaseous CO_2 away from the hot core is enhanced by ice sputtering of the dense and cold material along the outflow cavity walls or in a slow wind, and subsequently excited by infrared radiation from the source escaping through the outflow cavity. Warm gas-phase chemistry, especially through the CO + OH → CO_2 + H reaction, which is particularly effective in the 100–300 K range, can contribute as well (e.g., van Dishoeck et al. 2023).

C_2H_2 and HCN: Both molecules are detected toward IRAS 23385 and other high-mass protostars, as well as toward a few low-mass protostars (van Gelder et al. 2024a). Excitation temperatures from emission features are similarly low as for CO_2, 100–200 K, again lower than the values up to 600 K found for C_2H_2 and up to 900 K for HCN in protoplanetary disks around T Tauri stars (e.g, Grant et al. 2023; Temmink et al. 2024a; Schwarz et al. 2024; Colmenares et al. 2024; Arulanantham et al. 2025). In contrast with CO_2, neither of these two molecules are seen along the outflow (Fig. 16), or toward outflow positions well offset from the high mass protostellar sources as was the case in Orion (Boonman et al. 2003c). In low-mass outflows, such as HH 211, C_2H_2 and HCN are also not seen at any of the strong knot positions. There is one clear exception, the NGC 1333 IRAS4B shock, discussed in Sect. 6.3, and one other spot near Serpens SMM1. The fact that C_2H_2 and HCN are generally not extended makes a hot core origin most plausible for these molecules, with high temperature gas-phase reactions rather than ice sublimation dominating the formation of C_2H_2 and HCN (Francis et al. 2024; van Dishoeck et al. 2023) (see also models below).

CH_4: Methane gas is not readily seen toward protostars. Analysis of the JOYS low-mass sample reveals detections only in the two line-rich sources (B1-c, L14448-mm), as well as in the source SVS4-5, which is likely a disk (van Gelder et al. 2024a). In the former two sources, CH_4 is again cool, with temperatures of 100–200 K, suggesting a similar hot core origin as the other organic molecules. In disks around T Tauri stars, CH_4 is also seldom seen, with only two tentative detections reported (Colmenares et al. 2024; Temmink et al. 2025). In contrast, rich CH_4 line forests are prolific in many disks around very low-mass stars and brown dwarfs, even if not always easily distinguished due to line overlaps with C_2H_2 (e.g., Arabhavi et al. 2024; Kanwar et al. 2024).

H_2O: Water emission is surprisingly weak toward IRAS 23385, both through its vibration-rotation (5.5–7.5 μm) and pure rotational (>13 μm) lines. Toward one of the two sources in the binary, H_2O is also seen in absorption at a higher temperature of 550 K, more characteristic of winds or the inner warm disk midplane (Barr et al. 2020). H_2O emission and absorption is seen in other high-mass protostars as well (see example of IRAS 18089 in Sect. 7).

The low-mass protostars do not show prominent water emission lines, which is very different from the water emission forest seen in several more evolved Class II disks (e.g., Gasman et al. 2023; Pontoppidan et al. 2024b; Temmink et al. 2024a; Banzatti et al. 2025). However, upon close inspection, H_2O is detected in most low-mass protostars, either in the ro-vibrational band or in the pure rotational lines or in both, in absorption or emission (van Gelder et al. 2024a). These data indicate the presence of water at two temperatures: a cool temperature of 100–200 K, and a warmer component at 400–500 K, likely reflecting both a hot core and shock component. Figure 17 shows prominent water lines at longer wavelengths in the MIRI-MRS channel 4, comparing a few Class 0 and I sources with the line-rich Class II disk DF Tau (Grant et al. 2024). In particular, the quartet of lines around 23.8 μm has been found to be a good indicator of the presence of cold versus warm water as shown by Banzatti et al. (2023, 2025); Temmink et al. (2024a). The fact that the warm water lines are clearly suppressed in the protostellar sources indicates that the H_2O excitation temperature of water is indeed low. In contrast, the spectrum of a water-rich Class II source, DF Tau, has prominent warm and cold water lines in this wavelength range: all four lines rather than just two lines of the 23.8 μm quartet are seen.

We note that the two temperature components of water found in protostellar sources are not necessarily the same as the hot, warm and cold(er) components found in Class II disks where they have been associated with temperature gradients in the disk surface in the inner few au and water enhancement at the snowline (Banzatti et al. 2023, 2025; Gasman et al. 2023;

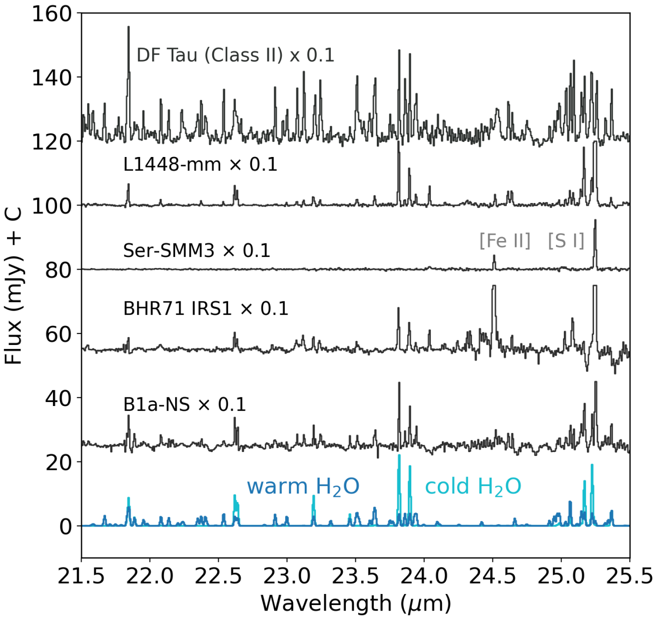

Fig. 17. Comparison of H_2O emission toward several low-mass protostars at long wavelengths in MRS channel 4. B1-a-NS is a Class I source, the other sources are Class 0 sources, including SMM3. The bottom panel shows warm and cold water model spectra at $T_{\rm rot}$=370 K (dark blue) and 160 K (light blue). The observed emission in protostars is dominated by the colder component. For comparison, the spectrum of a Class II disk, DF Tau, is shown at the top, illustrating that this disk has strong warm water emission (Grant et al. 2024).

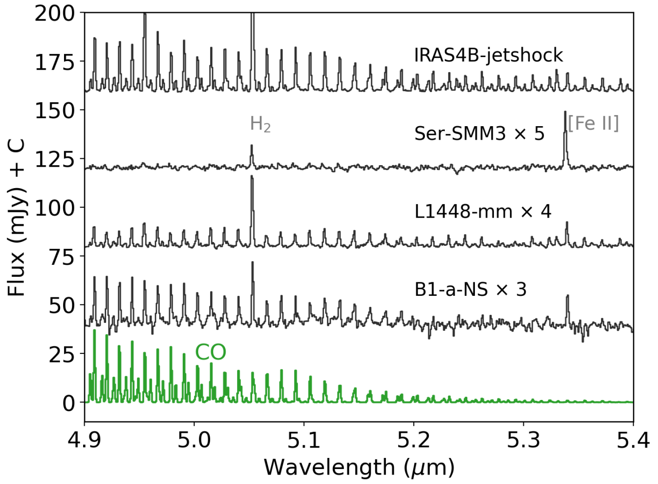

Fig. 18. Comparison of CO v = 1–0 5 μm emission toward several low-mass protostars. L1448 and SMM3 are Class 0 protostars, B1-a-NS is a Class I source, and the spectrum of NGC 1333 IRAS4B is taken at a shock knot position well off source (see Fig. 20). The bottom panel shows an optically thick CO model spectrum at T=1500 K.

Temmink et al. 2024a; Romero-Mirza et al. 2024): while there may be a similar water vapor enhancement in hot cores around 100 K, H_2O is likely to be subthermally excited at the much lower densities in protostellar environments, whereas the H_2O ro-vibrational band can be pumped by infrared radiation. Comparison with water in hot cores imaged with ALMA through lower excitation pure rotational lines of $H_2^{18}O$ and HDO (e.g., Persson et al. 2016; Jensen et al. 2019) will be done in future studies.

CO: The emission of CO is seen in about half of the MIRI spectra of protostars in the 4.9–5.2 μm range, showing the tail of the v =1–0 P−branch with $J_{\rm up}$ ≥ 23 (Fig. 18) (see also Salyk et al. 2024). When detected, it always indicates a high temperature (Fig. 4). A naive rotation diagram analysis assuming optically thin lines would imply ∼2000 K, but the actual kinetic temperature can be substantially lower, ∼1000 K if the CO emission is optically thick (see discussion in Herczeg et al. 2011; Francis et al. 2024; Rubinstein et al. 2024; Le Gouellec et al. 2025). Such emission could be consistent with the innermost disk region, as in Class II sources (e.g., Banzatti et al. 2022), but it can also be associated with the disk surface (Arulanantham et al. 2024) or shock knots (see Sect. 5) (Federman et al. 2024). Indeed, spectrally resolved ground-based CO data for Class I sources often show wind and outflow absorption in ^{12}CO v=1–0 profiles that could mask any emission in spectrally unresolved data (Herczeg et al. 2011). High extinction by the inner envelope could also hide CO emission in sources where it is not seen.

SO_2: Mid-infrared emission of SO_2 at 7.3 μm has been detected for the first time by JWST in a low-mass protostar (van Gelder et al. 2024b). It is seen toward the Class 0 protostar NGC 1333 IRAS2A, a source that is part of JOYS+ in program 1236 (PI: M. Ressler). Inspection of the full JOYS low-mass sample shows that this band is not commonly seen, only toward L1448-mm in emission and B1-c in absorption (van Gelder et al. 2024a).

Notably, SO_2 is one of the few molecules that can be observed with both JWST and ALMA since it has a permanent dipole moment. Interestingly, for IRAS2A the excitation temperature derived from the mid-infrared data, ∼100 K, is the same as that derived from the wealth of SO_2 millimeter lines imaged with ALMA on scales of 60 au radius as presented in van Gelder et al. (2024b) using data from program 2021.1.01578 (PI: B. Tabone). Similarly low temperatures are found for the two JOYS sources. A question then is to what extent this excitation temperature $T_{\rm rot}$ reflects the kinetic gas temperature $T_{\rm kin}$.

Within v=0, the level populations are determined by a mix of collisional (de-)excitation and radiative decay. A non-LTE excitation calculation using RADEX (van der Tak et al. 2007, 2020) with collisional rate coefficients from Balança et al. (2016) is adopted to compute $T_{\rm rot}$ and the difference between $T_{\rm kin}$ and $T_{\rm rot}$ as a function of kinetic temperature and H_2 density n. $T_{\rm rot}$ is obtained by fitting a rotation diagram to the model results for the same lines as observed with ALMA in IRAS2A. Figure 19 shows that at low densities ($<10^7$ cm^{-3}) the excitation is subthermal, $T_{\rm rot} << T_{\rm kin}$. However, typical envelope densities on scales of <100 au are 10^7–10^9 cm^{-3} (Jørgensen et al. 2004; Notsu et al. 2021) for which differences $T_{\rm kin} - T_{\rm rot}$ are smaller.

The temperatures derived from the MIRI-MRS data should be representative of the gas in which SO_2 resides. The number of molecules inferred from LTE slab models, however, is not. It is overestimated by a factor of 10^4 when compared with the ALMA results. The mid-infrared lines are clearly pumped by scattered IR radiation with a brightness temperature of ∼180 K, substantially higher than the rotational temperature (van Gelder et al. 2024b). When the infrared pumping is included, the number of molecules derived from the JWST and ALMA data are consistent. Combined with the small millimeter line width and lack of a velocity shift, a hot core rather than an accretion shock origin seems most likely for SO_2. This study emphasizes the synergy between JWST and ALMA for molecules with a dipole moment.

Although the importance of subthermal excitation and infrared pumping is highlighted here for the case of SO_2 in

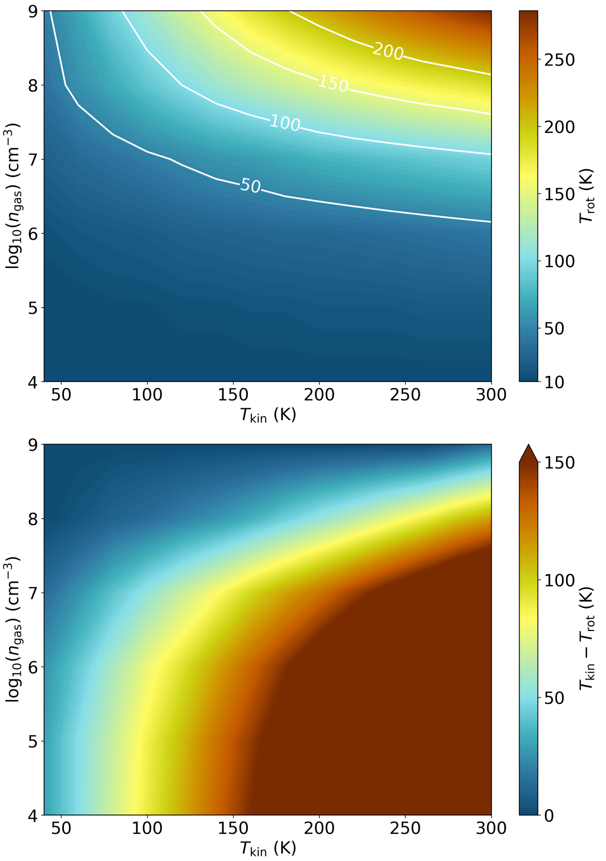

Fig. 19. Top: SO_2 rotational temperature T_{rot} within v=0 as function of kinetic temperature T_{kin} and density $n(H_2)$ obtained from non-LTE calculations. Bottom: Difference between T_{kin} and T_{rot}: large deviations are apparent at low densities ($<10^7$ cm^{-3}).

IRAS2A, Figure 19 is representative for other molecules with a dipole moment such as HCN and H_2O. The analysis in van Gelder et al. (2024a) also shows the importance of infrared pumping for other molecules and sources.

OH: As noted in Sect. 5, mid-infrared OH emission has been detected with *Spitzer* in bow-shocks (Tappe et al. 2008, 2012) and other environments with strong UV irradiation such as the surface layers of protoplanetary disks (Carr & Najita 2014). It is now also prominently seen with JWST in low-mass protostars at the source position (van Gelder et al. 2024a) and at (bow) shock positions (Neufeld et al. 2024; Caratti o Garatti et al. 2024), as well as in an irradiated disk (Zannese et al. 2024). Class II protoplanetary disks commonly show OH (e.g., Gasman et al. 2023; Temmink et al. 2024a; Schwarz et al. 2024; Vlasblom et al. 2025) although mostly at the longer wavelengths. In the high-mass JOYS sample, OH emission is only prominent in IRAS 23385 (Francis et al. 2024) although it is detected in some other sources (Reyes et al., in prep.).

The OH lines originate from extremely high rotational states, with rotational quantum numbers up to N=40 (E_{up} = 40 000 K). This phenomenon results from photodissociation of H_2O through its second electronically excited state, the $\tilde{B}$ state, producing OH in very high N states which then cascade down through pure rotational transitions to the ground state, a process that has been well studied in the laboratory and through quantum chemical calculations (e.g., Harich et al. 2001; van Harrevelt & van Hemert 2000) (see summary in Tabone et al. 2021). This process requires UV photons at 1140 –1430 Å and a wavelength range that includes Lyman α at 1216 Å, and it is thus a direct diagnostic of the strength of the UV radiation multiplied by the number of H_2O molecules (Tabone et al. 2023). The OH "prompt emission" occurs primarily at 9–11 μm with a characteristic asymmetry in the emission of the Λ-doublet lines. At longer wavelengths (>13 μm, depending on temperature), chemical pumping through the O + H_2 → OH(v, J) + H reaction contributes. Most of the JOYS sources show only these longer wavelength OH lines indicative of warm gas-phase chemistry (Francis et al. 2024; van Gelder et al. 2024a), although prompt emission is seen in a few JOYS sources (TMC1, BHR71-IRS1) besides HH 211. The implications of the presence or absence of 9–11 μm OH emission for the amount of UV and water remain to be quantified. Previously inferred values of the enhancement factor G_o compared with the interstellar radiation field are of order 10^2–10^3 on scales of ~1000 au using other tracers (Yıldız et al. 2015; Benz et al. 2016).

Other molecules: van Gelder et al. (2024a) report the first mid-infrared detection of NH_3 in a protostar, seen in absorption toward B1-c. The NH_3/H_2O column density ratio of 0.04 is again consistent with ice sublimation in a hot core. Other first detections toward a low-mass protostar include CS absorption (B1-c), and C_4H_2 and SiO emission (L1448-mm). The ^{13}C isotopologs of CO_2 and C_2H_2 are also seen for these two sources.

In summary, the relatively low temperatures of 100–200 K (somewhat higher in absorption) coupled with the lack of velocity shifts point toward a hot core origin for the bulk of the molecules. This is further strengthened by the similarity of gas and ice abundances relative to H_2O for molecules seen in ices: CO_2, CH_4 and NH_3, especially in the case of B1-c (see van Gelder et al. 2024a, and below). For L1448-mm and BHR71-IRS1, however, some molecules like H_2O are clearly associated with the outflow based on velocity offsets.

6.2. Molecular abundances: Hot core chemistry

The inferred molecular abundances can be used to test high temperature chemical models. The cleanest case for studying hot core chemistry is that of B1-c, for which the lines are in absorption and are therefore not affected by radiative pumping. Also, isotopologs are detected to correct for optical depth. For emission lines, determination of column densities and abundances is complicated by the fact that infrared radiative pumping needs to be properly accounted for: column densities can be too high by orders of magnitude if LTE excitation at the same low temperature that characterizes the rotational distribution is assumed for populating the vibrational levels (see case of SO_2 above).

Table 3 summarizes some key column density ratios of molecules. Determination of the fractional abundances with respect to H_2 is complicated by the fact that there is no clean tracer of the amount of 100–300 K molecular gas. Hence, warm H_2O is taken as a reference. Values are taken from Table H.4 of van Gelder et al. (2024a) and have a typical uncertainty of 30%. This can be higher if the optical depth of the lines is underestimated. Specifically, for CO_2 and C_2H_2, the column densities of $^{13}CO_2$ and $^{13}C_2H_2$ multiplied by 70 respectively 35 are used in Table 3. For CO_2 this value is a factor of three higher than that found from $^{12}CO_2$. The use of ratios implicitly assumes that the molecules are present in the same gas.

The chemistry in hot cores has been studied in a number of models over the past decades that start with the sublimation of ices at t = 0 above their sublimation temperature (typically

Table 3. Column density ratios of key molecules observed toward the low-mass protostar B1-c.

Species	Observed[a]	Model 150 K no X-rays	Model 150 K $L_X = 10^{29}$	Model 300 K no X-rays	Model 300 K $L_X = 10^{29}$	Model 600 K no X-rays	Model 600 K $L_X = 10^{29}$ erg s^{-1}
CO_2/H_2O	0.22	0.025	0.27	0.0016	0.0025	0.0012	0.0029
HCN/H_2O	0.08	0.024	0.0001	0.037	0.037	0.063	0.086
C_2H_2/H_2O	0.05	<0.0001	0.0003	<0.0001	0.0054	0.0001	0.0069
CH_4/H_2O	0.10	0.039	0.028	0.020	<0.0001	0.048	0.013
NH_3/H_2O	0.04	0.05	0.0001	0.062	0.016	0.10	0.069
C_2H_2/HCN	0.64	0.0001	3.4	0.0004	0.15	0.002	0.08
C_2H_2/CO_2	0.21	0.0001	0.001	0.008	2.2	0.10	240

Notes. [a] Observed column densities taken from Table H.4 of van Gelder et al. (2024a), using the warm H_2O column of 4.4×10^{18} cm^{-2} as reference. Observational uncertainties in the ratios are about 50%.

taken to be 100 K, representative of H_2O) and then follow the gas-phase chemistry for up to 10^5 yr (e.g., Charnley et al. 1992; Doty et al. 2004). It is well known that the abundances of some molecules are particularly sensitive to temperature, most notably HCN and C_2H_2 being significantly enhanced in warmer gas (Doty et al. 2002). In contrast, CO_2 production through CO + OH → CO_2 + H is halted at ~250 K when the OH + H_2 reaction takes over (see discussion in van Dishoeck et al. 2023). Another parameter that plays a role in setting the relative abundances is the X-ray luminosity. X-rays can both destroy molecules (e.g., water) and enhance molecules (e.g., C_2H_2) (Stäuber et al. 2005, 2007; Notsu et al. 2021).

Table 3 lists the results of the gas-grain chemistry model of Notsu et al. (2021) using the envelope structure of NGC 1333 IRAS2A derived by Kristensen et al. (2012) at r=60 au. This position is just inside the water snowline (~150 K) where the hot core starts and the density is 2×10^8 cm^{-3}. Such conditions are also representative of the B1-c envelope inside its snowline, even though it lies at somewhat smaller radii since B1-c is less luminous than IRAS2A. Values without X-rays and for $L_X = 10^{29}$ erg s^{-1} are tabulated. The model uses a detailed chemical network taken from Walsh et al. (2012, 2015).

The adopted X-ray luminosity of $L_X = 10^{29}$ erg s^{-1} is consistent with observations and chemical analyses of low-mass protostars (Benz et al. 2016) and turns out to be a "sweet spot" where the gas-phase CO_2 and C_2H_2 abundances are enhanced by one respectively two orders of magnitude at 150 K. Thus, this choice maximizes C_2H_2. H_2O and CH_4 are decreased by less than a factor of two for this value, but HCN and NH_3 are lower by more than two orders of magnitude, explaining the dramatic changes in the abundance ratios of, for example, C_2H_2/HCN in models with and without X-rays. For higher values of L_X, the abundances of all these six molecules decrease sharply. The use of H_2O as a reference introduces some uncertainties since its observed overall hot core abundance with respect to H_2 has been found to be less than the canonical value of 2×10^{-4} in models without X-rays (Persson et al. 2014, 2016). This observed low water abundance has, in fact, been one of the main motivations for introducing X-rays into the models (Stäuber et al. 2007; Notsu et al. 2021).

The overall conclusion of Table 3 is that hot core models of ice sublimation and gas-phase chemistry with modest X-rays reproduce the observed abundance ratios reasonably well within the model uncertainties of up to an order of magnitude. However, C_2H_2 is consistently underproduced by orders of magnitude at temperatures of only 150 K.

This underabundance of C_2H_2 has been noted before, also in the context of explaining its observed high abundances in high-mass protostars and even in deeply obscured (ultra)luminous infrared galaxies (Lahuis et al. 2007; Buiten et al. 2025). Temperature is clearly the one parameter that affects C_2H_2 most. Table 3 therefore also includes model abundances for temperatures of 300 and 600 K at the same density. These results show that the C_2H_2 abundance is indeed boosted at higher temperatures, especially in the presence of X-rays, although the observed high C_2H_2/H_2O ratios are not yet reached. We note that the observed rotational temperature of C_2H_2 in absorption toward B1-c is 285 ± 25 K, i.e., just consistent with the temperature regime at which C_2H_2 is significantly enhanced. HCN is increased as well with temperature, but not as strongly as C_2H_2. As expected, the CO_2 abundance is lower at $T > 300$ K, since OH is now driven into H_2O. Taken together, these results should be viewed as illustrative of the parameter regime that can explain the observed column density ratios. No single position model can explain all the column density ratios and the hydrocarbon chemistry remains to be fully understood. Explaining high C_2H_2 abundances derived from emission lines in hot core regions, where this molecule has a low rotational temperature of only ~150 K, would be a significant challenge if such temperatures were representative of the kinetic gas temperature. Source-specific depth-dependent models are needed to test whether the type of models presented here can reproduce both absolute and relative column densities. The models presented here do not consider any contribution from shocks. Sect. 6.3 discusses the detection of strong and warm C_2H_2 emission in at least one jet shock position that may have a different explanation.

6.3. NGC 1333 IRAS4B: Dense shock

Dense non-dissociative shocks can also emit copious molecular emission of molecules other than H_2 (Draine et al. 1983; Kaufman & Neufeld 1996). Indeed, extended warm H_2O emission has been imaged with *Herschel*-PACS in significant samples of low- and high-mass protostars showing both emission on and off source on scales of several thousand au (e.g., Nisini et al. 2010; Tafalla et al. 2013; Karska et al. 2013, 2018; van Dishoeck et al. 2021). We here investigate whether such molecular emission is seen in our data at any shocked positions off source. The HH 211 MRS map revealed bright OH prompt emission at the outer bow shock together with CO, H_2O and weak HCO^+ and CO_2 (see Fig. 7 of Caratti o Garatti et al. 2024), but no emission from other molecules. Also, in contrast with the extended H_2O

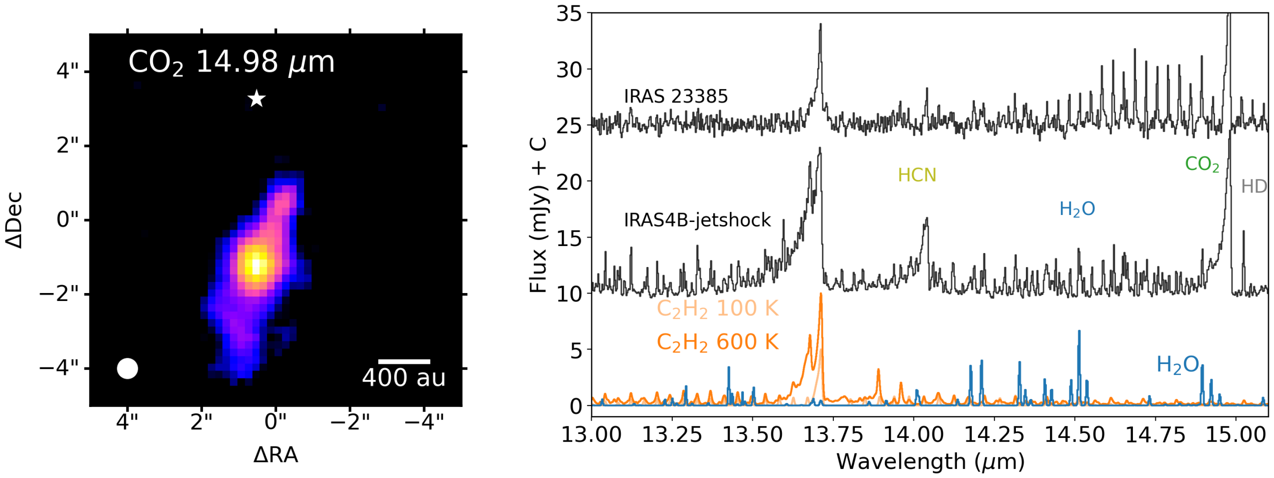

Fig. 20. Left: MRS image of the CO_2 15 μm band toward NGC 1333 IRAS4B showing the peak emission to be ~1000 au (~4″) offset from the source itself, whose position from millimeter interferometry is indicated by the white star. The beam size is indicated in the lower left corner. Right: MIRI-MRS spectrum of the NGC 1333 IRAS4B jet "knot" position in the 13–15 μm range highlighting its rich spectrum including hot C_2H_2 (600 K). For comparison, the spectrum of the high-mass protostar IRAS 23385, which shows only cold C_2H_2, is presented (Francis et al. 2024). The model spectra at the bottom show the contributions from C_2H_2 (100 and 600 K) and H_2O (280 K) in this wavelength range.

emission mapped by *Herschel*-PACS (Dionatos et al. 2018), no H_2O emission is found with MIRI at other HH 211 positions than the outer bow shock.

A special case within JOYS is formed by the Class 0 low-mass protostar NGC 1333 IRAS4B in Perseus (d=293 pc, L=4.4 $L_\odot$, Table 1). This source attracted attention by *Spitzer* since its mid-infrared IRS spectrum shows a very rich H_2O spectrum with an excitation temperature of ~170 K. It was speculated that these warm bright H_2O lines were due to a slow accretion shock liberating water at the envelope-disk interface in this young system (Watson et al. 2007). The subsequent longer wavelengths *Herschel*-PACS spectrum of this source taken with 9″ spaxels was found to be equally rich in H_2O and other far-infrared lines. However, the *Herschel* Nyquist-sampled spectral maps suggested the bulk of the emission to come from a position ~5″ south of the central source position as measured by millimeter interferometry, along the blue-shifted outflow lobe (Herczeg et al. 2012). The central source was concluded to be too heavily extincted even at these longer wavelengths. Rather than high-density ($\geq 10^{11}$ cm^{-3}) thermalized emission suggested by Watson et al. (2007), subthermal excitation of H_2O at $T_{\rm kin}$=1500 K and $n \sim 3 \times 10^6$ cm^{-3} was inferred by Herczeg et al. (2012).

The JWST MIRI-MRS spectral maps with their high spatial resolution can test these two scenarios. Figure 20 (left) shows an image in the CO_2 15 μm Q-branch. The emission of all molecules, including H_2O, as well as that of atoms is clearly seen to be extended along the blue outflow lobe with the brightest "knot" about 4″ offset from the central source position (see also Figures 13 and 14). No emission is detected at the central source position, nor in the red-shifted outflow lobe. This suggests that dense jet shocks are indeed responsible for the bright H_2O mid-infrared lines originally detected by *Spitzer* rather than an accretion shock onto the disk.

Figure 20 (right) presents the 13–15 μm MIRI-MRS spectrum extracted from the brightest knot position in a 1.4″ aperture. In contrast with most other jet and outflow positions in other JOYS Class 0 sources such as BHR 71 IRS1 (Fig. 16) or HH 211 (Caratti o Garatti et al. 2024), this knot shows very bright C_2H_2, HCN and CO_2 emission together with the mid-infrared H_2O lines. The C_2H_2 is also clearly much warmer, at least 600 K, compared with other low- and high-mass sources like IRAS 23385 (Fig. 20).

Although the spectrum can be well fitted with simple LTE slab models, the derivation of column densities and abundance ratios requires a detailed non-LTE excitation analysis since the density is well below the critical density of ~10^{12} cm^{-3} for ro-vibrational lines to be thermalized. Infrared pumping by radiation escaping through the outflow cavity can still contribute to the excitation of the ro-vibrational bands, even though the shock knot is significantly offset from the central source. The relatively high density of $>10^6$ cm^{-3}, likely higher than that of other jet knots, clearly helps in producing bright lines compared with other sources. The hot C_2H_2 emission points to high-temperature carbon-rich gas-phase chemistry taking place in this knot, perhaps enriched by the destruction or erosion of carbonaceous grains by processes such as sublimation (e.g., Li et al. 2021), pyrolysis or oxidation (e.g., Kress et al. 2010; Lee et al. 2010; Gail & Trieloff 2017) and reactions of carbon grains with atomic hydrogen, also called chemi-sputtering (e.g., Lenzuni et al. 1995). Recent protostar plus disk formation models by Borderies et al. (2025) show that this latter process is particularly effective at temperatures below 1000 K. Also, liberation of PAHs that were locked up in ices by sputtering may contribute. Taken together, this IRAS4B spectrum provides a unique opportunity to test physical-chemical models of high density shocks. A detailed analysis and comparison with the *Herschel* results will be presented in a future paper.

6.4. Chemistry in winds

The H_2 emission lines presented in Sect. 5 show evidence of wide-angle winds on scales of a few hundred au for low-mass protostars (see also Arulanantham et al. 2024; Salyk et al. 2024). The question addressed here is whether there is evidence of other molecules in these winds. In the edge-on case of the Tau 042021 Class II disk, H_2O and CO are found to be spatially extended with MIRI-MRS, but mostly along the disk surface and likely tracing scattered inner disk emission.

Figure 16 shows that CO_2 15 μm emission is extended along the outflow cavities for some sources, in contrast with C_2H_2

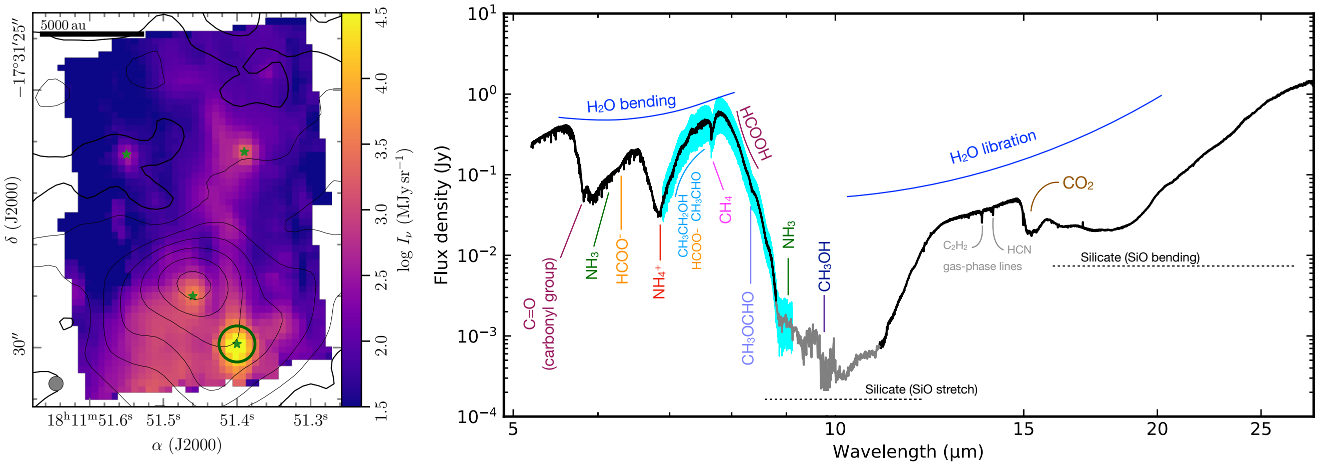

Fig. 21. Left: MIRI-MRS 5 μm continuum image of the IRAS 18089-1732. The four compact sources are marked by green stars. The 0.7″ aperture used to extract the MIRI-MRS spectrum of the brightest mid-infrared source is indicated by a green circle. A scale bar of 5000 au is shown in the top and the angular resolution at 5 μm is shown in the bottom-left corner. Black contours are the ALMA 3 mm continuum emission taken from Gieser et al. (2023a) with contour steps at 5, 10, 20, 40, 80, 160, 320×$\sigma_{\rm cont}$($\sigma_{\rm cont}$=0.057 mJy beam^{-1}). Right: MIRI-MRS spectrum of IRAS 18089-1732. The main absorption features are annotated in the figure. Gas-phase lines are not labeled, except in the case of C_2H_2 and HCN at 13.7 and 14.0 μm. The cyan region between 7 and 9 μm is the spectral window analyzed in this work. Because of the low S/N in the deep silicate absorption, the data between 8.9 and 10 μm are binned by a factor of five.

and HCN. Therefore, it is unlikely to be tracing scattered inner disk emission. Class I sources are good laboratories for studying disk winds since they are not overwhelmed by emission from hot cores or dense jet shocks. The Class I source TMC1, which shows a prominent H_2 wide-angle wind, has CO_2, OH and HCO^+ detected off source, but not H_2O (see Fig. 3 of Tychoniec et al. 2024). Taken together, it appears that primarily CO_2 is seen in emission off source, which, as mentioned in Sect. 6.1, could probe either sublimated ices or moderately warm gas chemistry in a wind. Sputtered ices along outflow cavity walls cannot be excluded, however. Since densities in winds are expected to be significantly below those required for thermalization, detailed non-LTE excitation models including infrared pumping are needed to quantify abundances. This is left to a future study. The other detected molecules, OH and HCO^+, point to a warm chemistry in which UV photons play a significant role, both in photodissociating H_2O and driving reactions of C^+ and O with excited H_2^*.

Winds can also be detected in absorption. Indeed, for the Class I source Oph IRS 46, both CO_2, C_2H_2 and HCN absorption have been seen with *Spitzer* and Keck (Lahuis et al. 2006) indicating an origin either in the upper layers of the inclined disk or in a wind/outflow. Within the JOYS sample, the Class I source TMC1A, known to have a disk wind (Bjerkeli et al. 2016; Harsono et al. 2023), shows both CO_2 and ro-vibrational H_2O lines in absorption (Fig. 15) but no HCN or C_2H_2, with the H_2O line having a clear velocity shift (van Gelder et al. 2024a). This makes it unlikely that the absorption arises in a hot core or inner disk. Quantification of column densities from absorption lines is much more robust than from emission lines; thus, TMC1A could serve as a test case for studying chemistry in winds.

In summary, the cases of TMC1 and TMC1A indicate that the chemistry in winds, showing CO_2, OH and HCO^+, is clearly different from the high temperature dense chemistry that produces abundant C_2H_2 and HCN (Sect. 6.2). Further development of, and quantitative comparison with, models of the chemistry in disk winds such as those of Panoglou et al. (2012); Yvart et al. (2016); Tabone et al. (2020) that include OH and HCO^+ are warranted.

7. Cold envelope: Ices

This section presents JOYS results on ices. As Figure 2 shows, ice features are prominently seen at 5–20 μm in MIRI-MRS spectra extracted from the bright mid-infrared continuum. Detected ices range from simple molecules like H_2O, CO_2 and CH_4 to CH_3OH as the most complex molecule identified pre-JWST (Boogert et al. 2015). Background information can be found in Sect. 2.3.4 and Appendix B.4.

7.1. Detection of complex molecules in ices

The high S/N JWST spectra allow weaker features to be identified, especially in the 5–10 μm range, where *Spitzer* only had R = 50–100. One of the early highlights of JOYS is the detection of complex molecules other than CH_3OH in ices toward the low-mass protostars NGC 1333 IRAS2A and B1-c and the high-mass source IRAS 23385+6053 (Rocha et al. 2024; Chen et al. 2024). These features occur in the range between 6.9–9.0 μm, also known as the icy COMs fingerprint region (Schutte et al. 1999; Öberg et al. 2011). To investigate how similar these COMs features are between low- and high-mass protostars, we analyze here a second high-mass protostar, IRAS 18089-1732.

Figure 21 presents the spectrum of IRAS 18089 extracted from the peak mid-infrared continuum in a 0.7″ aperture (RA=18h11m51.40s Dec=–17d31m29.93s). This aperture is optimized for the 7–9 μm region and is taken to be small, also at longer wavelengths, to avoid blending with another source. IRAS 18089 has a luminosity of ∼10^4 $L_\odot$ and envelope mass of ∼1000 $M_\odot$ based on single-dish observations (Sridharan et al. 2002; Beuther et al. 2002; Urquhart et al. 2018), at an estimated distance of 2.34 kpc (Xu et al. 2011). The source is known to be rich in gas-phase complex organic molecules (COMs) (e.g., Beuther et al. 2004; Isokoski et al. 2013).

Rocha et al. (2024) and Chen et al. (2024) found signatures of several icy COMs in their analyzed sources, including CH_3CHO (acetaldehyde), CH_3CH_2OH (ethanol), CH_3OCHO (methylformate), and CH_3OCH_3 (dimethylether). In addition, ice features of CH_4, HCOOH (formic acid), SO_2 and the negative ions OCN^-

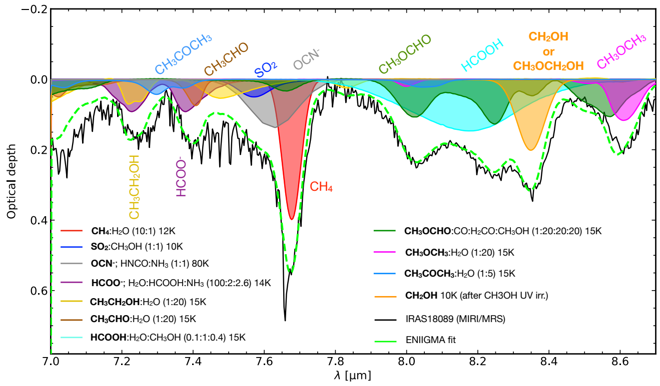

Fig. 22. Spectral fit between 7 and 8.7 μm of IRAS 18089 using the ENIIGMA fitting tool with laboratory ice mixtures from the LIDA database. Eleven ice components were used to obtain the best fit, which includes simple and complex molecules in ice mixtures. The boldface in the labels of the lab spectra indicates the main species that contributes in this spectral range. The narrow weak absorption features between 7 and 8 μm are primarily due to warm gas-phase H_2O; the narrow peak at 7.66 μm is due to gaseous CH_4 absorption.

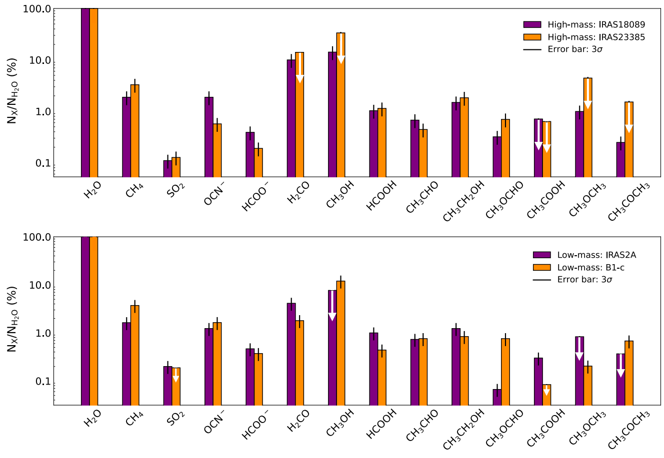

Fig. 23. Comparison of ice abundances relative to that of H_2O for the high-mass sources IRAS 18089 and IRAS 23385 (top) versus the low-mass protostars NGC 1333 IRAS2A and B1-c (bottom). White arrows indicate upper limits. The IRAS2A and IRAS 23385 results are taken from Rocha et al. (2024) and B1-c from Chen et al. (2024).

(cyanate ion) and $HCOO^-$ (formate ion) are found in the 7–9 μm range. Here, we adopt the same methodology as in Rocha et al. (2024) to execute the spectral fitting. The first step is to remove the continuum, the deep silicate feature and the H_2O 12 μm ice libration band, which is described in the Appendix F. This procedure also provides the total H_2O ice column density, which is found to be $(2.8 \pm 0.7) \times 10^{19}$ cm^{-2}.

The next step is to choose a local continuum for the 6.9–9.0 μm region on the optical depth spectrum that has been corrected for the global continuum, silicate feature and H_2O libration bands (see Fig. F.2). This local continuum takes into account absorption features from major species in this interval, such as the H_2O ice 6 μm bending mode, the prominent NH_4^+ 6.8 μm profile, and likely organic refractory material (Gibb et al. 2004). Figure F.3 in Appendix F shows this local continuum profile, which is obtained by fitting a fifth-order polynomial to guiding points to avoid unrealistic inflections. We note that a small but important excess is left around 7 μm since the CH_3 bending mode of several COMs contributes to this range.

After this local continuum subtraction, the spectrum is fitted using the infrared laboratory spectra of simple and complex molecules from the LIDA database, following Rocha et al. (2024) using the ENIIGMA fitting tool (Rocha et al. 2021). This code combines a large number of laboratory ice spectra in small groups of components aiming to find the best solution given by the χ^2. Starting from all possible species, a solution was found for IRAS 18089 that combines 11 ice mixtures, containing absorption features in the fitted wavelength range of CH_4, SO_2, OCN^-, $HCOO^-$, CH_3CH_2OH, CH_3CHO, CH_3OCHO, HCOOH, CH_3OCH_3 and CH_3COCH_3 (acetone), as shown in Figure 22.

Based on the statistical methods and criteria of Rocha et al. (2024) and as embedded in the ENIIGMA code, most of these identifications are thought to be secure; acetone is considered tentative for the case of IRAS 18089 (but see also discussion in Chen et al. 2024 for B1-c). The presence of H_2CO is based only on its 8 μm band and would need to be confirmed at shorter wavelengths. SO_2 ice is detected in this high-mass source, in contrast to the case of IRAS 23385 (Rocha et al. 2024). CH_3COOH (acetic acid) is not detected in either of the high-mass sources although its detection is sensitive to the local continuum placement at 7.8–8.0 μm.

Indeed, more generally, the detections and abundances of icy COMs remain sensitive to the details of the global and local continuum placement and subtraction. While the uncertainty in the global continuum reflects the source structure and SED, the local continuum must reflect the contribution of less understood species, such as salts and organic refractory materials that show broader infrared absorption features from 6 to 8 μm. Laboratory spectra are often available for only a limited range of ice mixtures and temperatures, although the current list already reflects huge experimental efforts focusing on those icy COMs that are also abundant in the gas-phase. Indeed, arguments in support of their identification include the detection of the same COMs at comparable abundances in the gas phase in the same source (see Chen et al. 2024; Nazari et al. 2024a, and below). New measurements to enlarge the icy COMs inventory in the laboratory exploring new ice mixtures in realistic abundances at a range of temperatures are encouraged, as well as more studies on the chemical composition of the organic refractory materials.

The IRAS 18089 spectrum contains a prominent 8.38 μm feature that has been seen in only a few other JWST ice spectra analyzed so far (B1-c, L1527, IRAS2A). Possible identifications include the hydroxymethyl radical (CH_2OH) or methoxymethanol (CH_3OCH_2OH). It will be discussed in a future paper that will also include new laboratory spectroscopy.

The derived ice column densities for the species fitted in this work are presented in Table F.1. CH_3OH is extracted from the bottom of the silicate feature for IRAS 18089, since no NIRSpec data are available for this source. The adopted band strengths are listed in Table 1 of Rocha et al. (2024). Uncertainties in inferred column densities are included in the table and are typically ~30%.

Figure 23 compares the ice columns relative to that of H_2O for the high-mass sources IRAS 18089 and IRAS 23385 versus the low-mass sources IRAS2A and B1-c. Very similar patterns are seen: not only are the same molecules detected in all four sources, but their abundances with respect to H_2O are also found to be comparable within the uncertainties for many species. Comparing high- and low-mass protostars, interestingly, methyl formate (CH_3OCHO) seems to show larger variations from source to source.

Chen et al. (2024) went one step further and compared the results for organic molecules in ices for the two low-mass protostars B1-c and NGC 1333 IRAS2A with those found in the gas phase in hot cores with ALMA toward the same sources. Interestingly, the ratios of some of the most abundant O-COMs with respect to methanol, CH_3OCHO/CH_3OH and CH_3OCH_3/CH_3OH, are very similar in ice and gas, supporting the picture of ice sublimation producing these species in their hot cores. However, the gaseous ratios of CH_3CHO/CH_3OH and C_2H_5OH/CH_3OH appear lower than those found in ices. Unless these COM ice abundances are overestimated, this suggests that some COMs may be destroyed quickly in the gas following sublimation (see discussion in Chen et al. 2024 and in Chen et al. 2025 for the case of acetone).

Besides quantification of ice column densities, comparisons between laboratory and observed infrared spectra also reveal information on ice temperatures and mixing conditions (i.e., mixing constituents and mixing ratios) of the detected COM ices, because these factors vary the peak position and the profile of their absorption bands. Rocha et al. (2024) and Chen et al. (2024) found that most of their detected COM ices are likely surrounded by a H_2O-rich environment, with CH_3OCHO as an outlier that is suggested to be present in a CO- and CH_3OH-rich layer. The inference on temperature is much more degenerate since many COM ice bands do not change much below their crystallization temperatures (usually ~100 K in the laboratory, 20%–40% lower in space due to lower pressures). Investigation of a larger sample is needed to solidify these results.

7.2. Ammonium salts in ices

The fit to the 7–9 μm range of the four sources for which the COMs have been analyzed (Fig. 23) also indicate the presence of two negative ions in the ices: $HCOO^-$ and OCN^- (see Fig. 22). The latter ion has been identified previously through its strong band at 4.62 μm seen along many lines of sight (e.g., Grim & Greenberg 1987; Novozamsky et al. 2001; van Broekhuizen et al. 2004), now also with JWST-NIRSpec (McClure et al. 2023; Nazari et al. 2024a). Together with the positive ion NH_4^+ that is ubiquitously detected at 6.85 μm (Figs. 2 and 21), they make up ammonium salts that are readily produced by acid-base reactions in ices (Knacke et al. 1982; Boogert et al. 2015, for review). Salts have recently gained renewed interest since they are found in high abundances in cometary material as one of the major nitrogen reservoirs (Altwegg et al. 2019) and also in the gas-phase in some high-mass protostars (Ginsburg et al. 2023).

The JWST JOYS analysis confirms the identification of the OCN^- ion through its bending mode at 7.6 μm and strengthens the assignment of the $HCOO^-$ ion as significant contributors to the 7.2 and 7.4 μm absorption bands, suggested by Schutte et al. (1999); Schutte & Khanna (2003). Moreover, they indicate the presence of ammonium hydrosulfide NH_4SH as the dominant ammonium salt in ices with SH^- the main counterpart of NH_4^+ and locking up 18–19% of the sulfur in dense clouds (Slavicinska et al. 2025a). Figure F.4 shows a fit to the 6.85 μm band of IRAS 18089. The ice anion abundances with respect to NH_4^+ are similar to those in comet 67P, where NH_4SH is also the dominant ammonium salt (Altwegg et al. 2022). Together, the identified icy N-species NH_4^+ and OCN^- make up 19% of the available N-budget (see Appendix F for details). NH_3 ice is difficult to measure in these data (Fig. 21), but, if its column were as high as 10% of H_2O ice (Boogert et al. 2015), it would increase the N–budget to 31%. Future studies using the larger JOYS+ sample and combining NIRSpec and MIRI will allow these ions to be studied across the Class 0 and I stages.

7.3. Limits on O_2 ice

The most abundant molecule detected in ices is H_2O, but it contains only a moderate fraction of the total oxygen budget, typically $\lesssim$20% (Whittet 2010; van Dishoeck et al. 2021). A significant fraction of oxygen must therefore be in other forms, and O_2 has been suggested as an option. Observations to date however indicate that it is not a major reservoir, neither in gas (Goldsmith et al. 2011; Liseau et al. 2012; Yıldız et al. 2013) nor in ice (Vandenbussche et al. 1999). Appendix B.4 provides more background information.

New impetus for searching for interstellar O_2 ice has come from the detection of abundant O_2 ice in comet 67P by the ROSINA instrument on board of the Rosetta mission (Bieler et al. 2015; Rubin et al. 2019). The cometary O_2 abundance is found to follow closely that of H_2O with heliocentric distance at a mean ratio of $O_2/H_2O\approx0.03$. While not a major oxygen reservoir, this still makes O_2 a significant ice component. Moreover, it provides insight into the major oxygen chemistry pathways: producing O_2 ice at this level through gas-grain chemistry requires special conditions (high density, low cosmic ray ionization rate) in the pre-stellar cloud to suppress water ice formation (Taquet et al. 2016).

Since O_2 is infrared inactive, it does not have a strong ice band in its pure ice form. However, if mixed with H_2O ice as suggested by the cometary results, its 6.45 μm band becomes weakly visible (Ehrenfreund et al. 1992; Müller et al. 2018). ISO-SWS was able to put only weak limits on the 6.45 μm feature in a few warm high-mass sources due to its low $S/N \approx 10$ on the continuum (Vandenbussche et al. 1999).

Here we used the deep MIRI spectrum of the most ice-rich source in the JOYS sample, the low-mass Class 0 source B1-c, to search for solid O_2. With an integration time of 1800 sec in channel 1C, this spectrum achieves a $S/N > 100$ on the continuum (Fig. 2). The data reduction details can be found in Chen et al. (2024). Figure 24 presents a blow up of the B1-c MIRI-MRS spectrum extracted at the source position in the 6–7 μm range. This region is dominated by the deep H_2O ice bending mode absorption at 6.0 μm with NH_3 ice at 6.18 μm, and the deep NH_4^+ band at 6.8 μm. Moreover, the B1-c spectrum is rich in narrow gas-phase absorption lines, most of them due to warm H_2O vapor that are superposed on the ice features (van Gelder et al. 2024a). A local continuum subtraction is performed between 6 and 6.6 μm, where any contribution of O_2 ice is expected (Fig. 24, top). Some anchor points are used in this fit to leave some space for known absorption features and ensure smooth curvature, and a fifth-order polynomial is then adopted to trace the continuum.

Subtracting all of these features and overlaying laboratory spectra of various O_2:H_2O mixtures provides a 3σ limit of O_2 (Fig. 24, bottom). The inferred value is $N_s(O_2) < 4.9\times10^{18}$ cm^{-2}, using a band strength $A = 3.9\times10^{-20}$ cm molecule^{-1} appropriate for 1:1 O_2 ice mixtures with H_2O (Müller et al. 2018). Together with $N_s(H_2O)=2.5\times10^{19}$ cm^{-2} (Chen et al. 2024), this provides an O_2 limit of ~20% relative to H_2O ice. Due to the strong dependence of the band strength on H_2O ice concentration, this value may be increased by a factor of five. We note that layered ice models indicate that O_2 is not uniformly mixed with H_2O ice (see Figure 5 in Taquet et al. 2016); hence, the use of an O_2:H_2O laboratory spectrum with a lower mixture than 1:30 could be justified. Nevertheless, it is clear that even with the sensitivity of JWST, it is not possible to put stringent limits on the O_2 ice abundance (Müller et al. 2018) and test values of order 3% as found in cometary ices.

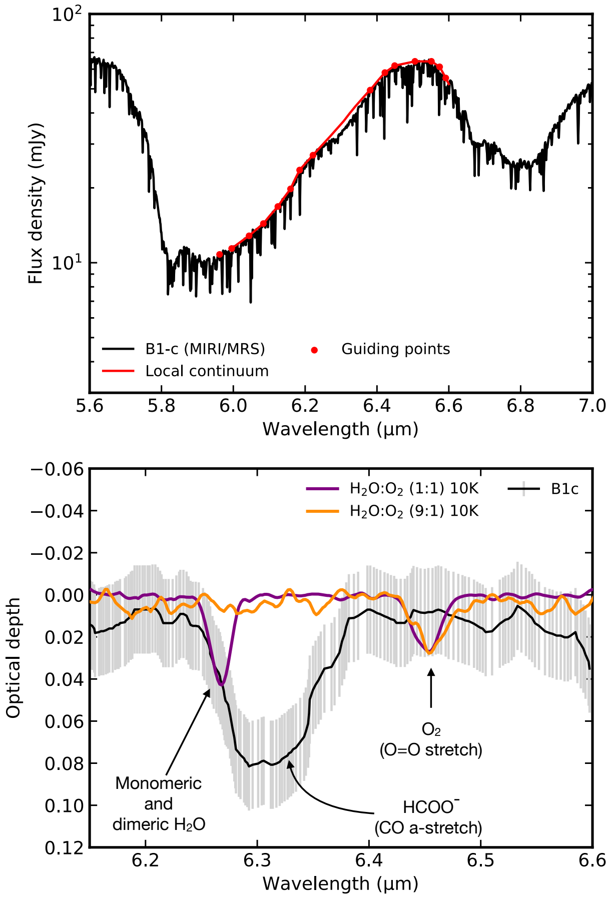

Fig. 24. Limits on O_2 ice in the spectrum of the low-mass protostar B1-c. The top panel shows the local continuum used between 6 and 6.6 μm together with the anchor points. The narrow absorption lines are all due to gas-phase water absorption (van Gelder et al. 2024a). The bottom panel presents the optical depth spectrum with 3σ error bars compared with O_2:H_2O ice laboratory spectra (Müller et al. 2018).

Future indirect constraints on the O_2 ice abundance may come from the analysis of the ^{13}CO ice profile at 4.8 μm and from searches for photoproducts of O_2 ice such as O_3 and CO_3 ice using both NIRSpec and MIRI data (Ehrenfreund & van Dishoeck 1998; Vandenbussche et al. 1999; Pontoppidan et al. 2003).

7.4. HDO/H_2O in protostellar ices

While there have been multiple determinations of the gaseous HDO/H_2O ratio in hot cores (Persson et al. 2014; Jensen et al. 2019), its value in interstellar ices remained poorly constrained prior to JWST (Dartois et al. 2003; Aikawa et al. 2012). JWST-NIRSpec offers the opportunity for deep searches for HDO ice through its O-D stretching mode at ~4.1 μm. Searches for this feature are complicated by the nearby weak CH_3OH 3.8–3.9 μm combination mode (Dartois et al. 2003), and a potential S-H stretch from molecules like H_2S or SH^- at 3.9 μm. On the other side of the HDO ice band, the deep $^{12}CO_2$ 4.3 μm ice absorption can distort the local continuum due to scattered light off ices, a process that is sensitive to grain shape effects (Dartois et al. 2022).

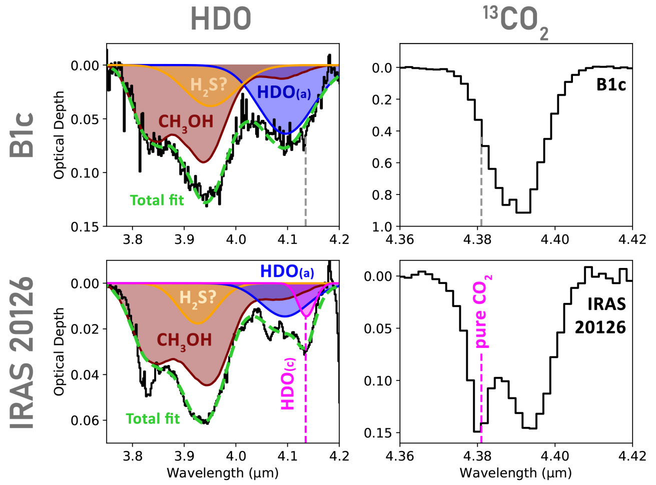

Fig. 25. Top-left panel: JWST NIRSpec spectrum of B1-c in the 3.8–4.2 μm range highlighting the detection of HDO ice. Laboratory spectra of HDO amorphous ice (HDO(a)) as well as of CH_3OH ice are overlaid. A Gaussian has been added to represent an S-H ice feature. Top-right panel: Ice band of $^{13}CO_2$ 4.38 μm of B1-c highlighting the lack of a heated ice component. Bottom-left panel: JWST NIRSpec spectrum of the high mass protostar IRAS 20126 taken from Slavicinska et al. (2024) showing the detection of both amorphous and crystalline HDO ice. The laboratory spectrum of crystalline HDO ice is shown in pink (HDO(c)). Bottom-right panel: Ice band of $^{13}CO_2$ 4.38 μm of IRAS 20126 showing evidence of a heated ice component as analyzed by Brunken et al. (2024a).

Slavicinska et al. (2024) recently presented the first robust detections of crystalline and amorphous HDO ice toward the intermediate- and high-mass protostars HOPS 370 (310 $L_\odot$) and IRAS 20126 (10^4 $L_\odot$) as part of the IPA sample. A careful decomposition of the 3.8–4.2 μm ice band was performed, using new laboratory data and obtaining a consistent fit with the CH_3OH 3.54 μm band to assess the contribution of CH_3OH ice at 3.8–3.9 μm. Both crystalline and amorphous HDO ice were required to fit the feature, consistent with the fact that both are warm sources as deduced also from the shape of their 3 μm H_2O ice bands showing crystalline H_2O ice and from the analysis of their $^{13}CO_2$ 4.38 μm ice bands (Brunken et al. 2024a). Both the HDO and $^{13}CO_2$ spectra for IRAS 20126 are included in Figure 25 (bottom). The inferred HDO/H_2O ice ratios range from (3–5) × 10^{-3}, comparable with the highest reported warm gaseous HDO/H_2O ratios in high-mass hot cores where ices have thermally sublimated.

The most prominent HDO ice detection to date is that toward the low mass Class 0 protostar L1527 using the G395M NIRSpec spectrum from program 1798 (PI: J. Tobin), which shows a significantly deeper deuterated water ice feature (Slavicinska et al. 2025b). This detection is particularly exciting, since this low-mass source provides a window into what the HDO/H_2O ice ratio in our own protosolar system could have been. The inferred value of 4.8 × 10^{-3} with an uncertainty of ~60% is at the upper end of the gaseous HDO/H_2O ratios in other isolated low-mass protostars (Jensen et al. 2019).

To explore whether the HDO/H_2O ice ratio toward L1527 is representative for solar-mass systems, we present here a second detection of HDO ice toward a low-mass protostar, B1-c. A NIRSpec G395M $R \sim 1000$ spectrum was taken as part of JOYS (program 1290). We note that all other NIRSpec spectra in JOYS+ used the G395H $R \sim 2700$ mode, which has a gap precisely at 4.1 μm and can therefore not be used for HDO searches. Within the JOYS+ data set, the low resolution PRISM mode could still be used for that purpose, albeit with less fidelity at R of only ~200. Such a PRISM study is left for a future paper.

Figure 25 (top) presents a blow-up of the 3.8–4.2 µm spectrum for B1-c over the same region as shown in Slavicinska et al. (2024); Slavicinska et al. (2025b) for the other sources. One complication for B1-c is that the blue side of the deep CO_2 ice feature shows clear signs of grain growth which affects the continuum determination. This wing has been removed using a local continuum in a similar manner as for L1527. Once removed, a clear HDO + CH_3OH feature emerges. Using the same fitting procedure as in Slavicinska et al. (2024); Slavicinska et al. (2025b), an HDO column of 1.2×10^{17} cm^{-2} is derived. The H_2O 3 µm band is completely saturated and below the noise in this source but an H_2O column density of 2.5×10^{19} cm^{-2} has been derived by Chen et al. (2024) from the H_2O libration mode (see also above section on O_2 ice limits for B1-c). Together this gives HDO/H_2O=$(4.8 \pm 3.0) \times 10^{-3}$, consistent with that found toward L1527. As for L1527, the uncertainties are dominated by the placement of the continuum and variations in band strength with temperature (see discussion in Slavicinska et al. 2025b).

Both values are close to that recently found in warm gas in a young protoplanetary disk where ice has sublimated (Tobin et al. 2023) (see Fig. 4 in Slavicinska et al. 2025b). They are somewhat higher than those measured in comets in our Solar system, suggesting that even though a large fraction of the water ice appears to be largely preserved in its journey from clouds to disks (Visser et al. 2009; Cleeves et al. 2014; van Dishoeck et al. 2021), some modifications may occur along the way to the comet and planetesimal formation sites (Furuya et al. 2017).

The HDO fit for B1-c requires only the presence of amorphous HDO ice. Since the H_2O 3 µm band profile cannot be observed in B1-c and the 12 µm band does not have a distinct crystalline feature, it is not possible to check whether there is any crystalline H_2O ice. However, the lack of crystalline HDO ice is consistent with the fact that the $^{13}CO_2$ ice band, included in Figure 25 (top), has only a single broad feature that can be fitted with cold CO_2:H_2O or CO_2:CH_3OH ice mixtures: no separate narrow blue-shifted peak due to heated pure CO_2 ice is needed as found for other sources (Brunken et al. 2024a). Similarly, the deep CO_2 15 µm bending mode of B1-c (Fig. 2) shows no hint of a double-peaked structure that is characteristic of heated ices. This suggests that, in contrast with the other sources, B1-c has not undergone episodes of intense accretion activity in the past that were strong enough to crystallize a significant portion of the ices: once crystallized, the process is irreversible.

8. Embedded disks

Disks are an integral part of protostellar systems, but little is still known about their composition in the embedded stage. A related question is to what extent these young disks are affected by accretion shocks of material falling onto the disk. Background information on this science case can be found in Sect. 2.3 and Appendix B.5.

8.1. Low-mass protostars

8.1.1. JWST spectra of sources with embedded disks

JWST MIRI-MRS data show rich spectra of Class II disks around pre-main sequence stars pointing to a diverse chemistry in their inner few au (see Appendix B.5). Some disks are very rich in H_2O (e.g., Gasman et al. 2023; Temmink et al. 2024a; Romero-Mirza et al. 2024; Banzatti et al. 2025), some are less H_2O rich (e.g., Perotti et al. 2023), whereas other disks show a prominent $^{(13)}CO_2$ feature (e.g., Grant et al. 2023; Vlasblom et al. 2025). Disks around very low mass stars often have strong emission from hydrocarbon molecules with only weak water lines (e.g., Tabone et al. 2023; Arabhavi et al. 2024, 2025; Kanwar et al. 2024). Excitation temperatures are high, from ~300 K up to 900 K. This diversity is thought to be linked to icy pebbles drifting from the outer to the inner disk, thereby enhancing molecules like H_2O and CO_2 when they cross their snowlines on timescales of 1–2 Myr. Dust traps locking up volatile elements in ices in the outer disks achieve the opposite effect of lowering their abundances (Kalyaan et al. 2023; Mah et al. 2023, 2024; Sellek et al. 2025).

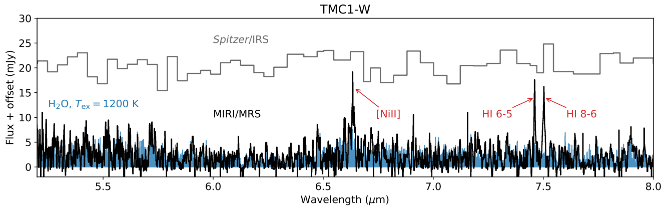

Fig. 26. JWST MIRI-MRS spectrum of the Class I TMC1-W source showing a forest of hot H_2O water lines. A LTE slab model at 1200 K is included for comparison in blue. The *Spitzer*-IRS spectrum of the binary TMC1 source is shown for comparison, illustrating that these types of detections were not possible prior to JWST. Figure adapted from van Gelder et al. (2024a), which shows the model spectrum offset from the data.

Since disks already form early in the Class 0 phase and are well established by the Class I phase (e.g., Ohashi et al. 2023; Tobin & Sheehan 2024), a prime question concerns the chemical composition of the inner regions of embedded young disks, at a time of <0.5 Myr when they are still pristine and not yet affected by radial drift of icy grains from the outer disk and/or when dust traps have not yet developed to interrupt the pebble flux.

Class I disks should have warm gas in their inner regions, just as Class II disks. Indeed, evidence of the presence of warm disk gas down to ~0.1 au is provided by VLT-CRIRES ^{12}CO υ=2–1 infrared line emission profiles at 4.6 µm (Herczeg et al. 2011). It therefore came as a surprise that the molecular line survey of the JOYS sources by van Gelder et al. (2024a) found primarily low excitation temperatures, not at all characteristic of inner disks (Sect. 6). Only one source with hot H_2O was uncovered, TMC1-W, which is part of the ~100 au separation binary source TMC1 with both sources showing evidence of a disk in millimeter continuum and line emission (Harsono et al. 2014; Tychoniec et al. 2021, 2024). Figure 26 presents the MIRI-MRS spectrum of the 5–8 µm range of this Class I protostar with the hot (~1200 K) water model overlaid. At first glance, the MIRI spectrum looks like pure noise, but blow-ups reveal that this is actually a forest of hot water lines (see also van Gelder et al. 2024a). Figure 26 includes the *Spitzer*-IRS spectrum for comparison to illustrate that such detections were not possible prior to JWST.

Figure 27 presents the 13.5–17.5 µm MIRI-MRS spectrum of one other Class I JOYS source, B1-a-NS. For comparison, the line-rich Class II disk DF Tau is shown, taken from Grant et al. (2024). This wavelength range contains several key molecules that are readily detected in Class II disks due to their $Q-$branches: CO_2, HCN and C_2H_2, in addition to the pure rotational lines of H_2O. It is clear that these Class I and II sources are very different, with B1-a showing only cold H_2O that is not even necessarily coming from the inner disk.

Figures 15 and 17 include the spectrum of our example source, the Class 0 protostar Serpens SMM3, which also shows evidence of a large embedded disk both in ALMA continuum

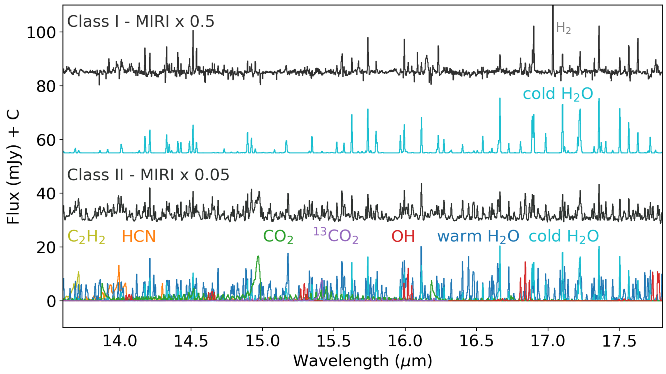

Fig. 27. Spectra from MIRI-MRS at 13.5–17.5 μm of the Class I source B1-a-NS showing only cold water (van Gelder et al. 2024a) and of the Class II disk DF Tau showing it being rich in warm H_2O and other molecules (Grant et al. 2024). The colored spectra show LTE slab models of individual molecules contributing to the observed spectra; they are meant to illustrate the positions of the lines, not as a fit to the data. The temperatures used on the H_2O slab models are 190 K (cold) and 490 K (warm).

and CO lines (Tychoniec et al. 2021) (Fig. 8). Like B1-a-NS, SMM3 shows no hints for warm molecular emission in the 13.5–17.5 μm range except for CO_2, nor at 22–26 μm for cold H_2O emission. The CO_2 emission appears extended along the outflow (Fig. 16) and may therefore not be arising from the inner disk. This example illustrates the importance of having spatial information at 30 au scales, as offered by MIRI-MRS.

8.1.2. Hiding warm molecular emission in young disks

We here discuss possible reasons for the absence of warm molecular disk emission in sources where a disk is clearly established. Figure 28 illustrates some differences between Class I and II disks. Some Class II disks also lack warm molecular emission, and in those cases the presence of a large inner cavity has been suggested (Banzatti et al. 2017; Vlasblom et al. 2024). Another related possibility is that dust traps in the outer disk have locked up water and other volatiles as ices, preventing the drifting icy pebbles from reaching the inner disk (e.g., Najita et al. 2013; Banzatti et al. 2020). However, the ALMA observations of a sample of representative Class 0 and I disks, including TMC1A, show little evidence of dust traps down to 5 au resolution (Ohashi et al. 2023). Also, even for Class II disks, gaps do not fully prevent oxygen and water from getting to the inner disk (e.g., Perotti et al. 2023; Schwarz et al. 2024; Gasman et al. 2025).

A more likely explanation is that the inner disk emission is hidden by small dust grains high up in the disk atmosphere, in any disk wind, and in the surrounding envelope. In Class II disks, the grains have grown and settled to the midplane, as evidenced by the fact that the analysis of their molecular emission generally invokes gas/(small) dust ratios of 10 000 rather than 100 in the line emitting region to explain the line strengths and line/continuum ratios (e.g., Meijerink et al. 2009; Bruderer et al. 2015; Woitke et al. 2018; Greenwood et al. 2019; Bosman et al. 2022). Figure 11 of Vlasblom et al. (2024) presents a series of thermochemical disk model spectra of H_2O and CO_2 in the 13–17 μm range for gas/dust ratios of 100, 1000 and 10 000 respectively, illustrating that the molecular emission is weakened by more than an order of magnitude at normal gas/dust ratios of 100. ALMA observations show clear evidence of highly settled large dust grains in the outer regions of Class II disks (e.g., Villenave et al. 2020), but much less in Class I disks (Villenave et al. 2023).

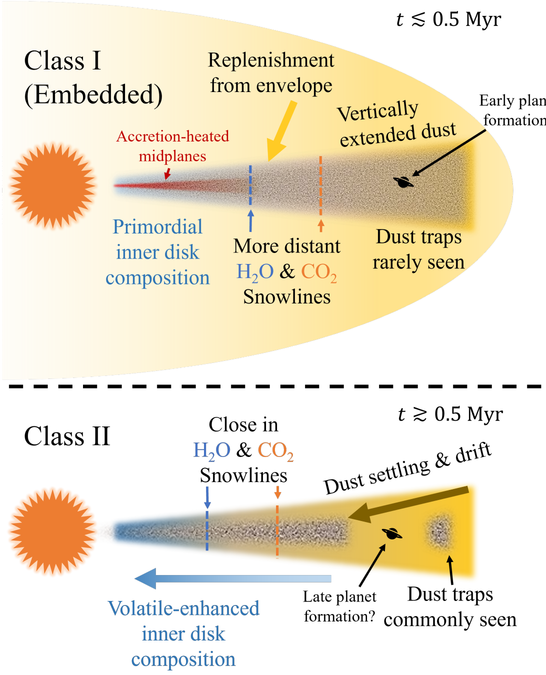

Fig. 28. Schematic illustrating differences in the physical and chemical structures of young Class I (∼0.5 Myr) (top) and more mature Class II (∼3 Myr) (bottom) disks.

Assuming ISM dust-to-gas ratios, the time taken for dust grains to grow large enough to settle is of the order of 1000 orbits at any given radius, which is ∼100 kyr for the outer disk. Drift thus likely begins sometime early on in the Class I phase. However, due to (i) the initial enrichment of the inner disk with dust from the outer disk, (ii) the timescale (100s of orbits) for the large grains to settle and drift, and (iii) the resupply of dust from the envelope, the dust-to-gas ratio can remain high up to ∼0.3–0.4 Myr (e.g., Cridland et al. 2022; Appelgren et al. 2023), i.e., for most of the Class I phase, likely even in the upper layers. Thus the levels of dust depletion needed to reproduce the line strengths in Class II disks are likely not achievable during the Class I phase even if drift is active to supply volatiles. Indeed, models of drifting icy grains find that inner disks are not only enhanced in H_2O but also in small dust that may mask the molecular features (Sellek et al. 2025; Houge et al. 2025).

While dust extinction could be an explanation for these MIRI observations, it remains puzzling that CO infrared disk emission, which should be similarly affected by dust extinction, is seen for several Class I sources (Herczeg et al. 2011), including TMC1A and TMC1 that are part of JOYS. This CO emission, particularly from the overtone bands, likely arises from the dust-free inner disk gas (Bosman et al. 2019; Banzatti et al. 2022), as has been found from spatially resolved near-infrared VLTI-Gravity observations of disks around more massive stars (e.g., GRAVITY Collaboration 2021). At least for the TMC1A disk, grain growth and likely dust settling has been inferred (Harsono et al. 2018).

Disk wind absorption superposed on disk emission is another option to minimize the molecular lines at the limited MIRI-MRS spectral resolution (Herczeg et al. 2011): high spectral resolution ($R \sim 100\,000$) VLT-CRIRES data reveal the presence of strong blue-shifted disk winds in absorption in

^{12}CO v =1–0 and ^{13}CO v=1–0 line profiles for many Class I sources. At MIRI-MRS spectral resolution, the emission and absorption may well cancel out (see also Banzatti et al. 2022). Such superposed absorption would be particularly important for bands that connect to the vibrational ground state. However it should not affect the highly excited pure rotational H_2O lines. Also, no C_2H_2 or HCN has yet been found associated with winds (see Sect. 6.4), except perhaps in the case of Oph IRS 46 (Lahuis et al. 2006). Further observations and analysis of a much larger sample of low-mass Class I disks, offered partially by JOYS+ and by approved Cycle 4 programs, is needed to determine whether the lack of warm molecular emission from embedded disks is found more commonly.

8.1.3. Evidence of accretion shocks?

A final question is whether the JWST data provide any indication of accretion shocks triggered by infall or streamers onto the disk. ALMA observations have suggested that sulfur-bearing molecules, most notably SO and SO_2, are good tracers of such shocks (Sakai et al. 2014; Artur de la Villarmois et al. 2019; Liu et al. 2025). JWST MIRI has detected SO_2 ro-vibrational emission at 7.3 μm for the first time on disk scales of a Class 0 source, but comparison with ALMA data suggests that a hot core rather than accretion shock origin is more likely. Also, SO_2 infrared emission is not commonly seen (van Gelder et al. 2024a). The use of [S I] 25 μm emission as an accretion shock tracer warrants further investigation, especially in Class I sources where it is not associated with the outflow, but is limited by the low spatial resolution in channel 4. Searching for local H_2 emission hot spots near the disk surface is another option.

8.2. High-mass protostars

Several high-mass protostars have been found to have Keplerian disks based on high-resolution ALMA data (see Appendix B.5), including IRAS 18089 (Beuther et al. 2007), although this has not yet been established for all high-mass sources included in JOYS. Due to their higher accretion rates and luminosities, the midplanes of disks around high-mass protostars can be heated to much higher temperatures than the upper disk layers resulting in a temperature gradient that is decreasing rather than increasing with height (D'Alessio et al. 1997; Harsono et al. 2015; Nazari et al. 2023). Barr et al. (2020) have proposed that the warm H_2O absorption at 7 μm seen at high spectral resolution data with SOFIA-EXES and ground-based instruments toward high-mass protostars actually arises in the accretion-heated inner midplane of disks. The warm H_2O absorption seen with MIRI-MRS toward IRAS 23385 (Francis et al. 2024) and IRAS 18089 (Figures 21 and 22) hints that this scenario could also hold for other high-mass protostars. Inspired by this scenario and using a radiative transfer model of Nazari et al. (2023) to characterize the temperature structure of an accreting massive disk, van Dishoeck et al. (2023) suggest that the cool CO_2 15 μm emission observed toward IRAS 23385 (Fig. 20) could arise from the colder surface layers of the outer disk around one or both of the protostars. Alternative hot core and outflow scenarios such as discussed in Sect. 6 cannot be excluded, however. Combined JWST, ALMA and high-resolution ground-based data are needed to disentangle the origin of the mid-infrared emission or absorption. Because of the high extinction, a pole-on geometry would be more favorable to peer into the inner disk-like structures. If a disk origin can be established, it would provide a unique probe of the physical and chemical structure of inner disks of high-mass protostars.

9. Conclusions

The exquisite sensitivity of JWST combined with the much higher spectral and spatial resolution offered by the MIRI-MRS IFU enable a new view of low- and high-mass protostars in their most deeply embedded stages. With this paper, we have presented a range of illustrative results on a sample of 23 low- and high-mass targets (32 if binaries are included) while addressing their physical and chemical evolution. A summary of published JOYS and JOYS+ studies to date is listed in Appendix B.6. Our main findings are as follows:

1. Mid-infrared H I recombination lines, in particular the H I 7–6 Humphreys α line at 12.37 μm, provide a powerful tool to measure accretion rates onto protostars in the earliest highly extincted stages. Inferred accretion rates for low-mass sources show a wide range of values, suggesting some sources are in a low-accretion quiescent stage. Analysis of one high-mass source indicates accretion rates that are high enough to form high-mass stars.
2. Jets commonly show a nested physical structure with an ionized core traced best by [Fe II] emission surrounded by a molecular layer traced by the higher-J H_2 pure rotational lines. This structure is seen across the entire protostellar mass range. For some low-mass sources, the molecular gas provides the main thrust in the earliest Class 0 stages, but this phase appears to be short-lived. By the Class I stage, the outflows become fully atomic and ionized. Our results emphasize the need of high spatial resolution data to determine mass loss rates.
3. Wide-angle winds traced by the lower-J pure-rotational H_2 lines are commonly found inside the outflow cavity walls, which can be outlined by scattered light and by entrained cold gas in CO millimeter lines. Their temperatures of a few hundred to 2000 K are lower than those of the jets, with gradients seen perpendicular to the jet axis. The main heating mechanisms of the gas may vary from position to position and warrant further investigation.
4. A large variety of atomic and ionic lines from refractory, semi-refractory, and volatile elements have been detected and imaged in most sources. Their different morphologies are related to different levels of elemental depletions, local shock conditions, and (in the case of noble gases) photoionization. Also, 20 μm continuum emission due to heated dust has been found in a few very young Class 0 sources. Together with the atomic lines, this allows dust launching in jets and grain destruction in shocks to be quantified.
5. Hot core and dense shock chemistry models can be tested with unprecedented detail through observations of simple key molecules such as H_2O, CO_2, HCN, C_2H_2, OH, and SO_2 in both low- and high-mass sources. Derivation of their abundances requires use of non-LTE excitation models including infrared pumping. Ice sublimation followed by high-temperature gas phase chemistry, perhaps stimulated by X-rays, explains the data for some sources, whereas dense jet shocks are more appropriate for others. No clear indication for accretion shocks onto low-mass disks has yet been found. The case of NGC 1333 IRAS4B provides a unique data set to test dense shock chemistry models, including the chemical processes that lead to bright hot C_2H_2 emission.
6. Ice studies have made a significant jump forward thanks to the high-quality MIRI-MRS data in the 5–10 μm range. Several complex organic molecules and ions (salts) have been found with comparable abundances in low- and high-mass protostars. We report the second detection of HDO ice in

a low-mass protostar, with HDO/H_2O ice ratios that point to inheritance from cloud to disk. Though O_2 ice remains elusive, JWST provides improved limits.

7. Young disks in the embedded stage do not show the same forest of warm molecular lines as more evolved Class II disks do. A likely explanation is that small dust has not yet grown and settled and is being replenished by radial drift, thereby obscuring a clear view to their inner few au. Extinction from dust in a disk wind or envelope may also contribute to this.

This paper provides a first comprehensive look into JWST MIRI-MRS studies of a significant sample of protostars. So far, many similarities between low- and high-mass sources have been found. Larger samples across evolutionary stages and stellar mass ranges, such as offered by JOYS+ and by other currently ongoing and future programs such as the High angular-resolution observations of Emergence in Filamentary Environments (HEFE; P.I. T. Megeath), will allow much more robust trends to be identified. In particular, the low-mass sample in JOYS contains only four (six with binaries) Class I sources and will be more than doubled in JOYS+. HEFE will add many more Class 0 sources of intermediate luminosity in a highly UV irradiated environment. Such large samples will also help in interpreting similar spectra seen in extragalactic sources.

More robust calibrations of mass loss and mass accretion rates need to be developed and quantified. Studies of binaries and/or clustering will be possible at 0.5–5″ separation with the JOYS+ sample. The combined NIRSpec + MIRI study will increase the available diagnostics, which includes providing higher excitation [Fe II] and H_2 lines that probe hotter gas. The results from such studies ultimately need to be made consistent with the physical components of warm and hot gas found in CO and H_2O data with *Herschel*. The high spatial and spectral resolution of NIRSpec also allows key ices to be detected and ice mapping against the scattered light continuum to be conducted. The NIRCam imaging and spectral mapping can do so as well. When combined with ALMA and other instruments, JWST will truly help lift the veil of key components of the youngest stages of stellar and planetary birth.

Acknowledgements. The authors thank the referee for their constructive comments and the entire JOYS+ team, Adwin Boogert, John Black, Brunella Nisini, Teresa Giannini, and Christoffel Waelkens for useful discussions. Collaboration with Catherine Walsh on hot core chemical models is much appreciated. This work is based on observations made with the NASA/ESA/CSA James Webb Space Telescope. The data were obtained from the Mikulski Archive for Space Telescopes at the Space Telescope Science Institute, which is operated by the Association of Universities for Research in Astronomy, Inc., under NASA contract NAS 5-03127 for JWST. These observations are associated with programs 1290 and 1257. The following National and International Funding Agencies funded and supported the MIRI development: NASA; ESA; Belgian Science Policy Office (BELSPO); Centre Nationale d'Études Spatiales (CNES); Danish National Space Centre; Deutsches Zentrum fur Luft und Raumfahrt (DLR); Enterprise Ireland; Ministerio De Economiá y Competividad; The Netherlands Research School for Astronomy (NOVA); The Netherlands Organisation for Scientific Research (NWO); Science and Technology Facilities Council; Swiss Space Office; Swedish National Space Agency; and UK Space Agency. Astrochemistry in Leiden is supported by funding from the European Research Council (ERC) under the European Union's Horizon 2020 research and innovation program (grant agreement No. 291141 MOLDISK), and by NOVA and NWO through TOP-1 grant 614.001.751 and its Dutch Astrochemistry Program (DANII). The present work is closely connected to ongoing research within InterCat, the Center for Interstellar Catalysis located in Aarhus, Denmark. TR acknowledges support from ERC grant no. 743029 EASY and TH from ERC grant no. 832428 Origins. ACG acknowledges support from PRIN-MUR 2022 20228JPA3A "The path to star and planet formation in the JWST era (PATH)" funded by NextGeneration EU and by INAF-GoG 2022 "NIR-dark Accretion Outbursts in Massive Young stellar objects (NAOMY)" and Large Grant INAF 2022 "YSOs Outflows, Disks and Accretion: toward a global framework for the evolution of planet forming systems (YODA)". KJ and GÖ acknowledge support from the Swedish National Space Agency (SNSA), and LC from grant PIB2021-127718NB-100 from the Spanish Ministry of Science and Innovation/State Agency of Research MCIN/AEI/10.13039/50110001103. PJK acknowledges financial support from the Research Ireland Pathway programme under Grant Number 21/PATH-S/9360. VJML's research is supported by an appointment to the NASA Postdoctoral Program at the NASA Ames Research Center, administered by Oak Ridge Associated Universities under contract with NASA. PN acknowledges support from the ESO Fellowship and IAU Gruber Foundation Fellowship programs. SN is grateful for support from Grants-in-Aid for JSPS (Japan Society for the Promotion of Science) Fellows Grant Number JP23KJ0329, MEXT/JSPS Grants-in-Aid for Scientific Research (KAKENHI) Grant Numbers JP23K13155 and JP24K00674, and Start-up Research Grant as one of the University of Tokyo Excellent Young Researcher 2024. GP gratefully acknowledges support from the Max Planck Society and from the Carlsberg Foundation, grant CF23-0481. This paper makes use of the following ALMA data: ADS/JAO.ALMA#ALMA 2015.1.00354.S, ADS/JAO.ALMA#ALMA 2017.1.01350.S, ADS/JAO.ALMA#ALMA 2019.1.00931.S. ALMA is a partnership of ESO (representing its member states), NSF (USA) and NINS (Japan), together with NRC (Canada), NSTC and ASIAA (Taiwan), and KASI (Republic of Korea), in cooperation with the Republic of Chile. The Joint ALMA Observatory is operated by ESO, AUI/NRAO and NAOJ.

References

Aikawa, Y., Kamuro, D., Sakon, I., et al. 2012, A&A, 538, A57
Aikawa, Y., Okuzumi, S., & Pontoppidan, K. 2024, in Comets III, eds. K. J. Meech, M. R. Combi, D. Bockelée-Morvan, S. N. Raymodn, & M. E. Zolensky, 33
Altwegg, K., Balsiger, H., & Fuselier, S. A. 2019, ARA&A, 57, 113
Altwegg, K., Combi, M., Fuselier, S. A., et al. 2022, MNRAS, 516, 3900
Anderson, D. E., Bergin, E. A., Maret, S., & Wakelam, V. 2013, ApJ, 779, 141
André, P., Ward-Thompson, D., & Barsony, M. 2000, in Protostars and Planets IV, eds. V. Mannings, A. P. Boss, & S. S. Russell (Tucson: University of Arizona), 59
Anglada, G., Rodríguez, L. F., & Carrasco-González, C. 2018, A&A Rev., 26, 3
Appelgren, J., Lambrechts, M., & van der Marel, N. 2023, A&A, 673, A139
Arabhavi, A. M., Kamp, I., Henning, T., et al. 2024, Science, 384, 1086
Arabhavi, A. M., Kamp, I., van Dishoeck, E. F., et al. 2025, ApJ, 984, L62
Arce, H. G., Shepherd, D., Gueth, F., et al. 2007, Protostars and Planets V, 245
Argyriou, I., Glasse, A., Law, D. R., et al. 2023, A&A, 675, A111
Artur de la Villarmois, E., Jørgensen, J. K., Kristensen, L. E., et al. 2019, A&A, 626, A71
Artur de la Villarmois, E., Guzmán, V. V., Jørgensen, J. K., et al. 2022, A&A, 667, A20
Arulanantham, N., McClure, M. K., Pontoppidan, K., et al. 2024, ApJ, 965, L13
Arulanantham, N., Salyk, C., Pontoppidan, K., et al. 2025, arXiv e-prints, [arXiv:2505.07562]
Assani, K. D., Li, Z.-Y., Ramsey, J. P., et al. 2025, A&A, submitted [arXiv:2504.02136]
Bacciotti, F., Nony, T., Podio, L., et al. 2025, A&A, submitted [arXiv:2501.03920]
Bachiller, R., & Tafalla, M. 1999, in NATO ASIC Proc. 540: The Origin of Stars and Planetary Systems, eds. C. J. Lada, & N. D. Kylafis, 227
Baek, G., MacFarlane, B. A., Lee, J.-E., et al. 2020, ApJ, 895, 27
Balança, C., Spielfiedel, A., & Feautrier, N. 2016, MNRAS, 460, 3766
Bally, J. 2016, ARA&A, 54, 491
Banzatti, A., & Pontoppidan, K. M. 2015, ApJ, 809, 167
Banzatti, A., Pontoppidan, K. M., Salyk, C., et al. 2017, ApJ, 834, 152
Banzatti, A., Pascucci, I., Bosman, A. D., et al. 2020, ApJ, 903, 124
Banzatti, A., Abernathy, K. M., Brittain, S., et al. 2022, AJ, 163, 174
Banzatti, A., Pontoppidan, K. M., Pére Chávez, J., et al. 2023, AJ, 165, 72
Banzatti, A., Salyk, C., Pontoppidan, K. M., et al. 2025, AJ, 169, 165
Barr, A. G., Boogert, A., DeWitt, C. N., et al. 2018, ApJ, 868, L2
Barr, A. G., Boogert, A., DeWitt, C. N., et al. 2020, ApJ, 900, 104
Barr, A. G., Boogert, A., Li, J., et al. 2022, ApJ, 935, 165
Barsony, M., Ressler, M. E., Le Gouellec, V. J. M., Tychoniec, Ł., & van Gelder, M. L. 2024, ApJ, 973, 42
Beltrán, M. T., & de Wit, W. J. 2016, A&A Rev., 24, 6
Benz, A. O., Bruderer, S., van Dishoeck, E. F., et al. 2016, A&A, 590, A105
Bergin, E. A., Melnick, G. J., Stauffer, J. R., et al. 2000, ApJ, 539, L129
Bergin, E. A., Melnick, G. J., Gerakines, P. A., Neufeld, D. A., & Whittet, D. C. B. 2005, ApJ, 627, L33
Bergin, E. A., Bosman, A., Teague, R., et al. 2024, ApJ, 965, 147
Bertoldi, F., Timmermann, R., Rosenthal, D., Drapatz, S., & Wright, C. M. 1999, A&A, 346, 267
Beuther, H., Hunter, T. R., Zhang, Q., et al. 2004, ApJ, 616, L23

Beuther, H., Schilke, P., Sridharan, T. K., et al. 2002, A&A, 383, 892

Beuther, H., Sridharan, T. K., & Saito, M. 2005, ApJ, 634, L185

Beuther, H., Zhang, Q., Bergin, E. A., et al. 2007, A&A, 468, 1045

Beuther, H., van Dishoeck, E. F., Tychoniec, L., et al. 2023, A&A, 673, A121

Beuther, H., Kuiper, R., & Tafalla, M. 2025, arXiv e-prints, [arXiv:`2501.16866`]

Bieler, A., Altwegg, K., Balsiger, H., et al. 2015, Nature, 526, 678

Bik, A., & Thi, W. F. 2004, A&A, 427, L13

Bjerkeli, P., van der Wiel, M. H. D., Harsono, D., Ramsey, J. P., & Jørgensen, J. K. 2016, Nature, 540, 406

Blake, G. A., & Boogert, A. C. A. 2004, ApJ, 606, L73

Blake, G. A., Anicich, V. G., & Huntress, Jr., W. T. 1986, ApJ, 300, 415

Böker, T., Beck, T. L., Birkmann, S. M., et al. 2023, PASP, 135, 038001

Bonito, R., Orlando, S., Peres, G., et al. 2010, A&A, 511, A42

Bontemps, S., Andre, P., Terebey, S., & Cabrit, S. 1996, A&A, 311, 858

Boogert, A. C. A., Helmich, F. P., van Dishoeck, E. F., et al. 1998, A&A, 336, 352

Boogert, A. C. A., Ehrenfreund, P., Gerakines, P. A., et al. 2000, A&A, 353, 349

Boogert, A. C. A., Pontoppidan, K. M., Lahuis, F., et al. 2004, ApJS, 154, 359

Boogert, A. C. A., Pontoppidan, K. M., Knez, C., et al. 2008, ApJ, 678, 985

Boogert, A. C. A., Chiar, J. E., Knez, C., et al. 2013, ApJ, 777, 73

Boogert, A. C. A., Gerakines, P. A., & Whittet, D. C. B. 2015, ARA&A, 53, 541

Boonman, A. M. S., Stark, R., van der Tak, F. F. S., et al. 2001, ApJ, 553, L63

Boonman, A. M. S., Doty, S. D., van Dishoeck, E. F., et al. 2003a, A&A, 406, 937

Boonman, A. M. S., van Dishoeck, E. F., Lahuis, F., & Doty, S. D. 2003b, A&A, 399, 1063

Boonman, A. M. S., van Dishoeck, E. F., Lahuis, F., et al. 2003c, A&A, 399, 1047

Borderies, A., Commerçon, B., & Bourdon, B. 2025, A&A, 694, A89

Bosman, A. D., Bruderer, S., & van Dishoeck, E. F. 2017, A&A, 601, A36

Bosman, A. D., Banzatti, A., Bruderer, S., et al. 2019, A&A, 631, A133

Bosman, A. D., Bergin, E. A., Calahan, J., & Duval, S. E. 2022, ApJ, 930, L26

Bouchet, P., García-Marín, M., Lagage, P. O., et al. 2015, PASP, 127, 612

Boudin, N., Schutte, W. A., & Greenberg, J. M. 1998, A&A, 331, 749

Brown, J. M., Pontoppidan, K. M., van Dishoeck, E. F., et al. 2013, ApJ, 770, 94

Bruderer, S., Benz, A. O., Doty, S. D., van Dishoeck, E. F., & Bourke, T. L. 2009, ApJ, 700, 872

Bruderer, S., Harsono, D., & van Dishoeck, E. F. 2015, A&A, 575, A94

Brunken, N. G. C., Rocha, W. R. M., van Dishoeck, E. F., et al. 2024a, A&A, 685, A27

Brunken, N. G. C., van Dishoeck, E. F., Slavicinska, K., et al. 2024b, A&A, 692, A163

Buiten, V. A., van der Werf, P. P., Viti, S., et al. 2025, A&A, 699, A312

Bushouse, H., Eisenhamer, J., Dencheva, N., et al. 2024, `https://doi.org/10.5281/zenodo.15632984`

Cacciapuoti, L., Macias, E., Gupta, A., et al. 2024, A&A, 682, A61

Cami, J., Yamamura, I., de Jong, T., et al. 2000, A&A, 360, 562

Caratti o Garatti, A., Stecklum, B., Linz, H., Garcia Lopez, R., & Sanna, A. 2015, A&A, 573, A82

Caratti o Garatti, A., Ray, T. P., Kavanagh, P. J., et al. 2024, A&A, 691, A134

Cardelli, J. A., Clayton, G. C., & Mathis, J. S. 1989, ApJ, 345, 245

Carr, J. S. 1989, ApJ, 345, 522

Carr, J. S., & Najita, J. R. 2008, Science, 319, 1504

Carr, J. S., & Najita, J. R. 2011, ApJ, 733, 102

Carr, J. S., & Najita, J. R. 2014, ApJ, 788, 66

Caselli, P., Keto, E., Bergin, E. A., et al. 2012, ApJ, 759, L37

Ceccarelli, C., Codella, C., Balucani, N., et al. 2023, in Astronomical Society of the Pacific Conference Series, 534, Protostars and Planets VII, eds. S. Inutsuka, Y. Aikawa, T. Muto, K. Tomida, & M. Tamura, 379

Cernicharo, J., Noriega-Crespo, A., Cesarsky, D., et al. 2000, Science, 288, 649

Cesaroni, R., Neri, R., Olmi, L., et al. 2005, A&A, 434, 1039

Cesaroni, R., Beuther, H., Ahmadi, A., et al. 2019, A&A, 627, A68

Cesaroni, R., Galli, D., Padovani, M., Rivilla, V. M., & Sánchez-Monge, Á. 2025, A&A, 693, A76

Charnley, S. B., Tielens, A. G. G. M., & Millar, T. J. 1992, ApJ, 399, L71

Chen, Y., Rocha, W. R. M., van Dishoeck, E. F., et al. 2024, A&A, 690, A205

Chen, Y., Garrod, R. T., Rachid, M., et al. 2025, A&A, 696, A198

Christiaens, V., Gonzalez, C., Farkas, R., et al. 2023, J. Open Source Softw., 8, 4774

Cleeves, L. I., Bergin, E. A., Alexander, C. M. O. D., et al. 2014, Science, 345, 1590

Colmenares, M. J., Bergin, E. A., Salyk, C., et al. 2024, ApJ, 977, 173

Connelley, M. S., & Reipurth, B. 2018, ApJ, 861, 145

Cridland, A. J., Rosotti, G. P., Tabone, B., et al. 2022, A&A, 662, A90

Crouzet, N., Mueller, M., Sargent, B., et al. 2025, A&A, 698, A77

Cyganowski, C. J., Whitney, B. A., Holden, E., et al. 2008, AJ, 136, 2391

D'Alessio, P., Calvet, N., & Hartmann, L. 1997, ApJ, 474, 397

Dartois, E., D'Hendecourt, L., Boulanger, F., et al. 1998, A&A, 331, 651

Dartois, E., Thi, W., Geballe, T. R., et al. 2003, A&A, 399, 1009

Dartois, E., Noble, J. A., Ysard, N., Demyk, K., & Chabot, M. 2022, A&A, 666, A153

Delabrosse, V., Dougados, C., Cabrit, S., et al. 2024, A&A, 688, A173

Dionatos, O., & Güdel, M. 2017, A&A, 597, A64

Dionatos, O., Nisini, B., Garcia Lopez, R., et al. 2009, ApJ, 692, 1

Dionatos, O., Ray, T., & Güdel, M. 2018, A&A, 616, A84

Dionatos, O., Kristensen, L. E., Tafalla, M., Güdel, M., & Persson, M. 2020, A&A, 641, A36

Dominik, C., Min, M., & Tazaki, R. 2021, OpTool: Command-line driven tool for creating complex dust opacities, Astrophysics Source Code Library [`record ascl:2104.010`]

Dorschner, J., Begemann, B., Henning, T., Jaeger, C., & Mutschke, H. 1995, A&A, 300, 503

Doty, S. D., van Dishoeck, E. F., van der Tak, F. F. S., & Boonman, A. M. S. 2002, A&A, 389, 446

Doty, S. D., Schöier, F. L., & van Dishoeck, E. F. 2004, A&A, 418, 1021

Draine, B. T. 2006, in Astronomical Society of the Pacific Conference Series, 348, Astrophysics in the Far Ultraviolet: Five Years of Discovery with FUSE, eds. G. Sonneborn, H. W. Moos, & B. G. Andersson, 58

Draine, B. T., & Hensley, B. S. 2021, ApJ, 909, 94

Draine, B. T., Roberge, W. G., & Dalgarno, A. 1983, ApJ, 264, 485

Dullemond, C. P., Henning, T., Visser, R., et al. 2007, A&A, 473, 457

Dungee, R., Boogert, A., DeWitt, C. N., et al. 2018, ApJ, 868, L10

Dunham, M. M., Stutz, A. M., Allen, L. E., et al. 2014, in Protostars and Planets VI, eds. H. Beuther, R. S. Klessen, C. P. Dullemond, & T. Henning, 195

Ehrenfreund, P., & van Dishoeck, E. F. 1998, Adv. Space Res., 21, 15

Ehrenfreund, P., Breukers, R., D'Hendecourt, L., & Greenberg, J. M. 1992, A&A, 260, 431

Ehrenfreund, P., Boogert, A. C. A., Gerakines, P. A., et al. 1996, A&A, 315, L341

Ehrenfreund, P., Dartois, E., Demyk, K., & D'Hendecourt, L. 1998, A&A, 339, L17

Ehrenfreund, P., Kerkhof, O., Schutte, W. A., et al. 1999, A&A, 350, 240

Ellerbroek, L. E., Podio, L., Dougados, C., et al. 2014, A&A, 563, A87

Enoch, M. L., Evans, II, N. J., Sargent, A. I., & Glenn, J. 2009, ApJ, 692, 973

Ercolano, B., & Pascucci, I. 2017, Roy. Soc. Open Sci., 4, 170114

Espaillat, C., Ingleby, L., Furlan, E., et al. 2013, ApJ, 762, 62

Evans, II, N. J., Lacy, J. H., & Carr, J. S. 1991, ApJ, 383, 674

Evans, N. J., Dunham, M. M., Jørgensen, J. K., et al. 2009, ApJS, 181, 321

Fallscheer, C., Beuther, H., Sauter, J., Wolf, S., & Zhang, Q. 2011, ApJ, 729, 66

Federman, S. A., Megeath, S. T., Rubinstein, A. E., et al. 2024, ApJ, 966, 41

Fedriani, R., Caratti o Garatti, A., Cesaroni, R., et al. 2023, A&A, 676, A107

Ferreira, J., Dougados, C., & Cabrit, S. 2006, A&A, 453, 785

Fiorellino, E., Tychoniec, Ł., Cruz-Sáenz de Miera, F., et al. 2023, ApJ, 944, 135

Fischer, W. J., Megeath, S. T., Furlan, E., et al. 2017, ApJ, 840, 69

Fischer, W. J., Hillenbrand, L. A., Herczeg, G. J., et al. 2023, in Astronomical Society of the Pacific Conference Series, 534, Protostars and Planets VII, eds. S. Inutsuka, Y. Aikawa, T. Muto, K. Tomida, & M. Tamura, 355

Flower, D. R., & Pineau Des Forêts, G. 2010, MNRAS, 406, 1745

Franceschi, R., Henning, T., Tabone, B., et al. 2024, A&A, 687, A96

Francis, L., Johnstone, D., Lee, J.-E., et al. 2022, ApJ, 937, 29

Francis, L., van Gelder, M. L., van Dishoeck, E. F., et al. 2024, A&A, 683, A249

Francis, L., van Dishoeck, E. F., Caratti o Garatti, A., et al. 2025, A&A, 694, A174

Frank, A., Ray, T. P., Cabrit, S., et al. 2014, in Protostars and Planets VI, eds. H. Beuther, R. S. Klessen, C. P. Dullemond, & T. Henning, 451

Furlan, E., McClure, M., Calvet, N., et al. 2008, ApJS, 176, 184

Furuya, K., Drozdovskaya, M. N., Visser, R., et al. 2017, A&A, 599, A40

Gail, H.-P., & Trieloff, M. 2017, A&A, 606, A16

Gardner, J. P., Mather, J. C., Abbott, R., et al. 2023, PASP, 135, 068001

Gasman, D., van Dishoeck, E. F., Grant, S. L., et al. 2023, A&A, 679, A117

Gasman, D., Temmink, M., van Dishoeck, E. F., et al. 2025, A&A, 694, A147

Geers, V. C., van Dishoeck, E. F., Pontoppidan, K. M., et al. 2009, A&A, 495, 837

Gerakines, P. A., Whittet, D. C. B., Ehrenfreund, P., et al. 1999, ApJ, 522, 357

Giannini, T., Nisini, B., Neufeld, D., et al. 2011, ApJ, 738, 80

Giannini, T., Antoniucci, S., Nisini, B., Bacciotti, F., & Podio, L. 2015, ApJ, 814, 52

Gibb, E. L., Whittet, D. C. B., Boogert, A. C. A., & Tielens, A. G. G. M. 2004, ApJS, 151, 35

Gieser, C., Beuther, H., Semenov, D., et al. 2023a, A&A, 674, A160

Gieser, C., Beuther, H., van Dishoeck, E. F., et al. 2023b, A&A, 679, A108

Ginsburg, A., McGuire, B. A., Sanhueza, P., et al. 2023, ApJ, 942, 66

Godard, B., Pineau des Forêts, G., Lesaffre, P., et al. 2019, A&A, 622, A100

Goldsmith, P. F., Liseau, R., Bell, T. A., et al. 2011, ApJ, 737, 96

González-Alfonso, E., Wright, C. M., Cernicharo, J., et al. 2002, A&A, 386, 1074

Gordon, K. D., Clayton, G. C., Decleir, M., et al. 2023, ApJ, 950, 86

Goto, M., Vasyunin, A. I., Giuliano, B. M., et al. 2021, A&A, 651, A53

Grant, S. L., van Dishoeck, E. F., Tabone, B., et al. 2023, ApJ, 947, L6
Grant, S. L., Kurtovic, N. T., van Dishoeck, E. F., et al. 2024, A&A, 689, A85
GRAVITY Collaboration (Koutoulaki, M., et al.) 2021, A&A, 645, A50
GRAVITY Collaboration (Wojtczak, J. A., et al.) 2023, A&A, 669, A59
Green, J. D., Yang, Y.-L., Evans, II, N. J., et al. 2016, AJ, 151, 75
Greene, T. P., Wilking, B. A., Andre, P., Young, E. T., & Lada, C. J. 1994, ApJ, 434, 614
Greenwood, A. J., Kamp, I., Waters, L. B. F. M., Woitke, P., & Thi, W. F. 2019, A&A, 626, A6
Grim, R. J. A., & Greenberg, J. M. 1987, ApJ, 321, L91
Grim, R. J. A., Greenberg, J. M., de Groot, M. S., et al. 1989, A&AS, 78, 161
Güdel, M., Lahuis, F., Briggs, K. R., et al. 2010, A&A, 519, A113
Gueth, F., & Guilloteau, S. 1999, A&A, 343, 571
Guevara, C., Stutzki, J., Ossenkopf-Okada, V., et al. 2024, A&A, 690, A294
Guillet, V., Jones, A. P., & Pineau Des Forêts, G. 2009, A&A, 497, 145
Guilloteau, S., Bachiller, R., Fuente, A., & Lucas, R. 1992, A&A, 265, L49
Gusdorf, A., Pineau Des Forêts, G., Cabrit, S., & Flower, D. R. 2008, A&A, 490, 695
Harich, S., Yang, X., Yang, X., van Harrevelt, R., & van Hemert, M. 2001, Phys. Rev. Lett., 87
Harsono, D., Jørgensen, J. K., van Dishoeck, E. F., et al. 2014, A&A, 562, A77
Harsono, D., Bruderer, S., & van Dishoeck, E. F. 2015, A&A, 582, A41
Harsono, D., Bjerkeli, P., van der Wiel, M. H. D., et al. 2018, Nat. Astron., 2, 646
Harsono, D., Bjerkeli, P., Ramsey, J. P., et al. 2023, ApJ, 951, L32
Hartigan, P., Raymond, J., & Hartmann, L. 1987, ApJ, 316, 323
Hartmann, L., & Kenyon, S. J. 1996, ARA&A, 34, 207
Hartmann, L., Herczeg, G., & Calvet, N. 2016, ARA&A, 54, 135
Heays, A. N., Visser, R., Gredel, R., et al. 2014, A&A, 562, A61
Helmich, F. P., van Dishoeck, E. F., Black, J. H., et al. 1996, A&A, 315, L173
Henning, T. 2010, ARA&A, 48, 21
Henning, T., Kamp, I., Samland, M., et al. 2024, PASP, 136, 054302
Herbst, E., & van Dishoeck, E. F. 2009, ARA&A, 47, 427
Herczeg, G. J., Brown, J. M., van Dishoeck, E. F., & Pontoppidan, K. M. 2011, A&A, 533, A112
Herczeg, G. J., Karska, A., Bruderer, S., et al. 2012, A&A, 540, A84
Hollenbach, D. 1985, Icarus, 61, 36
Hollenbach, D., & McKee, C. F. 1989, ApJ, 342, 306
Houge, A., Krijt, S., Banzatti, A., et al. 2025, MNRAS, 537, 691
Hsieh, T. H., Segura-Cox, D. M., Pineda, J. E., et al. 2023, A&A, 669, A137
Hudgins, D. M., Sandford, S. A., Allamandola, L. J., & Tielens, A. G. G. M. 1993, ApJS, 86, 713
Hueso, R., & Guillot, T. 2005, A&A, 442, 703
Hull, C. L. H., Girart, J. M., Tychoniec, Ł., et al. 2017, ApJ, 847, 92
Ilee, J. D., Fairlamb, J., Oudmaijer, R. D., et al. 2014, MNRAS, 445, 3723
Ilee, J. D., Cyganowski, C. J., Brogan, C. L., et al. 2018, ApJ, 869, L24
Indriolo, N., Neufeld, D. A., Barr, A. G., et al. 2020, ApJ, 894, 107
Indriolo, N., Neufeld, D. A., DeWitt, C. N., et al. 2015, ApJ, 802, L14
Ioppolo, S., Cuppen, H. M., Romanzin, C., van Dishoeck, E. F., & Linnartz, H. 2008, ApJ, 686, 1474
Ioppolo, S., Sangiorgio, I., Baratta, G. A., & Palumbo, M. E. 2013, A&A, 554, A34
Isokoski, K., Bottinelli, S., & van Dishoeck, E. F. 2013, A&A, 554, A100
Jenkins, E. B. 2009, ApJ, 700, 1299
Jensen, S. S., Jørgensen, J. K., Kristensen, L. E., et al. 2019, A&A, 631, A25
Johnston, K. G., Hoare, M. G., Beuther, H., et al. 2020, ApJ, 896, 35
Jørgensen, J. K., Schöier, F. L., & van Dishoeck, E. F. 2002, A&A, 389, 908
Jørgensen, J. K., Hogerheijde, M. R., van Dishoeck, E. F., Blake, G. A., & Schöier, F. L. 2004, A&A, 413, 993
Jørgensen, J. K., Belloche, A., & Garrod, R. T. 2020, ARA&A, 58, 727
Kalyaan, A., Pinilla, P., Krijt, S., et al. 2023, ApJ, 954, 66
Kama, M., Shorttle, O., Jermyn, A. S., et al. 2019, ApJ, 885, 114
Kamp, I., Henning, T., Arabhavi, A. M., et al. 2023, Faraday Discuss., 245, 112
Kanwar, J., Kamp, I., Jang, H., et al. 2024, A&A, 689, A231
Karska, A., Herczeg, G. J., van Dishoeck, E. F., et al. 2013, A&A, 552, A141
Karska, A., Kaufman, M. J., Kristensen, L. E., et al. 2018, ApJS, 235, 30
Kaufman, M. J., & Neufeld, D. A. 1996, ApJ, 456, 611
Kim, H. J., Evans, Neal J., I., Dunham, M. M., Lee, J.-E., & Pontoppidan, K. M. 2012, ApJ, 758, 38
Knacke, R. F., McCorkle, S., Puetter, R. C., Erickson, E. F., & Kraetschmer, W. 1982, ApJ, 260, 141
Knez, C., Boogert, A. C. A., Pontoppidan, K. M., et al. 2005, ApJ, 635, L145
Knez, C., Lacy, J. H., Evans, Neal J., I., van Dishoeck, E. F., & Richter, M. J. 2009, ApJ, 696, 471
Kóspál, Á., Ábrahám, P., Diehl, L., et al. 2023, ApJ, 945, L7
Kress, M. E., Tielens, A. G. G. M., & Frenklach, M. 2010, Adv. Space Res., 46, 44
Kristensen, L. E., & Dunham, M. M. 2018, A&A, 618, A158
Kristensen, L. E., Visser, R., van Dishoeck, E. F., et al. 2010, A&A, 521, L30
Kristensen, L. E., van Dishoeck, E. F., Tafalla, M., et al. 2011, A&A, 531, L1
Kristensen, L. E., van Dishoeck, E. F., Bergin, E. A., et al. 2012, A&A, 542, A8
Kristensen, L. E., van Dishoeck, E. F., Mottram, J. C., et al. 2017, A&A, 605, A93
Kristensen, L. E., Godard, B., Guillard, P., Gusdorf, A., & Pineau des Forêts, G. 2023, A&A, 675, A86
Krolikowski, D. M., Kraus, A. L., & Rizzuto, A. C. 2021, AJ, 162, 110
Kwan, J., & Fischer, W. 2011, MNRAS, 411, 2383
Lacy, J. H. 2013, ApJ, 765, 130
Lacy, J. H., Evans, Neal J., I., Achtermann, J. M., et al. 1989, ApJ, 342, L43
Lacy, J. H., Carr, J. S., Evans, Neal J., I., et al. 1991, ApJ, 376, 556
Lada, C. J., & Wilking, B. A. 1984, ApJ, 287, 610
Lahuis, F., & van Dishoeck, E. F. 2000, A&A, 355, 699
Lahuis, F., van Dishoeck, E. F., Boogert, A. C. A., et al. 2006, ApJ, 636, L145
Lahuis, F., Spoon, H. W. W., Tielens, A. G. G. M., et al. 2007, ApJ, 659, 296
Lahuis, F., van Dishoeck, E. F., Jørgensen, J. K., Blake, G. A., & Evans, N. J. 2010, A&A, 519, A3
Law, D. R., E. Morrison, J., Argyriou, I., et al. 2023, AJ, 166, 45
Le Gouellec, V. J. M., Hull, C. L. H., Maury, A. J., et al. 2019, ApJ, 885, 106
Le Gouellec, V. J. M., Greene, T. P., Hillenbrand, L. A., & Yates, Z. 2024, ApJ, 966, 91
Le Gouellec, V. J. M., Lew, B. W. P., Greene, T. P., et al. 2025, ApJ, 985, 225
Lee, C.-F. 2015, in IAU General Assembly, 29, 2230421
Lee, C.-F. 2020, A&A Rev., 28, 1
Lee, C.-F., Hirano, N., Palau, A., et al. 2009, ApJ, 699, 1584
Lee, J.-E., Bergin, E. A., & Nomura, H. 2010, ApJ, 710, L21
Lee, J., Lee, J.-E., Lee, S., et al. 2013, ApJS, 209, 4
Lee, C.-F., Ho, P. T. P., Li, Z.-Y., et al. 2017, Nat. Astron., 1, 0152
Lehmann, A., Godard, B., Pineau des Forêts, G., Vidal-García, A., & Falgarone, E. 2022, A&A, 658, A165
Lenzuni, P., Gail, H.-P., & Henning, T. 1995, ApJ, 447, 848
Li, J., Bergin, E. A., Blake, G. A., Ciesla, F. J., & Hirschmann, M. M. 2021, Sci. Adv., 7, eabd3632
Li, J., Boogert, A., Barr, A. G., et al. 2023, ApJ, 953, 103
Li, J., Boogert, A., & Tielens, A. G. G. M. 2024, ApJS, 273, 32
Linsky, J. L., Draine, B. T., Moos, H. W., et al. 2006, ApJ, 647, 1106
Lis, D. C., Güsten, R., Goldsmith, P. F., et al. 2024, A&A, 691, A116
Liseau, R., Goldsmith, P. F., Larsson, B., et al. 2012, A&A, 541, A73
Liu, X., van Dishoeck, E. F., Hogerheijde, M. R. et al., 2025, A&A, submitted
Lodders, K. 2003, ApJ, 591, 1220
Madden, M. C. L., Boogert, A. C. A., Chiar, J. E., et al. 2022, ApJ, 930, 2
Mah, J., Bitsch, B., Pascucci, I., & Henning, T. 2023, A&A, 677, L7
Mah, J., Savvidou, S., & Bitsch, B. 2024, A&A, 686, L17
Manara, C. F., Morbidelli, A., & Guillot, T. 2018, A&A, 618, L3
Manara, C. F., Ansdell, M., Rosotti, G. P., et al. 2023, in Astronomical Society of the Pacific Conference Series, 534, Protostars and Planets VII, eds. S. Inutsuka, Y. Aikawa, T. Muto, K. Tomida, & M. Tamura, 539
Manfroid, J., Hutsemékers, D., & Jehin, E. 2021, Nature, 593, 372
Manoj, P., Watson, D. M., Neufeld, D. A., et al. 2013, ApJ, 763, 83
Maret, S., Bergin, E. A., Neufeld, D. A., et al. 2009, ApJ, 698, 1244
Maud, L. T., Cesaroni, R., Kumar, M. S. N., et al. 2019, A&A, 627, L6
McCaughrean, M. J., Rayner, J. T., & Zinnecker, H. 1994, ApJ, 436, L189
McClure, M. 2009, ApJ, 693, L81
McClure, M. K., Rocha, W. R. M., Pontoppidan, K. M., et al. 2023, Nat. Astron., 7, 431
McClure, M. K., van 't Hoff, M., Francis, L., et al. 2025, Nature, in press, `https://doi.org/10.1038/s41586-025-09163-z`
Meijerink, R., Pontoppidan, K. M., Blake, G. A., Poelman, D. R., & Dullemond, C. P. 2009, ApJ, 704, 1471
Melnick, G. J., Tolls, V., Neufeld, D. A., et al. 2008, ApJ, 683, 876
Min, M., Hovenier, J. W., & de Koter, A. 2005, A&A, 432, 909
Miotello, A., Kamp, I., Birnstiel, T., Cleeves, L. C., & Kataoka, A. 2023, in Astronomical Society of the Pacific Conference Series, 534, Protostars and Planets VII, eds. S. Inutsuka, Y. Aikawa, T. Muto, K. Tomida, & M. Tamura, 501
Miyauchi, N., Hidaka, H., Chigai, T., et al. 2008, Chem. Phys. Lett., 456, 27
Molinari, S., Faustini, F., Testi, L., et al. 2008, A&A, 487, 1119
Moscadelli, L., Sanna, A., Beuther, H., Oliva, A., & Kuiper, R. 2022, Nat. Astron., 6, 1068
Mottram, J. C., van Dishoeck, E. F., Schmalzl, M., et al. 2013, A&A, 558, A126
Mottram, J. C., van Dishoeck, E. F., Kristensen, L. E., et al. 2017, A&A, 600, A99
Mulas, G., Baratta, G. A., Palumbo, M. E., & Strazzulla, G. 1998, A&A, 333, 1025
Müller, B., Giuliano, B. M., Bizzocchi, L., Vasyunin, A. I., & Caselli, P. 2018, A&A, 620, A46

Murillo, N. M., Lai, S.-P., Bruderer, S., Harsono, D., & van Dishoeck, E. F. 2013, A&A, 560, A103
Murillo, N. M., van Dishoeck, E. F., Hacar, A., Harsono, D., & Jørgensen, J. K. 2022, A&A, 658, A53
Myers, P. C., Mardones, D., Tafalla, M., Williams, J. P., & Wilner, D. J. 1996, ApJ, 465, L133
Najita, J., Carr, J. S., & Mathieu, R. D. 2003, ApJ, 589, 931
Najita, J. R., Carr, J. S., Pontoppidan, K. M., et al. 2013, ApJ, 766, 134
Narang, M., Manoj, P., Tyagi, H., et al. 2024, ApJ, 962, L16
Nazari, P., Tabone, B., & Rosotti, G. P. 2023, A&A, 671, A107
Nazari, P., Rocha, W. R. M., Rubinstein, A. E., et al. 2024a, A&A, 686, A71
Nazari, P., Tabone, B., Ahmadi, A., et al. 2024b, A&A, 686, A201
Neufeld, D. A., & Hollenbach, D. J. 1994, ApJ, 428, 170
Neufeld, D. A., Melnick, G. J., Sonnentrucker, P., et al. 2006, ApJ, 649, 816
Neufeld, D. A., Nisini, B., Giannini, T., et al. 2009, ApJ, 706, 170
Neufeld, D. A., Manoj, P., Tyagi, H., et al. 2024, ApJ, 966, L22
Nisini, B., Giannini, T., & Lorenzetti, D. 2002, ApJ, 574, 246
Nisini, B., Antoniucci, S., Giannini, T., & Lorenzetti, D. 2005, A&A, 429, 543
Nisini, B., Benedettini, M., Codella, C., et al. 2010, A&A, 518, L120
Nisini, B., Santangelo, G., Antoniucci, S., et al. 2013, A&A, 549, A16
Nisini, B., Santangelo, G., Giannini, T., et al. 2015, ApJ, 801, 121
Nisini, B., Navarro, M. G., Giannini, T., et al. 2024, ApJ, 967, 168
Nomura, H., Furuya, K., Cordiner, M. A., et al. 2023, in Astronomical Society of the Pacific Conference Series, 534, Protostars and Planets VII, eds. S. Inutsuka, Y. Aikawa, T. Muto, K. Tomida, & M. Tamura, 1075
Noriega-Crespo, A., Morris, P., Marleau, F. R., et al. 2004, ApJS, 154, 352
Notsu, S., van Dishoeck, E. F., Walsh, C., Bosman, A. D., & Nomura, H. 2021, A&A, 650, A180
Novozamsky, J. H., Schutte, W. A., & Keane, J. V. 2001, A&A, 379, 588
Öberg, K. I., & Bergin, E. A. 2021, Phys. Rep., 893, 1
Öberg, K. I., Boogert, A. C. A., Pontoppidan, K. M., et al. 2011, ApJ, 740, 109
Öberg, K. I., Facchini, S., & Anderson, D. E. 2023, ARA&A, 61, 287
Ohashi, N., Tobin, J. J., Jørgensen, J. K., et al. 2023, ApJ, 951, 8
Okoda, Y., Yang, Y.-L., Evans, II, N. J., et al. 2025, ApJ, 982, 149
Ortiz-León, G. N., Loinard, L., Dzib, S. A., et al. 2018, ApJ, 865, 73
Panoglou, D., Cabrit, S., Pineau Des Forêts, G., et al. 2012, A&A, 538, A2
Pascucci, I., Hollenbach, D., Najita, J., et al. 2007, ApJ, 663, 383
Pascucci, I., Herczeg, G., Carr, J. S., & Bruderer, S. 2013, ApJ, 779, 178
Pascucci, I., Cabrit, S., Edwards, S., et al. 2023, in Astronomical Society of the Pacific Conference Series, 534, Protostars and Planets VII, eds. S. Inutsuka, Y. Aikawa, T. Muto, K. Tomida, & M. Tamura, 567
Pascucci, I., Beck, T. L., Cabrit, S., et al. 2025, Nat. Astron., 9, 81
Perotti, G., Rocha, W. R. M., Jørgensen, J. K., et al. 2020, A&A, 643, A48
Perotti, G., Christiaens, V., Henning, T., et al. 2023, Nature, 620, 516
Persson, M. V., Jørgensen, J. K., van Dishoeck, E. F., & Harsono, D. 2014, A&A, 563, A74
Persson, M. V., Harsono, D., Tobin, J. J., et al. 2016, A&A, 590, A33
Pineda, J. E., Segura-Cox, D., Caselli, P., et al. 2020, Nat. Astron., 4, 1158
Pineda, J. E., Arzoumanian, D., Andre, P., et al. 2023, in Astronomical Society of the Pacific Conference Series, 534, Protostars and Planets VII, eds. S. Inutsuka, Y. Aikawa, T. Muto, K. Tomida, & M. Tamura, 233
Podio, L., Bacciotti, F., Nisini, B., et al. 2006, A&A, 456, 189
Podio, L., Tabone, B., Codella, C., et al. 2021, A&A, 648, A45
Podio, L., Ceccarelli, C., Codella, C., et al. 2024, A&A, 688, L22
Pontoppidan, K. M., Blake, G. A., van Dishoeck, E. F., et al. 2008, ApJ, 684, 1323
Pontoppidan, K. M., Fraser, H. J., Dartois, E., et al. 2003, A&A, 408, 981
Pontoppidan, K. M., van Dishoeck, E. F., & Dartois, E. 2004, A&A, 426, 925
Pontoppidan, K. M., Salyk, C., Bergin, E. A., et al. 2014, Protostars & Planets VI, eds. Beuther, H., Klessen, R., Dullemond, K., & Henning, Th. (Tucson: University of Arizona Press), 363
Pontoppidan, K. M., Evans, N., Bergner, J., & Yang, Y.-L. 2024a, RNAAS, 8, 68
Pontoppidan, K. M., Salyk, C., Banzatti, A., et al. 2024b, ApJ, 963, 158
Przybilla, N., Nieva, M.-F., & Butler, K. 2008, ApJ, 688, L103
Pudritz, R. E., & Norman, C. A. 1986, ApJ, 301, 571
Rachid, M. G., Brunken, N., de Boe, D., et al. 2021, A&A, 653, A116
Rachid, M. G., Rocha, W. R. M., & Linnartz, H. 2022, A&A, 665, A89
Raga, A., & Cabrit, S. 1993, A&A, 278, 267
Raunier, S., Chiavassa, T., Marinelli, F., Allouche, A., & Aycard, J.-P. 2003, J. Phys. Chem. A, 107, 9335
Ray, T. P., & Ferreira, J. 2021, New A Rev., 93, 101615
Ray, T., Dougados, C., Bacciotti, F., Eislöffel, J., & Chrysostomou, A. 2007, in Protostars and Planets V, eds. B. Reipurth, D. Jewitt, & K. Keil, 231
Ray, T. P., McCaughrean, M. J., Caratti o Garatti, A., et al. 2023, Nature, 622, 48
Reipurth, B., & Bally, J. 2001, ARA&A, 39, 403
Reipurth, B., Bally, J., & Devine, D. 1997, AJ, 114, 2708
Reiter, M., Kiminki, M. M., Smith, N., & Bally, J. 2017, MNRAS, 467, 4441
Rieke, G. H., Wright, G. S., Böker, T., et al. 2015, PASP, 127, 584
Rigby, J., Perrin, M., McElwain, M., et al. 2023, PASP, 135, 048001
Rigliaco, E., Pascucci, I., Duchene, G., et al. 2015, ApJ, 801, 31
Rocha, W. R. M., Perotti, G., Kristensen, L. E., & Jørgensen, J. K. 2021, A&A, 654, A158
Rocha, W. R. M., Rachid, M. G., Olsthoorn, B., et al. 2022, A&A, 668, A63
Rocha, W. R. M., van Dishoeck, E. F., Ressler, M. E., et al. 2024, A&A, 683, A124
Rocha, W. R. M., McClure, M. K., Sturm, J. A., et al. 2025, A&A, 693, A288
Rohde, P. F., Walch, S., Seifried, D., et al. 2019, MNRAS, 483, 2563
Romanova, M. M., Ustyugova, G. V., Koldoba, A. V., & Lovelace, R. V. E. 2005, ApJ, 635, L165
Romero-Mirza, C. E., Banzatti, A., Öberg, K. I., et al. 2024, ApJ, 975, 78
Rosenthal, D., Bertoldi, F., & Drapatz, S. 2000, A&A, 356, 705
Rubin, M., Altwegg, K., Balsiger, H., et al. 2019, MNRAS, 489, 594
Rubinstein, A. E., Evans, N. J., Tyagi, H., et al. 2024, ApJ, 974, 112
Sadavoy, S. I., Di Francesco, J., André, P., et al. 2014, ApJ, 787, L18
Sakai, N., Sakai, T., Hirota, T., et al. 2014, Nature, 507, 78
Salyk, C., Pontoppidan, K. M., Blake, G. A., et al. 2008, ApJ, 676, L49
Salyk, C., Blake, G. A., Boogert, A. C. A., & Brown, J. M. 2009, ApJ, 699, 330
Salyk, C., Pontoppidan, K. M., Blake, G. A., Najita, J. R., & Carr, J. S. 2011, ApJ, 731, 130
Salyk, C., Yang, Y.-L., Pontoppidan, K. M., et al. 2024, ApJ, 974, 97
Sargent, B. A., Forrest, W. J., Tayrien, C., et al. 2009, ApJS, 182, 477
Savage, B. D., & Sembach, K. R. 1996, ARA&A, 34, 279
Schilke, P., Walmsley, C. M., Pineau des Forets, G., & Flower, D. R. 1997, A&A, 321, 293
Schneider, N., Röllig, M., Simon, R., et al. 2018, A&A, 617, A45
Schutte, W. A., & Khanna, R. K. 2003, A&A, 398, 1049
Schutte, W. A., Boogert, A. C. A., Tielens, A. G. G. M., et al. 1999, A&A, 343, 966
Schwarz, K. R., Henning, T., Christiaens, V., et al. 2024, ApJ, 962, 8
Seidensticker, K. J., & Schmidt-Kaler, T. 1989, A&A, 225, 192
Sellek, A. D., Vlasblom, M., & van Dishoeck, E. F. 2025, A&A, 694, A79
Shang, H., Liu, C.-F., Krasnopolsky, R., & Wang, L.-Y. 2023, ApJ, 944, 230
Slavicinska, K., Rachid, M. G., Rocha, W. R. M., et al. 2023, A&A, 677, A13
Slavicinska, K., van Dishoeck, E. F., Tychoniec, Ł., et al. 2024, A&A, 688, A29
Slavicinska, K., Boogert, A. C. A., Tychoniec, Ł., et al. 2025a, A&A, 693, A146
Slavicinska, K., Tychoniec, Ł., Navarro, M. G., et al. 2025b, ApJL, in press, [arXiv:2505.14686]
Smith, N., Bally, J., Shuping, R. Y., Morris, M., & Kassis, M. 2005, AJ, 130, 1763
Snellen, I. 2025, ARA&A, in press [arXiv:2505.08926]
Sonnentrucker, P., González-Alfonso, E., & Neufeld, D. A. 2007, ApJ, 671, L37
Spaans, M., Hogerheijde, M. R., Mundy, L. G., & van Dishoeck, E. F. 1995, ApJ, 455, L167
Speedie, J., Dong, R., Teague, R., et al. 2025, ApJ, 981, L30
Sridharan, T. K., Beuther, H., Schilke, P., Menten, K. M., & Wyrowski, F. 2002, ApJ, 566, 931
Stäuber, P., Doty, S. D., van Dishoeck, E. F., & Benz, A. O. 2005, A&A, 440, 949
Stäuber, P., Benz, A. O., Jørgensen, J. K., et al. 2007, A&A, 466, 977
Tabone, B., Cabrit, S., Bianchi, E., et al. 2017, A&A, 607, L6
Tabone, B., Godard, B., Pineau des Forêts, G., Cabrit, S., & van Dishoeck, E. F. 2020, A&A, 636, A60
Tabone, B., van Hemert, M. C., van Dishoeck, E. F., & Black, J. H. 2021, A&A, 650, A192
Tabone, B., Bettoni, G., van Dishoeck, E. F., et al. 2023, Nat. Astron., 7, 805
Tafalla, M., Liseau, R., Nisini, B., et al. 2013, A&A, 551, A116
Tappe, A., Lada, C. J., Black, J. H., & Muench, A. A. 2008, ApJ, 680, L117
Tappe, A., Forbrich, J., Martín, S., Yuan, Y., & Lada, C. J. 2012, ApJ, 751, 9
Taquet, V., Furuya, K., Walsh, C., & van Dishoeck, E. F. 2016, MNRAS, 462, S99
Taquet, V., van Dishoeck, E. F., Swayne, M., et al. 2018, A&A, 618, A11
Temmink, M., van Dishoeck, E. F., Gasman, D., et al. 2024a, A&A, 689, A330
Temmink, M., van Dishoeck, E. F., Grant, S. L., et al. 2024b, A&A, 686, A117
Temmink, M., Sellek, A. D., Gasman, D., et al. 2025, A&A, 699, A134
Terwisscha van Scheltinga, J., Ligterink, N. F. W., Boogert, A. C. A., van Dishoeck, E. F., & Linnartz, H. 2018, A&A, 611, A35
Terwisscha van Scheltinga, J., Marcandalli, G., McClure, M. K., Hogerheijde, M. R., & Linnartz, H. 2021, A&A, 651, A95
Tielens, A. G. G. M., & Hagen, W. 1982, A&A, 114, 245
Tielens, A. G. G. M., McKee, C. F., Seab, C. G., & Hollenbach, D. J. 1994, ApJ, 431, 321
Tobin, J. J., & Sheehan, P. D. 2024, ARA&A, 62, 203
Tobin, J. J., Looney, L. W., Li, Z.-Y., et al. 2016, ApJ, 818, 73
Tobin, J. J., Megeath, S. T., van't Hoff, M., et al. 2019, ApJ, 886, 6
Tobin, J. J., van't Hoff, M. L. R., Leemker, M., et al. 2023, Nature, 615, 227
Tofflemire, B. M., Manara, C. F., Banzatti, A., et al. 2025, ApJ, 985, 224

Tyagi, H., Manoj, P., Narang, M., et al. 2025, ApJ, 983, 110
Tychoniec, Ł., Manara, C. F., Rosotti, G. P., et al. 2020, A&A, 640, A19
Tychoniec, Ł., van Dishoeck, E. F., van't Hoff, M. L. R., et al. 2021, A&A, 655, A65
Tychoniec, Ł., van Gelder, M. L., van Dishoeck, E. F., et al. 2024, A&A, 687, A36
Urquhart, J. S., König, C., Giannetti, A., et al. 2018, MNRAS, 473, 1059
Valdivia-Mena, M. T., Pineda, J. E., Caselli, P., et al. 2024, A&A, 687, A71
van Broekhuizen, F. A., Keane, J. V., & Schutte, W. A. 2004, A&A, 415, 425
van de Voort, F., Quataert, E., Faucher-Giguère, C.-A., et al. 2018, MNRAS, 477, 80
van der Tak, F. F. S., Black, J. H., Schöier, F. L., Jansen, D. J., & van Dishoeck, E. F. 2007, A&A, 468, 627
van der Tak, F. F. S., Lique, F., Faure, A., Black, J. H., & van Dishoeck, E. F. 2020, Atoms, 8, 15
van Dishoeck, E. F. 2004, ARA&A, 42, 119
van Dishoeck, E. F., & Black, J. H. 1988, ApJ, 334, 771
van Dishoeck, E. F., & Helmich, F. P. 1996, A&A, 315, L177
van Dishoeck, E. F., & Blake, G. A. 1998, ARA&A, 36, 317
van Dishoeck, E. F., Kristensen, L. E., Mottram, J. C., et al. 2021, A&A, 648, A24
van Dishoeck, E. F., Grant, S., Tabone, B., et al. 2023, Faraday Discuss., 245, 52
van Gelder, M. L., Francis, L., van Dishoeck, E. F., et al. 2024a, A&A, 692, A197
van Gelder, M. L., Ressler, M. E., van Dishoeck, E. F., et al. 2024b, A&A, 682, A78
van Harrevelt, R., & van Hemert, M. 2000, J. Chem. Phys., 112, 5787
van Kempen, T. A., Kristensen, L. E., Herczeg, G. J., et al. 2010, A&A, 518, L121
Vandenbussche, B., Ehrenfreund, P., Boogert, A. C. A., et al. 1999, A&A, 346, L57
van't Hoff, M. L. R., Harsono, D., Tobin, J. J., et al. 2020, ApJ, 901, 166
Varricatt, W. P., Davis, C. J., Ramsay, S., & Todd, S. P. 2010, MNRAS, 404, 661
Velusamy, T., Langer, W. D., & Marsh, K. A. 2007, ApJ, 668, L159
Villenave, M., Ménard, F., Dent, W. R. F., et al. 2020, A&A, 642, A164
Villenave, M., Podio, L., Duchêne, G., et al. 2023, ApJ, 946, 70
Visser, R., van Dishoeck, E. F., Doty, S. D., & Dullemond, C. P. 2009, A&A, 495, 881
Vlasblom, M., van Dishoeck, E. F., Tabone, B., & Bruderer, S. 2024, A&A, 682, A91
Vlasblom, M., Temmink, M., Grant, S. L., et al. 2025, A&A, 693, A278
Walsh, C., Nomura, H., Millar, T. J., & Aikawa, Y. 2012, ApJ, 747, 114
Walsh, C., Nomura, H., & van Dishoeck, E. 2015, A&A, 582, A88
Wang, Y., Zhang, Q., Pillai, T., Wyrowski, F., & Wu, Y. 2008, ApJ, 672, L33
Watson, D. M., Bohac, C. J., Hull, C., et al. 2007, Nature, 448, 1026
Watson, D. M., Calvet, N. P., Fischer, W. J., et al. 2016, ApJ, 828, 52
Weingartner, J. C., & Draine, B. T. 2001, ApJ, 548, 296
Wells, M., Pel, J. W., Glasse, A., et al. 2015, PASP, 127, 646
Whittet, D. C. B. 2010, ApJ, 710, 1009
Whittet, D. C. B., Pendleton, Y. J., Gibb, E. L., et al. 2001, ApJ, 550, 793
Whittet, D. C. B., Cook, A. M., Chiar, J. E., et al. 2009, ApJ, 695, 94
Williams, G. M., Cyganowski, C. J., Brogan, C. L., et al. 2022, MNRAS, 509, 748
Woitke, P., Min, M., Thi, W. F., et al. 2018, A&A, 618, A57
Wright, C. M., van Dishoeck, E. F., Cox, P., Sidher, S. D., & Kessler, M. F. 1999, ApJ, 515, L29
Wright, G. S., Rieke, G. H., Glasse, A., et al. 2023, PASP, 135, 048003
Wyrowski, F., Güsten, R., Menten, K. M., et al. 2016, A&A, 585, A149
Xie, C., Pascucci, I., Long, F., et al. 2023, ApJ, 959, L25
Xu, Y., Moscadelli, L., Reid, M. J., et al. 2011, ApJ, 733, 25
Yang, Y.-L., Evans, II, N. J., Green, J. D., Dunham, M. M., & Jørgensen, J. K. 2017, ApJ, 835, 259
Yang, Y.-L., Evans, II, N. J., Smith, A., et al. 2020, ApJ, 891, 61
Yang, Y.-L., Green, J. D., Pontoppidan, K. M., et al. 2022, ApJ, 941, L13
Yen, H.-W., Koch, P. M., Takakuwa, S., et al. 2017, ApJ, 834, 178
Yıldız, U. A., Kristensen, L. E., van Dishoeck, E. F., et al. 2012, A&A, 542, A86
Yıldız, U. A., Acharyya, K., Goldsmith, P. F., et al. 2013, A&A, 558, A58
Yıldız, U. A., Kristensen, L. E., van Dishoeck, E. F., et al. 2015, A&A, 576, A109
Yuan, Y., Neufeld, D. A., Sonnentrucker, P., Melnick, G. J., & Watson, D. M. 2012, ApJ, 753, 126
Yvart, W., Cabrit, S., Pineau des Forêts, G., & Ferreira, J. 2016, A&A, 585, A74
Zannese, M., Tabone, B., Habart, E., et al. 2024, Nat. Astron., 8, 577
Zhang, Y., Snellen, I. A. G., & Mollière, P. 2021, A&A, 656, A76
Zhou, L., Xie, D., & Guo, H. 2015, J. Chem. Phys., 142, 124317

---

[1] Leiden Observatory, Leiden University, PO Box 9513, 2300 RA Leiden, The Netherlands
[2] Max Planck Institut für Extraterrestrische Physik (MPE), Giessenbachstrasse 1, 85748 Garching, Germany
[3] Laboratory for Astrophysics, Leiden Observatory, Leiden University, PO Box 9513, 2300 RA Leiden, The Netherlands
[4] School of Cosmic Physics, Dublin Institute for Advanced Studies, 31 Fitzwilliam Place, D02 XF86, Dublin, Ireland
[5] Max Planck Institute for Astronomy, Königstuhl 17, 69117 Heidelberg, Germany
[6] INAF–Osservatorio Astronomico di Capodimonte, Salita Moiariello 16, 80131 Napoli, Italy
[7] UK Astronomy Technology Centre, Royal Observatory Edinburgh, Blackford Hill, Edinburgh EH9 3HJ, UK
[8] Space Science and Astrobiology Division, NASA's Ames Research Center, Moffett Field, CA 94035, USA
[9] Department of Space, Earth and Environment, Chalmers University of Technology, Onsala Space Observatory, 439 92 Onsala, Sweden
[10] Institut de Ciencies de l'Espai (ICE-CSIC), Campus UAB, Carrer de Can Magrans S/N, 08193 Cerdanyola del Valles, Catalonia, Spain
[11] Institut d'Estudis Espacials de Catalunya (IEEC), c/ Gran Capitá, 2–4, 08034 Barcelona, Spain
[12] Department of Physics, Maynooth University, Maynooth, Co. Kildare, Ireland
[13] INAF–Osservatorio Astronomico di Roma, Via di Frascati 33, 00078 Monte Porzio Catone, Italy
[14] European Southern Observatory (ESO), Karl-Schwarzschild-Strasse 2, 1780 85748 Garching, Germany
[15] Department of Earth and Planetary Science, Graduate School of Science, University of Tokyo, 7-3-1 Hongo, Bunkyo-ku, Tokyo 113-0033, Japan
[16] Star and Planet Formation Laboratory, RIKEN Cluster for Pioneering Research, 2-1 Hirosawa, Wako, Saitama 351-0198, Japan
[17] Niels Bohr Institute, University of Copenhagen, NBB BA2, Jagtvej 155A, 2200 Copenhagen, Denmark
[18] Jet Propulsion Laboratory, California Institute of Technology, 4800 Oak Grove Drive, Pasadena, CA 91109, USA
[19] Université Paris-Saclay, CNRS, Institut d'Astrophysique Spatiale, 91405 Orsay, France
[20] Centro de Astrobiologıa (CAB) CSIC-INTA, Ctra. de Ajalvir km 4, Torrejøn de Ardøz, 28850, Madrid, Spain
[21] Department of Astrophysics, University of Vienna, Türkenschanzstrasse 17, 1180 Vienna, Austria
[22] ETH Zürich, Institute for Particle Physics and Astrophysics, Wolfgang-Pauli-Strasse 27, 8093 Zürich, Switzerland
[23] Université Paris-Saclay, Université Paris Cité, CEA, CNRS, AIM, 91191 Gif-sur-Yvette, France
[24] Department of Astronomy, Oskar Klein Centre, Stockholm University, AlbaNova University Center, 10691 Stockholm, Sweden
[25] Institute of Astronomy, KU Leuven, Celestijnenlaan 200D, 3001 Leuven, Belgium

Appendix A: Source positions

Table 1 contains the coordinates and properties of the JOYS sources. See also Table A.1 in van Gelder et al. (2024a) for more information on the low-mass sources. Table A.1 contains more information on the observational set-up.

Appendix B: Scientific background

This section presents background information on the science cases addressed in this paper as well as the motivation for using JWST-MIRI in more detail than described in Sect. 2.3. To avoid interrupting the flow of the results in Sections 4–8, this information is contained here in a single section. See also Sect. 2 for terminology.

B.1. Protostellar accretion

Most of the protostellar accretion occurs in the earliest, deeply embedded stages (e.g., Lada & Wilking 1984; Hartmann et al. 2016) but there are very few direct measurements of the rates at which this process occurs. The H I recombination lines are thought to be good tracers if they are produced primarily in the accretion column onto the forming star (magnetospheric accretion). Most notably, the H I 7–6 Humphries α line at 12.37 μm has been proposed as an accretion tracer for highly extincted sources for which more commonly used shorter wavelength tracers like Brackett γ cannot be observed (Rigliaco et al. 2015). However, H I recombination lines may also be produced in jet/wind shocks or circumstellar photoionized gas. The high spatial resolution imaging of the H I lines offered by MIRI is important to disentangle these processes. Beuther et al. (2023) provide the first JOYS application of H I for the IRAS 23385+6053 high-mass protostar. We note that these disk-to-protostar accretion rates should not be confused with the cloud-to-envelope-to-disk gas infall rates measured on larger scales (Myers et al. 1996; Mottram et al. 2013; Wyrowski et al. 2016) and are not necessarily the same (Dunham et al. 2014).

Accretion is known to be an episodic phenomenon, with accretion rates varying by orders of magnitude during the main accretion phase (Hartmann & Kenyon 1996; Frank et al. 2014; Fischer et al. 2023). Since ejection and accretion processes are closely linked, these episodic events have also historically been traced through “bullets” or “knots” in the jets away from the central source, where they are more easily observed at near-infrared wavelengths (Reipurth et al. 1997; Bally 2016; Lee 2020). Models of outflow propagation show that many of these “knots” can naturally be explained by variations in the jet ejection velocity, with high velocity blobs within the jet producing shocks as they catch up with the slower moving flow within the jet (Raga & Cabrit 1993; Bonito et al. 2010; Rohde et al. 2019; Shang et al. 2023). This hypothesis of linked accretion and ejection is supported by a handful of observed cases where an outburst in a protostellar system has been followed by the appearance of a new knot (Ellerbroek et al. 2014; Fedriani et al. 2023; Cesaroni et al. 2025). With its high angular resolution over a wide area, JWST NIRCam offers new opportunities to survey these knots closer to the protostar and in more extincted regions than before.

Another opportunity for JWST is that of time domain studies. The JWST NIRCam study of the HH 211 outflow by Ray et al. (2023) has demonstrated the use of accurate imaging over a 20 year period for determining the proper motions and tangential velocity of the jet knots. Another example is provided by the change in the mid-infrared SED of some protostars like EC 53 during the outburst cycle as material builds up in the inner disk (e.g., Connelley & Reipurth 2018; Baek et al. 2020; Francis et al. 2022). This could cause molecular lines to shift from emission to absorption as the disk midplane is heated by accretion and thus serve as a valuable diagnostic (McClure et al. 2025). Similarly, some mid-infrared ice bands are excellent signatures of thermal processing, most notably the $^{12}CO_2$ 15 μm band (Ehrenfreund et al. 1998, 1999; Pontoppidan et al. 2008; Kim et al. 2012) and now also the $^{13}CO_2$ 4.38 μm band observed with JWST as part of the IPA program (Brunken et al. 2024a).

B.2. Protostellar jets, winds, and outflows

Jets and outflows are seen from young stars up to ~2 Myr age, spanning all protostellar phases from Class 0 to Class II, and for low- and high-mass protostars, and are one of the most striking phenomena in astrophysics (see reviews by Reipurth & Bally 2001; Ray et al. 2007; Arce et al. 2007; Frank et al. 2014; Bally 2016; Lee 2020). Not only are they supersonic and highly collimated but they can stretch for several parsecs, even beyond the boundaries of their molecular cloud. Since mass loss and accretion rates are closely coupled (Beuther et al. 2002), jets and winds are most powerful in the earliest evolutionary stage and can be used as a proxy for past activity (see Sect. 4). In fact, estimates suggest that ~10% of the accreted mass is ultimately ejected, a number that may change with evolutionary state and be as high as 100% in some MHD disk-wind models at the earliest stages (Pascucci et al. 2023). As the statistically estimated lifetime of the low-mass Class 0 phase is only about 5×10^4 years (Evans et al. 2009; Kristensen & Dunham 2018), associated outflows in the deeply embedded phase are not as big in their extent as those from more evolved sources. They are, however, a full trace of the activity since the birth of the protostar.

Despite their clear importance, there are still many questions about the physics of the jets, winds, and outflows from the youngest protostars. In large part this is because they are deeply embedded, particularly in the earliest stages and in the region close to the source. Protostellar jets have so far mainly been probed in the near-infrared at larger distances from the source via the vibrationally excited H_2 lines tracing temperatures in excess of 1000 K and the near-infrared forbidden [Fe II] lines tracing hot ionized gas (e.g., Nisini et al. 2005; Podio et al. 2006; Giannini et al. 2011). In contrast, millimeter images of CO pure rotational lines commonly trace the slower moving entrained cold ambient gas, whereas SiO and H_2O lines reveal higher velocity jets in some but not all sources (e.g., Guilloteau et al. 1992; Bachiller & Tafalla 1999; Kristensen et al. 2011; Podio et al. 2021; Bally 2016). In a few cases, also disk winds, i.e., wider angle (poorly collimated) and slower moving material that is launched from a larger range of disk radii than the jets, are found (Lee et al. 2017; Tabone et al. 2017; Nazari et al. 2024b). Figure 1 illustrates these components.

The near-infrared and millimeter are two extremes in wavelength with only limited information on the intermediate temperature regime. To observe the much more highly collimated underlying jet propelling forward these outflows close to the source at velocities close to the gravitational escape velocity ($\approx$ 100–300 km s^{-1} for low-mass sources), they have to be studied in the mid- and far-infrared. The usefulness of mid-infrared observations of outflows from Class 0 sources has been demonstrated using *Spitzer-IRS* (e.g., Neufeld et al. 2006, 2009; Melnick et al. 2008; Maret et al. 2009; Lahuis et al. 2010). Although they are

Table A.1. Main MIRI-MRS observational details of the sample of JOYS sources in the PID 1290 JWST GTO program.

ID	Archive name	Sources	RA J2000	Dec J2000	Dith	Exposure time (s)	Background	Mosaic
1	B1b-S	-	03:33:17.953	+31:09:31.49	2	1005, 1005, 1005	-	1×1
2	B1b	B1-b	03:33:20.341	+31:07:21.36	2	200, 200, 200	B1b-S	1×1
3	B1c-1	B1-c	03:33:17.953	+31:09:31.49	4	2009, 4029, 2009	B1b-S	1×1
4	B1c-2	-	03:33:18.211	+31:09:28.63	2	200, 200, 200	B1b-S	1×1
5	B1a	B1-a-1, 2	03:33:16.669	+31:07:54.90	2	200, 200, 200	B1b-S	1×1
6	IRAS4B	IRAS4B	03:29:12.012	+31:13:07.07	2	200, 200, 200	B1b-S	1×1
7	IRAS4B-b1	-	03:29:12.040	+31:13:01.35	2	200, 200, 200	B1b-S	1×1
8	IRAS4A-b1	-	03:29:10.595	+31:13:19.40	2	200, 200, 200	B1b-S	1×1
9	L1448mm	L1448-mm	03:25:38.761	+30:44:08.16	2	200, 200, 200	B1b-S	2×3
10	Emb-8	Per-emb 8	03:44:43.982	+32:01:35.21	2	200, 200, 200	B1b-S	1×1
11	Dark-Taurus	-	04:39:32.290	+26:05:14.50	1	200, 200, 200	-	1×1
12	L1527-1	L1527 IRS	04:39:53.955	+26:03:09.56	2	1000, 1000, 1000	Dark-Taurus	1×1
13	L1527-2	-	04:39:54.245	+26:03:11.67	2	200, 200, 200	Dark-Taurus	1×1
14	TMC1A	TMC1-A	04:39:35.203	+25:41:45.17	2	216, 216, 216	Dark-Taurus	1×1
15	TMC1	TMC1-W,E	04:41:12.700	+25:46:34.80	2	200, 200, 200	Dark-Taurus	1×1
16	Dark-Serpens	-	18:29:48.250	+01:14:26.20	2	200, 200, 200	-	1×1
17	SVS4-5	SVS 4-5	18:29:57.630	+01:13:00.20	2	605, 605, 605	Dark-Serpens	1×1
18	SerpSMM3	Ser-SMM3	18:29:59.302	+01:14:00.97	2	200, 200, 200	Dark-Serpens	1×1
19	SerpEmb8N	-	18:29:49.269	+01:16:52.62	2	200, 200, 200	Dark-Serpens	1×1
20	SerpS68N	Ser-S68N-N, S	18:29:48.074	+01:16:43.80	2	200, 200, 200	Dark-Serpens	1×1
21	SerpSMM1-2	Ser-SMM1-b1, b2	18:29:49.602	+01:15:21.90	2	200, 200, 200	Dark-Serpens	1×1
22	SerpSMM1-1	Ser-SMM1-a	18:29:49.874	+01:15:19.79	4	200, 200, 200	Dark-Serpens	1×1
23	Dark-BHR71	-	12:01:30:720	-65:08:44.60	2	200, 200, 200	-	1×1
24	BHR71-IRS2	BHR71-IRS2	12:01:34.000	-65:08:47.00	2	200, 200, 200	Dark-BHR71	1×1
25	BHR71-IRS1	BHR71-IRS1	12:01:36.548	-65:08:53.59	2	200, 200, 200	Dark-BHR71	3×3
26	G28IRS2	G28IRS2	18:42:51.967	-3:59:53.985	2	200, 200, 200	-	1×1
27	G28P1	A, B	18:42:50.679	-4:03:14.087	2	799, 799, 799	-	2×2
28	G28S	-	18:42:46.414	-4:04:15.404	2	200, 200, 200	-	1×1
29	Dark-IRAS23385	-	23:41:11.033	61:10:28.928	2	200, 200, 200	-	1×1
30	IRAS23385	A, B	23:40:54.503	61:10:27.846	2	800, 800, 800	Dark-IRAS23385	2×2
31	Dark-IRAS18089	-	18:11:44.112	-17:31:03.047	2	200, 200, 200	-	1×1
32	IRAS18089	A, B, C	18:11:51.447	-17:31:27.285	2	400, 400, 400	Dark-IRAS18089	2×1
33	Dark-G31	-	18:47:32.382	-1:13:44.317	2	200, 200, 200	-	1×1
34	G31	G31	18:47:34.308	-1:12:46.000	2	200, 200, 200	Dark-G31	1×1

Notes. The coordinates are the center position of the observation, not the positions of the protostars. The exposure time is the exposure time divided over the A,B,C gratings. Dith stands for Dithers.

of poor spectral and spatial resolution compared to MIRI, such studies show not only that an underlying atomic component is present but suggest that the mass loss rate in such young jets is much higher than those from less embedded sources of equivalent mass (Dionatos et al. 2009).

Additional information on the physical and chemical structure of jets and outflows has been provided by *Herschel* far-infrared spectroscopic studies. Like *Spitzer*-IRS, the spatial resolution is poor, typically 10–20″, thus probing scales of a few 1000 au. Still, surveys of nearly 100 low- and high-mass protostars with the HIFI and PACS instruments have provided insight into the warm (few hundred K–1000 K) gas using H_2O, OH and CO pure rotational lines up to very high J_u=49 ($E_{\rm up}$ = 6457 K). Two different physical components can be distinguished that are clearly different in temperature and in spatial and velocity distribution from the entrained outflow gas probed by low-J CO lines (Kristensen et al. 2010; van Kempen et al. 2010; Herczeg et al. 2012; Karska et al. 2013; Manoj et al. 2013; Nisini et al. 2013; Tafalla et al. 2013; Green et al. 2016; Mottram et al. 2017; Kristensen et al. 2017; Karska et al. 2018; Dionatos et al. 2018, 2020; van Dishoeck et al. 2021).

The [O I] 63 µm line has also been surveyed with *Herschel*, and is commonly associated with the jets powering the outflows at speeds of more than 90 km s^{-1} with respect to that of the source (van Kempen et al. 2010; Nisini et al. 2015; Dionatos & Güdel 2017; Karska et al. 2018). As the main coolant of the gas (Hollenbach 1985), it can serve as a direct measure of mass loss rates. We note, however, that optical depth, self-absorption or absorption from cold foreground clouds can affect the results inferred from spectrally unresolved [O I] line profiles, as indicated by spectrally resolved [O I] data with SOFIA (e.g., Schneider et al. 2018; Guevara et al. 2024; Lis et al. 2024). Comparison of mass flux rates from [O I] and CO suggests that this atomic gas is not the dominant driver of the entrained outflow gas in the earliest stages: the jets in the Class 0 phase are mostly molecular. However, toward the Class I stage, the jets become mostly atomic (Nisini et al. 2015). This scenario can now be tested with JWST using its diagnostic lines and spectral imaging to compare with the [O I] results both qualitatively and quantitatively.

Finally, the abundances of H_2O, OH and other hydrides and the distribution of ^{13}CO 6–5 emission point to UV fields up to $10^2 - 10^3$ times the general interstellar radiation field in the outflow cavity walls (Spaans et al. 1995; Yıldız et al. 2012; Benz et al. 2016; van Dishoeck et al. 2021). In particular, the H_2O abundance in outflows is low due to UV photodissociation, of order $10^{-7} - 10^{-6}$ (Tafalla et al. 2013; Karska et al. 2018). The limited spatial resolution of *Herschel* and *Spitzer*, however, prevented imaging any of these processes at the base of the outflow in the inner few 100 au.

JWST now provides imaging of a wealth of mid-infrared lines at 10–100 times higher spatial resolution than was possible with *Spitzer*. Their diagnostic potential for studying outflows is summarized in Table D.1. Of prime importance are the [Fe II] and lines of other refractory elements tracing the jets, together with the H_2 lines imaging both the jets and the wider-angle winds. Some kinematic data down to ∼10 km s^{-1} accuracy can be obtained. [Ne II] has been found to trace both jets and photoionized gas in embedded sources using *Spitzer* data (Lahuis et al. 2010; Güdel et al. 2010), which can now be disentangled through direct imaging. [Ne II] versus [Ne III] can provide constraints on the ionizing radiation field (e.g., Espaillat et al. 2013). Comparison of all of these lines with shock models such as those by Hollenbach & McKee (1989) and from the Paris-Durham code (e.g., Godard et al. 2019; Lehmann et al. 2022; Kristensen et al. 2023) then provide constraints on shock velocity and pre-shock densities. The OH mid-infrared " prompt emission" pure rotational lines are proven to be powerful tracers of UV irradiation in deeply embedded regions (e.g., Neufeld et al. 2024).

Even though JWST will not be able to resolve the launching zone of the protostellar jets (the innermost few au), it can investigate the spatial structure and stratification of the jets in their close environment and constrain the launching mechanisms. Also, the structures seen with JWST on small scales can ultimately be linked with the physical components inferred from data at other wavelengths on larger scales. Initial JWST papers on outflows using JOYS data of the HH 211 Class 0 outflow (Caratti o Garatti et al. 2024) and the Class I TMC1 binary source (Tychoniec et al. 2024) indeed reveal a nested jet structure consisting of an ionized core traced by [Fe II] with a molecular layer traced by high-J H_2 surrounding it, with a wider angle wind seen in low-J H_2 lines (see also Federman et al. 2024; Delabrosse et al. 2024). By studying the temperature and chemical structure of such winds, ultimately constraints on their origin may be obtained, in particular whether they are MHD winds (e.g., Pudritz & Norman 1986; Romanova et al. 2005) or photoevaporative winds (e.g., Ercolano & Pascucci 2017).

Another question that MIRI can help answer is whether dust is launched inside jets from Class 0 sources. This, in turn, provides constraints on the launching radius of the jet, in particular whether it is inside or outside the dust sublimation radius (∼1400 K, typically located at <0.1 au for a low-mass protostar, D'Alessio et al. 1997). The presence of dust in jets can either be imaged directly through its mid-infrared continuum, or it can be inferred more indirectly from line ratios of refractory to non-refractory species to determine their depletion. The latter method has been used for Class II sources using near-infrared lines (e.g., Nisini et al. 2002; Podio et al. 2006). While inferred depletion values are not as high as in the general ISM, the gas in optically visible jets has not attained solar abundances, at least close to Class II sources (e.g., Giannini et al. 2015). Thus, this suggests that there is dust in the jet and that it is only gradually destroyed via the mild internal jet shocks, as expected from models of grain destruction in dense gas (e.g., Tielens et al. 1994; Schilke et al. 1997; Gusdorf et al. 2008; Guillet et al. 2009). This raises the obvious question whether dust is even more important in jets from Class 0 sources than in Class I sources. MIRI covers many atomic lines of both refractory and less refractory elements, most notably from [Fe I], [Fe II] and [S I], that can address this issue (e.g., Anderson et al. 2013). The HH 211 MRS map by Caratti o Garatti et al. (2024) directly detects continuum dust emission associated with the base of the jet directly suggesting that dust is indeed launched in jets. It also indicates modest depletions of refractory elements suggesting that not all grains are destroyed. A detailed JOYS case is provided by the BHR 71 IRS1 jet and outflow (Tychoniec et al., in prep.).

Some evidence of dust in outflows can also be found on larger scales from pre-JWST mid-infrared continuum ground-based and *Spitzer* images (e.g., Smith et al. 2005; Velusamy et al. 2007) and in absorption against a background nebula (Reiter et al. 2017). On these scales, dust can also be mixed and entrained into the jet and outflow from the surrounding cloud, especially in regions near the bow shock. This is shown for the HH 211 case at larger distances from the source (Caratti o Garatti et al. 2024).

High-mass protostars have powerful outflows detected in CO millimeter lines, with the CO momentum flux increasing strongly with source luminosity and envelope mass (Bontemps et al. 1996; Beuther et al. 2002; Mottram et al. 2017). These high-mass flows have been much less studied in other diagnostics because of their high extinctions, although several jets that are likely driving such outflows have been detected at near-infrared wavelengths (mostly in H_2) (e.g., Varricatt et al. 2010; Lee et al. 2013; Caratti o Garatti et al. 2015). Many of the IRDC regions exhibit so-called green fuzzies or extended green objects which are thought to be caused by shock-excited H_2 emission in the 4.6 μm *Spitzer* band (e.g., Noriega-Crespo et al. 2004; Beuther et al. 2005; Cyganowski et al. 2008). JWST NIRCam and NIRSpec data now demonstrate that CO ro-vibrational emission can dominate this filter as well (Ray et al. 2023). MIRI provides a wealth of mid-infrared diagnostics to determine the physical structure of high-mass sources, as demonstrated by initial JOYS results (Beuther et al. 2023; Gieser et al. 2023b). Moreover, such data allow one to quantify the relative importance of shocks versus UV radiation in the "feedback" of a high-mass protostar on its immediate surroundings.

Finally, lines of HD starting at $R(4)$ ($E_{\rm up}$ = 1895 K) are also covered and provide together with H_2 constraints on [D]/[H] (e.g., Bertoldi et al. 1999; Wright et al. 1999; Yuan et al. 2012). One puzzle is the depletion of deuterium in denser clouds (Linsky et al. 2006) compared with that seen in the local diffuse interstellar medium. It has been suggested that carbonaceous grains can lock up significant deuterium (e.g., Draine 2006); if so, then this deuterium should be released by strong shocks that destroy grains. The power of JWST MIRI to address this question has recently been demonstrated using JOYS data of both low- and high-mass protostars by Francis et al. (2025). Line images of HD in the nearby HH 211 outflow show strong correlations with shock tracers such as [Fe II] and [S I], but HD/H_2 varies by a factor of four without any clear trends with shock conditions. This is consistent with the conclusion of Caratti o Garatti et al. (2024) that not all grains have been destroyed. The detection of HD in the high-mass IRAS23385+6035 source provides the first measurement of HD/H_2 in the outer Galaxy, at a galactocentric radius of 11 kpc. It falls significantly below the predicted trends from galactic chemical evolution models with radius (e.g., van de Voort et al. 2018), suggesting that there is a significant reservoir of deuterium (such as that in grains) that is not measured by HD.

B.3. Hot cores and dense molecular shocks

Protostars passively heat the gas in their surroundings through gas-dust collisions to a range of temperatures depending on distance from the source. The warm (T > 100 K) inner parts of the collapsing envelopes are called "hot cores." The term "passively heated" distinguishes these hot cores from shock-heated or UV-heated gas.

Millimeter observations have found a rich chemistry to be associated with the hot cores of deeply embedded protostellar sources, from simple to rather complex organic molecules (COMs), i.e., carbon-containing molecules with at least 6 atoms (see reviews by Herbst & van Dishoeck 2009; Jørgensen et al. 2020; Ceccarelli et al. 2023). This section is focused on simple molecules other than H_2 that are detected by mid-infrared emission or absorption lines. This includes molecules such as CO_2, CH_4 and C_2H_2 that cannot be studied by millimeter techniques because they do not have a permanent dipole moment, but that have strong dipole-allowed vibration-rotation transitions. Some of them, most notably CO_2 and CH_4, are major components of interstellar ices (Boogert et al. 2015), but they cannot be formed in large amounts in cold gas. Therefore, they are excellent probes of ice sublimation in hot cores. Other molecules, most notably H_2O, can have contributions from both ice sublimation or sputtering as well as high temperature gas-phase chemistry in shocks (see van Dishoeck et al. 2021, for overview). Sect. 2.2 summarizes other simple molecules that can be studied at mid-infrared wavelengths.

Several of these molecules were first detected at infrared wavelengths by pioneering high spectral resolution ($R \sim 10^5$) ground-based absorption line observations of the brightest high-mass protostars (Evans et al. 1991; Lacy et al. 1989, 1991; Knez et al. 2009). The ISO-SWS and subsequently *Spitzer* detected mid-infrared lines of gaseous CO, H_2O, CO_2, C_2H_2, HCN, CH_4 and SO_2 in a variety of mostly high-mass protostellar sources both in absorption and emission, albeit at much lower spectral resolution than the ground-based data (e.g., Helmich et al. 1996; van Dishoeck & Helmich 1996; Lahuis & van Dishoeck 2000; Boogert et al. 2004; Boonman et al. 2003b; Sonnentrucker et al. 2007) (see also review by van Dishoeck 2004). More recently, high spectral resolution absorption line observations were obtained using EXES on SOFIA and CRIRES on the ESO-VLT but are again limited to the brightest high-mass sources (e.g., Dungee et al. 2018; Barr et al. 2020; Indriolo et al. 2020; Barr et al. 2022; Li et al. 2023). The CS molecule was first detected at infrared wavelengths by Barr et al. (2018). Based on their excitation temperatures and line profiles or velocity offsets, the ground- and space-based studies have suggested a variety of origins of these molecules: hot cores, outflows, and shocks, and even the midplanes of disks around high-mass protostars that are heated by the accretion luminosity.

Notably, JWST can contribute to answering these questions in a variety of ways. First, it has the sensitivity to observe nearby low-mass Class 0 protostars. Its high spatial resolution allows emission lines to be located and to be associated with different physical components. Second, its higher spectral resolution compared with *Spitzer* boosts line/continuum ratios and enables many more detections of molecules in emission, especially in the 5–10 μm range. At R ~3000, MIRI also has enough spectral resolution to detect the gas-phase lines of several important molecules in absorption (e.g., H_2O, CH_4, CO_2, C_2H_2, HCN) and distinguish them from the nearby much broader ice bands (Boogert et al. 1998; Dartois et al. 1998; van Dishoeck 2004). These pencil-beam absorption line-of-sight data provide a unique method to peer deep into the hot cores located close to the protostars compared with beam-diluted emission data at millimeter wavelengths (Boonman et al. 2001). Third, the observation of many individual R- and P-branch lines as well as spectrally resolving the Q-branches, plus detecting ^{13}C isotopologs and hot bands (i.e., transitions between vibrationally excited states), allows for more accurate constraints on excitation temperatures and optical depth of the lines (van Gelder et al. 2024a). Also, MIRI has the ability to disentangle many of the H_2O pure rotational line blends (Banzatti et al. 2023, 2025).

The JOYS overview of molecular lines in low-mass protostars at the source position by van Gelder et al. (2024a) and that in the high-mass protostar IRAS23385 by Francis et al. (2024) highlight all of these aspects. They can test hot core models such as those by Doty et al. (2002); Notsu et al. (2021) that include both ice sublimation as well as high temperature gas-phase chemistry. The SO_2 mid-infrared emission detected by van Gelder et al. (2024b) underlines the importance of taking infrared pumping into account in the excitation. With JWST, also extragalactic hot cores can be studied (Buiten et al. 2025), greatly improving on early *Spitzer* infrared spectroscopic studies of AGN (Lahuis et al. 2007).

At outflow positions offset from the source, the jet shocks plow into dense gas that can produce not just atomic but also molecular emission in the shocked and post-shock gas. Indeed, models of dense $J-$ and $C-$type shocks produce strong H_2, CO, H_2O and/or OH mid- and far-infrared emission (e.g., Draine et al. 1983; Hollenbach & McKee 1989; Kaufman & Neufeld 1996; Flower & Pineau Des Forêts 2010) that has been observed with *Herschel*. *Spitzer*-IRS observations of the HH 211 outflow have detected strong supra-thermal OH emission (see Sect. 2.2) from its bow shock (Tappe et al. 2008, 2012), now also beautifully seen by JWST MIRI-MRS (Caratti o Garatti et al. 2024) in JOYS HH 211 data and in one of the HOPS 370 jet knots in IPA data (Neufeld et al. 2024). This emission is well modeled by photodissociation of H_2O producing OH in very highly excited rotational states (Tabone et al. 2021). The mechanism is further confirmed by the symmetric/antisymmetric line asymmetry, predicted by molecular physics calculations (Zhou et al. 2015), that is also observed in JWST data (Zannese et al. 2024). JWST NIRSpec spectra have confirmed that CO ro-vibrational emission is strong and can outshine H_2 in broadband emission at 4.6 μm (Ray et al. 2023). Investigating at which knot and bow-shock positions this molecular emission is seen, and where not, offers opportunities to test the shock models further and ultimately use the molecular emission as a diagnostic tool, in concert with the results on larger scales from *Herschel* and *Spitzer*.

B.4. Cold outer envelope: Ices

Mid-infrared spectroscopy is unique compared with millimeter and near-infrared data in its ability to probe solid-state features. The central IFU spaxels centered on each source show a rising SED with broad bands of cold ices and silicates superposed in absorption (Fig. 2). These ices are not a minor chemical component; they are actually the main reservoir of the non-refractory carbon and oxygen in cold regions (see Boogert et al. 2015, for review).

MIRI improves significantly on ISO-SWS, *Spitzer* and ground-based telescopes by having the sensitivity to observe the coldest, most ice-rich low-mass Class 0 and the deeply embedded high-mass sources. Also, late-type background stars behind dense clouds can be targeted to reveal the ice content of pre-stellar cores prior to star formation (e.g., Knez et al. 2005; Goto et al. 2021; McClure et al. 2023). Equally important is the fact that, compared with *Spitzer*-IRS, MIRI-MRS has much improved spectral resolving power in the critical 5–10 μm range ($R \sim 3000$ vs $50 - 100$) which is key to resolve and identify weak features. Combined with complementary NIRSpec 3–5 μm data such as part of JOYS+, this will allow for a complete ice inventory.

Pre-JWST mid-infrared spectra have identified primarily simple molecules in ices up to CH_3OH. Some of the weakest ice bands have been suggested to be due to larger organic molecules such as CH_3CH_2OH or CH_3CHO (Schutte et al. 1999; Öberg et al. 2011), but these molecules can only be reliably assigned through a detailed comparison of laboratory ice band profiles with the high-quality spectra that MIRI provides. Recognizing the potential of MIRI in this area, the Leiden Laboratory for Astrophysics has been collecting many laboratory spectra of both simple ices and, recently, more complex molecules in pure and in mixed ice form (e.g., Terwisscha van Scheltinga et al. 2018, 2021; Rachid et al. 2021, 2022; Slavicinska et al. 2023), building on earlier efforts (e.g., Hudgins et al. 1993; Ehrenfreund et al. 1996; Boudin et al. 1998; Mulas et al. 1998; Öberg et al. 2011; Ioppolo et al. 2013). Together, they are collected and made publically available through the *Leiden Ice Database for Astrochemistry* (LIDA) (Rocha et al. 2022) at `icedb.strw.leidenuniv.nl`. Identification of larger ice species would strongly support the view that many complex molecules are actually formed in the ices during the cold pre-stellar and protostellar warm-up phases, rather than solely by high temperature gas-phase chemistry in the hot cores (see reviews by Herbst & van Dishoeck 2009; Jørgensen et al. 2020; Ceccarelli et al. 2023). Using JOYS(+) data for one low- and one high-mass protostar, MIRI-MRS has indeed identified several icy complex molecules demonstrating that they are made in ices (Rocha et al. 2024). Comparison of abundance ratios of complex molecules in ice and gas in the same source for two low-mass JOYS protostars indicates that some molecules are destroyed in the warm gas following ice sublimation, whereas other molecules are not (Chen et al. 2024). Similar analyses using high quality MIRI-MRS data for other low- and high-mass protostars such as provided by the CORINOS and IPA programs (Yang et al. 2022; Nazari et al. 2024a; Tyagi et al. 2025) are in progress.

Ions and salts have long been known to be a significant component of ices (Grim & Greenberg 1987; Grim et al. 1989), with the 4.62 μm band ascribed to OCN^- (Novozamsky et al. 2001) and a significant part of the 6.85 μm band to NH_4^+ (Schutte & Khanna 2003; Boogert et al. 2015). These ions are naturally produced through acid-base reactions between the acid NH_3 and bases such as HNCO and HCOOH; laboratory experiments show that these are thermal reactions that occur even at low temperatures in ices (Raunier et al. 2003; van Broekhuizen et al. 2004). The JWST-NIRSpec detection of the OCN^- ice band in a prestellar core toward a background star confirms this low temperature formation route (McClure et al. 2023). One puzzle, however, is that not enough negative ions have been identified to counterbalance the amount of NH_4^+ in ices implied by the 6.85 μm band. With MIRI, the prospects for identifying the weak and broad features due to other negative ions such as $HCOO^-$ (Schutte et al. 1999) are much improved, and both OCN^- and $HCOO^-$ are indeed now detected in JOYS data (Rocha et al. 2024; Chen et al. 2024). In addition, confirmation of the NH_4^+ identification and balancing the ice charges is highlighted by the combined laboratory and observational study of Slavicinska et al. (2025a), including a likely JWST detection of the main counter ion SH^-. This ion also locks up a significant fraction, up to 20%, of the sulfur budget in dense clouds.

The ice band profiles give information on the ice environment (e.g., whether the molecule is in a water-rich or water-poor environment or whether it has been heated) and thus whether the ice is layered or segregated upon heating (e.g., Pontoppidan et al. 2008; Boogert et al. 2015). Since crystallization processes are irreversible, this also provides a record of the temperature history of the sources, in particular whether they have been heated in the past due to episodic accretion events. A well-known case is that of the 15 μm bending mode of $^{12}CO_2$ (Ehrenfreund et al. 1999; Gerakines et al. 1999; Kim et al. 2012), now also possible with JWST NIRSpec for $^{13}CO_2$ (Brunken et al. 2024a). Moreover, the gas/ice ratio increases with overall envelope heating and thus with evolutionary state (van Dishoeck & Helmich 1996; Dartois et al. 1998; van Dishoeck & Blake 1998). MIRI can compare gas and ice column densities directly for sources where the gas-phase lines are also in absorption, like the JOYS case of B1-c (van Gelder et al. 2024a).

Isotopologs have long been known to be a powerful probe of the physical and chemical structure of the region in which they are residing (see review by Nomura et al. 2023). At low temperatures, the abundances of the heavier isotopes can be enhanced by orders of magnitude through gas-phase reactions. UV photons can also selectively destroy isotopologs such as ^{13}CO, $C^{18}O$ and $^{14}N^{15}N$ (e.g., van Dishoeck & Black 1988; Heays et al. 2014). Now that these isotopes can also be detected in exoplanetary atmospheres (Zhang et al. 2021; Snellen 2025) they may contain information on their formation pathways that cannot be inferred readily by other means (Bergin et al. 2024). JWST-MIRI builds on earlier work (Boogert et al. 2000) by providing high-quality spectra of ^{13}CO and $^{13}CO_2$ that can be used to determine $^{12}C/^{13}C$ isotopolog ratios of ices in cold clouds (McClure et al. 2023) and protostellar envelopes (Brunken et al. 2024b) before they enter the giant planet-forming zones of disks.

For the specific case of water, the MIRI data will be highly complementary to the gaseous water lines obtained from *Herschel* in the WISH and related programs for the same sources (van Dishoeck et al. 2021) (see Sect. B.3). They complement ALMA and NOEMA data on warm gaseous $H_2^{18}O$ emission in the inner envelope (e.g., Persson et al. 2014; Jensen et al. 2019). Together, the data can be used to put together the full picture of the evolution of water (gas *and* ice) from pre-stellar cores to cometary objects, and ultimately provide, through comparison of the deuterium fractionation, further insight into the origin of water in comets and in oceans on Earth. So far, this comparison has been based on gas-phase HDO/H_2O ratios in hot cores assuming that they reflect those in ices, but this does not need to be the case. Direct measurements of HDO/H_2O ice are now possible with JWST. For this reason, a deep NIRSpec spectrum covering the HDO 4.1 μm ice band has been obtained for the most ice-rich solar-mass protostar in the JOYS sample, B1-c. Prior to JWST, there had been upper limits and hints of HDO ice detections (e.g., Dartois et al. 2003; Aikawa et al. 2012), but the first firm detection of HDO ice, toward an intermediate and high-mass protostar, has recently been reported by Slavicinska et al. (2024) as part of the IPA program, demonstrating NIRSpec's ability for this purpose.

Related to the H_2O case is that of O_2 ice. Oxygen is the third most abundant element in space, yet its major reservoirs are still under debate. A long standing problem has been that some fraction of oxygen (up to 50%) may be unaccounted for if an interstellar abundance of 5.8×10^{-4} (Przybilla et al. 2008) is assumed (Whittet 2010; Draine & Hensley 2021) (see recent summary by van Dishoeck et al. 2021): H_2O ice only accounts for about 20% of oxygen in cold regions (Boogert et al. 2015). Models of the chemistry in dense clouds predict that O, O_2 and H_2O are the main volatile oxygen carriers (Tielens & Hagen 1982), with O and O_2 being converted to H_2O ice through hydrogenation on the surfaces of grains (Bergin et al. 2000), processes that have been confirmed in the laboratory (Miyauchi et al. 2008; Ioppolo et al. 2008). However, under certain conditions O_2 ice could become a significant reservoir. Indeed, cometary data of 67P show a surprisingly high and constant O_2/H_2O ice ratio of a few % (Bieler et al. 2015; Rubin et al. 2019).

O_2 is notoriously difficult to observe both in the gas and in ice. As a symmetric molecule, it does not have a permanent dipole moment and can only be observed in the gas through its much weaker magnetic dipole transitions from space or its much less abundant $^{16}O^{18}O$ isotopolog from the ground. While O_2 gas has been detected at low abundances at a few PDR and shock positions (Goldsmith et al. 2011; Liseau et al. 2012), *Herschel*-HIFI deep searches have mostly obtained upper limits including a fractional abundance as low as 6×10^{-9} for the NGC 1333 IRAS4A source that is part of JOYS(+) (Yıldız et al. 2013). Even in the inner hot core of the COM-rich IRAS 16293-2422B source, the gaseous O_2 abundance appears to be less than 10^{-6}, thus containing only a small fraction of oxygen (Taquet et al. 2018). One possible explanation for its absence in hot cores could be the presence of X-rays destroying O_2 following its sublimation around 30 K (Notsu et al. 2021). This suggests that O_2 ice could still be present in the coldest parts of protostellar envelope which JWST MIRI can search for.

B.5. Embedded disks

Disks around low-mass young T Tauri stars have been studied in great detail over the last decades and much has been learned about their physical and chemical structure (see reviews by Dullemond et al. 2007; Miotello et al. 2023; Manara et al. 2023; Öberg et al. 2023). In contrast, little is still known about the physical and chemical properties of disks in the embedded phase. It is well established theoretically that disks must form by the Class 0 stage as the inevitable byproduct of the collapse of a rotating core and observationally from the fact that all Class 0 sources drive collimated jets. Much of the observational difficulties stem from the fact that the emission from the disk is readily overwhelmed by that from the surrounding envelope if observed at too low spatial resolution and sensitivity to image minor isotopologs. With ALMA, this situation is rapidly changing and embedded disks can now be detected through Keplerian rotation of CO isotopolog lines (e.g., Murillo et al. 2013; Yen et al. 2017). An overview is presented in Tobin & Sheehan (2024). The recent eDisk ALMA survey of embedded disks at 0.04″ (down to 7 au) resolves also the millimeter dust emission showing elongated disk images (Ohashi et al. 2023). Some of the eDisk sources are part of JOYS.

Embedded disks are warmer than mature Class II disks (van't Hoff et al. 2020), with fresh material that can be brought through accretion streamers onto the disk (e.g., Pineda et al. 2020; Murillo et al. 2022; Hsieh et al. 2023; Cacciapuoti et al. 2024; Valdivia-Mena et al. 2024; Podio et al. 2024; Speedie et al. 2025). One specific goal of the MIRI program will be to search for signs of compact accretion shocks that could be revealed by H_2, atomic lines (e.g., [S I]) and other shock tracers centered on the source. Indeed, models of accretion shocks predict a rich spectrum of CO, H_2O and OH lines (Neufeld & Hollenbach 1994). Accretion shocks have been suggested based on millimeter observations of SO and SO_2 molecules (Sakai et al. 2014; Artur de la Villarmois et al. 2019, 2022; Liu et al. 2025). The shock (its velocity) is a direct measure of where most of the material enters the disk, although at only a few km s^{-1} this will be too low to measure with JWST. The strength of the shock and inflow of envelope material, in turn, have consequences for the thermal and chemical structure of the young disk, in particular whether pristine pre-stellar core material can be preserved during the transport from cloud to disk or whether the chemistry is reset (e.g., Visser et al. 2009). The mid-infrared detection of SO_2 on disk scales with JWST as part of JOYS+ (van Gelder et al. 2024b) could be a signature of an accretion shock, although the line width and velocity measured with ALMA suggest that thermal sublimation of SO_2 ice in a hot core is more likely.

ALMA studies provide insight into the outer parts of embedded disks, but infrared studies are needed to probe the innermost regions (<1 au) that ALMA cannot reach. Mature Class II disks show surprisingly rich mid-infrared spectra with *Spitzer* (Carr & Najita 2008; Salyk et al. 2008; Pontoppidan et al. 2014) that may differ for very low mass stars (Pascucci et al. 2013). This is even more apparent now with JWST (e.g., Grant et al. 2023; Kóspál et al. 2023; Banzatti et al. 2023; Gasman et al. 2023; Henning et al. 2024; Pontoppidan et al. 2024b; Temmink et al. 2024a; Romero-Mirza et al. 2024; Colmenares et al. 2024), with disks around very low mass stars showing a wide variety of hydrocarbon molecules (Tabone et al. 2023; Xie et al. 2023; Arabhavi et al. 2024). Mid-infrared lines from H_2O, HCN, C_2H_2, CO_2 and OH are commonly seen, indicating hot molecular gas at temperatures of 300–900 K arising from the inner few au, i.e., the terrestrial planet-forming zones of the disks. This hot gas is also probed by pioneering velocity resolved ($R = 20000 - 100000$) ground based CO infrared spectra (e.g., Najita et al. 2003; Blake & Boogert 2004; Salyk et al. 2009; Brown et al. 2013; Banzatti & Pontoppidan 2015; Banzatti et al. 2022; Temmink et al. 2024b). Various atomic transitions, most prominently the [Ne II] 12.8 μm line, have been studied as well pre-JWST (e.g., Pascucci et al. 2007; Güdel et al. 2010). An interesting question is therefore whether young disks in the embedded phase have similarly rich spectra as the more evolved disks that probe the inner few au. Existing *Spitzer* data had too low feature/continuum and spatial resolution to address this question (Lahuis et al. 2006, 2010) but VLT-CRIRES data show strong 4.7μm CO emission lines from embedded Class I protostars that indicate Keplerian rotation and are thus promising for JWST studies of other molecules (Herczeg et al. 2011). However, the JWST molecular line survey of the JOYS low-mass protostars by van Gelder et al. (2024a) suggests that emission from inner disks is not commonly seen.

The question whether high-mass protostars have disks has been debated as well, although it is likely they do too, since they all show collimated jets and outflows (Beltrán & de Wit 2016; Beuther et al. 2025). Their characterization is even more difficult since they are all hidden by huge amounts of extinction. Millimeter interferometer studies have revealed elongated disk-like structures around the massive protostars with signs of Keplerian motion (e.g., Cesaroni et al. 2005; Ilee et al. 2018; Maud et al. 2019; Johnston et al. 2020; Williams et al. 2022) (see review by Beltrán & de Wit 2016). Radiation transport studies provide some information on the density structures of the underlying disks (Fallscheer et al. 2011) and make predictions of expected mid-infrared structures. Obviously, the mid-infrared data trace completely different structures than the millimeter images, and important additional parameters that could be obtained in the mid-infrared regime include the vertical disk structure or the disk flaring, if the emission were spatially resolved.

As for the low-mass disks, the spectroscopy will allow for investigation into several other properties of the embedded disks, in particular the temperature, ionization state, and chemical composition. Indeed, ground-based CO $v = 2 - 0$ overtone emission at 2.3 μm has been detected with high resolution spectroscopy and infrared interferometry. The data are indicative of a disk origin coming from inside the dust sublimation radius (Carr 1989; Bik & Thi 2004; Ilee et al. 2014; GRAVITY Collaboration 2021). Compared with previous mid-infrared studies, the higher spatial resolution JWST MIRI spectra will be much less beam diluted and could therefore pick up disk emission. The higher spectral resolution of MIRI-MRS also helps to boost the line-to-continuum ratio. Indeed, the relatively cool CO_2 emission seen toward the high mass protostar IRAS 23385+6053 in JOYS data could arise from the cooler outer surface of a massive disk (van Dishoeck et al. 2023) although other interpretations such as a hot core are also possible (Francis et al. 2024).

B.6. JOYS studies

Early JOYS publications on selected topics or individual sources are discussed in Sections 4–8 and are briefly summarized here. They include a study on the atomic and molecular lines in the high-mass protostar IRAS 23385+6053 by Beuther et al. (2023); Gieser et al. (2023b); Francis et al. (2024); on the linked accretion and ejection in the Class I binary protostar TMC-1 by Tychoniec et al. (2024); and on the analysis of ices including the detection of complex molecules and sulfur-bearing salts by Rocha et al. (2024); Chen et al. (2024); Slavicinska et al. (2025a). Moreover, van Gelder et al. (2024a) provides an overview of detected gaseous molecular lines at the central position of all JOYS sources. An early comparison with Class II sources is provided by van Dishoeck et al. (2023).

The HH 211 outflow imaged with NIRCam has been highlighted by Ray et al. (2023), whereas the MIRI-MRS large mosaic taken as part of JOYS is analyzed in Caratti o Garatti et al. (2024). A survey of HD and HD/H_2 in HH 211 and other sources with galactocentric radius is published by Francis et al. (2025).

The L1527 outflow has been studied both within JOYS and in PID 1798 (PI J. Tobin). This is a rare case in which the jets are characterized by the presence of double peak emission in forbidden emission lines with a low and high velocity component, but with no such signature in molecular emission (Devaraj et al., in prep.; Drechsler et al., in prep.). The low velocity components are thought to be excited by shocks at the outflow cavity wall by interaction of the disk wind with the ambient medium. The high velocity component is excited by the fast moving jet inside the low-density cavity where no molecular material is present anymore to be entrained by the fast moving flow.

JOYS+ publications include the mid-infrared detection of gas-phase SO_2 (van Gelder et al. 2024b); the analysis of NIRSpec observations of the Serpens S68N binary protostellar system (Le Gouellec et al. 2025); a combined JWST-MIRI + ALMA analysis of the fascinating WL20 triple system with aligned disks and jets in Ophiuchus (Barsony et al. 2024); and a determination of the $^{12}C/^{13}C$ ratio in ices (Brunken et al. 2024b). Together, these JOYS(+) papers demonstrate the rich and diverse science that can be done with a single protostellar data set.

Appendix C: Simultaneous MIRI imaging

C.1. Protostars in the outer Galaxy

The simultaneous off-source image at 15 μm obtained for IRAS 23385+6053 at a Galactocentric radius of 11 kpc is presented in Figure C.1. Since the MRS on-source observation consisted of a 2 × 2 mosaic as well as a background pointing, the simultaneous MIRI image is a composite of two off-source pointings, a southern and northern region. The southern region has 3 exposures of 200 seconds each, and the northern region is a mosaic of 4 images, with each 3 exposures of 200 seconds. Thus, the northern image is significantly deeper than the southern one. The resulting rms values, after subtraction of a median background of 0.14 MJy sr^{-1}, are 0.4 (north) and 3.8 (south) MJy sr^{-1}, respectively.

Using the aperture photometry method, 47 point sources were found, after discarding doubles, false positive detections or bad pixels. The high spatial resolution of MIRI now allows point sources to be distinguished from the extended bright background. SEDs were made using near-infrared observations of 2MASS and WISE at the shorter wavelengths at the MIRI positions, see Figure C.2 for one example. A rising SED between 2 and 15 μm was used as a criterion to identify embedded protostars, as done in Greene et al. (1994) between 2 and 10 μm. For the source shown in Figure C.2, the spectral slope α_{2-15} is > 0.46 taking into account that the 15 μm MIRI data point is a lower limit due to saturation. The integrated luminosity is at least 450 $L_\odot$, suggesting indeed an intermediate or high mass source, but the lack of data longer than 15 μm prevents assessing the total luminosity of these sources and quantities such as $T_{\rm bol}$. This source was highlighted in the image accompanying the press release of Rocha et al. (2024) at `webbtelescope.org/contents/news-releases/2024/news-2024-111`.

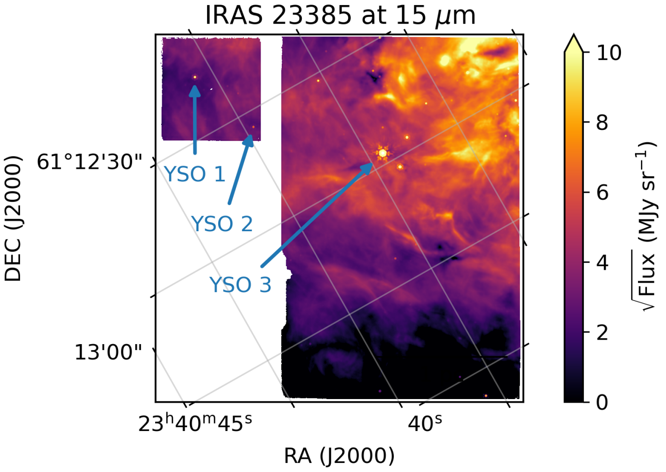

Fig. C.1. Simultaneous MIRI 15 μm imaging near the young high-mass cluster IRAS 23385+6053 at a galactocentric distance of 11 kpc. Its coordinates are 23:40:49.18, +61:11:22.86.

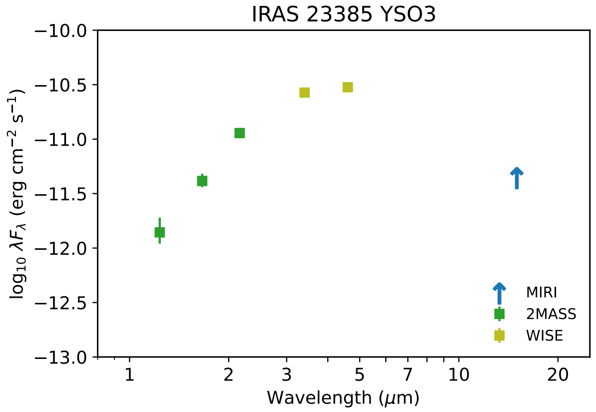

Fig. C.2. Spectral energy distribution of a candidate embedded protostar in the outer Galaxy found by simultaneous MIRI imaging.

Other MIRI point sources have α values closer to zero or negative, suggesting that they are more evolved sources. This example serves as an illustration of JWST-MIRI's capabilities to detect new protostars in highly extincted distant and crowded regions.

C.2. Role of PAH emission affecting ice bands

The MIRI spectra and SEDs may also contain signatures of PAHs. MIRI has the sensitivity to detect these features throughout a cloud. At the position of deeply embedded sources, PAH features were largely undetected with ISO for high-mass protostars (e.g., Gibb et al. 2004) (unless associated with well-known PDRs such as Orion), and with *Spitzer* for low-mass protostars (Geers et al. 2009). Likely explanations include freeze-out into ices and coagulation to larger PAH systems that do not emit, rather than a lack of UV radiation to excite them. With JWST's much higher sensitivity, PAH emission may be seen both on and off source, however.

The case of IRAS 23385+6053 provides a particularly illustrative example of how this emission can complicate the analysis of broad ice features in the spectrum. Likely, the PAH emission, which is clearly seen at 11.3 μm (Beuther et al. 2023), comes from a background cloud and is extincted by ices in the dense envelope surrounding the high-mass protostellar cluster. This makes the 6.2 and 7.7 μm features hard to detect and they can distort the ice bands. This case serves as a warning for detailed analysis of ice bands in high-mass sources.

Appendix D: Mass loss rate determinations and shock model comparison

To obtain more quantitative information on the physical parameters and jet properties of SMM3, we follow the analysis methods of Caratti o Garatti et al. (2024) for HH 211 in slightly modified form. Rather than using [Fe II] and [S I] line ratios, we take the [Ne II] and [S I] line fluxes to constrain shock characteristics. Figure D.1 compares the observed extinction-corrected [Ne II] 12.8 μm and [S I] 25 μm fluxes from spectra extracted at the red knot position with the shock models of Hollenbach & McKee (1989). Assuming that all of the line emission comes from such dissociative shocks, the [Ne II] line constrains the shock velocity to 40 – 45 km s^{-1}, whereas the [S I] flux suggests the pre-shock total hydrogen density $n_0(\mathrm{H} + 2\mathrm{H}_2)$ to be ~ 10^5 cm^{-3} (red lobe). The mass loss rate indicated by the atomic lines is then

$$\dot{M}_{\rm atomic} = \mu m_{\rm H} n_0 \pi r_j^2 v_{\rm tot}, \tag{D.1}$$

where μ is the mean atomic weight (1.35), $m_{\rm H}$ is the proton mass, r_j is the jet radius, measured to be ~60 au from the jet diameter at the shortest wavelengths where the MIRI angular resolution is the highest and sufficient to resolve the width. The total velocity $v_{\rm tot}$ of ~50 km s^{-1} is obtained from the measured jet velocity of ~30 km s^{-1} (from ionic lines and from ALMA CO data in the jet), corrected for an inclination of ~ 50^o estimated from CO millimeter maps (Yıldız et al. 2015). The inclination could be higher by 10-15^o as estimated from the ALMA continuum disk image, but is unlikely to be lower. This formula gives a typical mass loss rate of $\dot{M}_{\rm atomic} = 4.5 \times 10^{-8}$ M$_\odot$ yr^{-1} for the red lobe.

An alternative route to getting the mass outflow rates is to use the flux of the [O I] 63 μm line, which is the main coolant of the jet (Hollenbach 1985). Using the measured [O I] 63 μm flux from *Herschel*-PACS of 1×10^{-2} L$_\odot$ summed over the ~9″ spaxels where the line is detected gives a mass loss rate $\dot{M}$ of ~ $(0.6 - 1) \times 10^{-6}$ M$_\odot$ yr^{-1} (Mottram et al. 2017; Karska et al. 2018), significantly higher than the value inferred above.

Watson et al. (2016) found that the [Fe II] 26 μm ground state fine structure line can be used as a proxy for [O I] through the following relation:

$$\dot{M}_{\rm atomic} = 1.4 \times 10^{-3} L(\mathrm{Fe}\ 26\mu\mathrm{m})/L_\odot. \tag{D.2}$$

Using the extinction corrected 26 μm [Fe II] luminosities of 3.5×10^{-6} and 7.5×10^{-6} L$_\odot$ for the red- and blue-shifted positions where H$_2$ was extracted gives mass loss rates of $\dot{M}_{\rm atomic}$ = 0.5×10^{-8} and 1.1×10^{-8} M$_\odot$ yr^{-1}, respectively, more in line with those found from [Ne II] + [S I]. However, these values seem low compared with the *Spitzer* studies by Watson et al. (2016) using this line, also given the significant luminosity of SMM3, but this could be due to the much smaller area over which the [Fe II] line flux is measured compared with *Spitzer* data. Summing over the entire ~ 7″ × 7″ MRS channel 4 FoV (comparable to the *Spitzer*-IRS aperture) gives an extinction-corrected [Fe II] 26 line luminosity of 6.1×10^{-5} L$_\odot$, which translates to $\dot{M}_{\rm atomic} = 8.6 \times 10^{-8}$ M$_\odot$ yr^{-1}. This value is indeed significantly higher than that derived for a single position, but is still an order of magnitude lower than that derived from [O I]. A similar difference was found for HH 211.

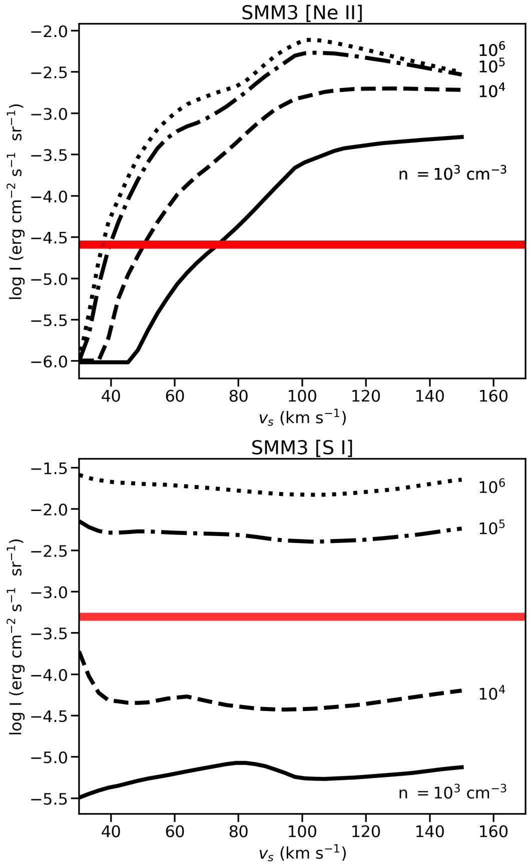

Fig. D.1. Comparison of the extinction-corrected [Ne II] 12 μm and [S I] 25 μm fluxes for SMM3 in the red outflow lobe with shock models of Hollenbach & McKee (1989) as function of shock velocity and pre-shock density. The red horizontal bars indicate the observed values for the red lobe of SMM3.

We note that the [O I] determination should be considered as an upper limit for various reasons. The Hollenbach (1985) model assumes a single knot, whereas there may be many more in the beam, as is known for the case of SMM3 (Tychoniec et al. 2021) (Le Gouellec et al., in prep.). For the case of SMM3, the [O I] 63 μm flux is also likely affected by extended emission from the nearby SMM6 source in the large *Herschel*-PACS aperture: the peak [O I] emission indeed seems somewhat off centered from the SMM3 source position (Karska et al. 2013). Finally, optical depth and foreground absorption of the [O I] 63 μm line can also affect the estimate. In summary, this example illustrates the uncertainties and pitfalls associated with the different methods and the need to recalibrate some of the relations for the higher spatial resolution data provided by JWST.

Table D.1. Overview of mid-infrared lines commonly detected in protostellar systems.

Species	Transition $u-l$	λ (μm)	E_u/k (K)	Type[a]	Origin
[Fe II]	$a^4F_{9/2}$-$a^6D_{9/2}$	5.3402	2694	R	Jet
	$a^4F_{7/2}$-$a^4F_{9/2}$	17.9232	3496		Jet
	$a^4F_{5/2}$-$a^4F_{7/2}$	24.5019	4083		Jet
	$a^6D_{7/2}$-$a^6D_{9/2}$	25.9884	554		Jet, Entrained gas
[Fe I]	$^5D_3$-$^5D_4$	24.0423	600	R	Jet
[Ni II]	$^2D_{3/2}$-$^2D_{5/2}$	6.6360	2168	R	Jet
[Ne II]	$^2P_{1/2}$-$^2P_{3/2}$	12.8135	1123	V	Jet, Photoionized gas
[Ne III]	$^3P_1$-$^3P_2$	15.5551	925	V	Jet, Photoionized gas
[Ar II]	$^2P_{1/2}$-$^2P_{3/2}$	6.9853	2060	V	Jet, Photoionized gas
[S I]	$^3P_1$-$^3P_2$	25.2490	570	SR	Jet, Wind?
H_2[b]	S(1)	17.0348	170	V	Wind, Entrained gas
	S(5)	6.9095	2504	V	Wind, Jet
CO	$v = 1-0 \geq$P(24)	4.9–5.2	4600–8000	V	Jet, Shock[d]
H_2O	v_2=1-0 rovib	5.5–7.5	2300–>4000	V	Shock, Hot core[d]
	v=0-0 warm	11–18[c]	2600–>8000	V	Shock, Hot core[d]
	v=0-0 cold	20–27[c]	1100–4000	V	Hot core[d]
CO_2	v_2=1-0	14.4–15.6	960–1500	V	Hot core[d], Outflow
HCN	v_2=1-0	13.5–14.5	1000–1500	V	Hot core[d]
C_2H_2	v_5=1-0	13.0–14.5	1000–2000	V	Hot core[d]
OH	v=0-0	9–27	10000–40000	V	Shock, UV-irradiated gas[d]

[a] R=Refractory, SR=Semi-Refractory, V=Volatile.

[b] Only some example H_2 lines in v=0 are listed

[c] Lines from warm H_2O also at longer wavelengths

[d] Some contribution from young disk possible in Class I sources

Appendix E: Which line traces what?

Table D.1 summarizes the commonly observed mid-infrared lines in protostellar systems and their proposed origin based on the JWST data.

Appendix F: IRAS 18089 continuum, silicate, and H_2O ice subtraction

In order to analyze the 7–9 μm range for absorption of various ices, first the continuum and silicate features need to be subtracted from the IRAS 18089 spectrum presented in Fig. 21. The method consists of applying the following equation to simultaneously fit both components

$$F = F_0 \exp(-\tau_{\rm dust}) + F_{\rm cold}, \tag{F.1}$$

where F_0 is assumed to be a blackbody emission with a temperature of 700 K, originating from the warm envelope region. $\tau_{\rm dust}$ is the optical depth from the dust along the line of sight, which is given by $\tau_{\rm dust} = \rho_{\rm dust}\kappa_{\rm dust}$, where $\rho_{\rm dust}$ is the dust column density in cm^{-2} g, and $\kappa_{\rm dust}$ is the dust mass absorption coefficient in cm^2 g^{-1}. Finally, an additional source of emission coming from a cold envelope at T = 35 K is used to fit (by eye) the spectrum at wavelengths above 20 μm where cold dust emission starts playing a major role.

The dust properties used in this paper follow previous studies by Sargent et al. (2009); Boogert et al. (2008); McClure et al. (2023) and Rocha et al. (2024). They consist of adopting olivine ($MgFeSiO_4$) and pyroxene ($Mg_{0.7}Fe_{0.3}SiO_3$) stoichiometries as representative of the dust. The optical constants of these materials were taken from Dorschner et al. (1995). In addition, a grain-shape correction was performed by adopting a distribution of hollow spheres (DHS Min et al. 2005), and a size distribution ranging from $a_{\rm min}$ = 0.1 μm to $a_{\rm max}$ = 1.0 μm. The calculations of the dust opacities with those properties are executed with the OpTool software (Dominik et al. 2021).

Figure F.1 (top) shows the continuum and silicate absorption profiles for IRAS 18089. The contributions of the two silicate (pyroxene + olivine) bands at 9.7 and 18 μm are seen. The 9.7 μm absorption is slightly overestimated in the model to account for the excess between 8 and 9 μm. Part of this missing absorption at 9–10 μm may be due to some superposed silicate emission from an inner warm envelope or disk. Since our primary interest is in the 7–9 μm range, the precise details do not matter. The 18 μm band matches well the observations but the long wavelength wing is overpredicted by the model. This is compensated by the cold blackbody emission above 20 μm.

Once the continuum and silicate are estimated, the spectrum is converted to an optical depth scale using the equation $\tau = -\ln(F_{\rm obs}/F_{\rm cont})$, where $F_{\rm obs}$ is the observed flux and $F_{\rm cont}$ is the continuum flux which in this approach includes the silicate absorption profile. The result is presented in Figure F.1 (bottom).

Based on this continuum model with the silicate features, we obtain $\tau_{9.7}$ = 9.2. Assuming an extinction law similar to dense star-forming regions in Perseus ($A_V = 28.6 \times \tau_{9.7}$, Boogert et al. 2013), the derived visual extinction is A_V ~263 mag (see Appendix G for more details). While such a huge extinction correction would be required for any emission features arising from the inner region (see van Gelder et al. 2024a, for a detailed discussion), this is not the case for absorption bands from the ices/dust. For example, independent analyses of L−band spectra from protostars in the Serpens molecular cloud were performed by Pontoppidan et al. (2004) with extinction correction

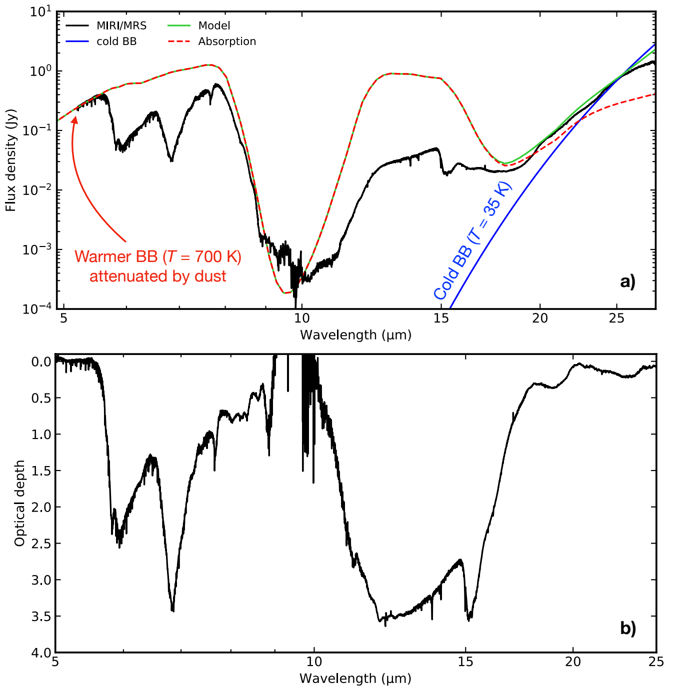

Fig. F.1. Spectrum of IRAS 18089 before and after global continuum and silicate subtraction. Panel a (top) shows the simplified model for IRAS 18089 given by a warm (red line) and cold (blue line) blackbody emission. Panel b (bottom) displays the optical depth scale of IRAS 18089 with both continuum and silicate subtracted.

and Perotti et al. (2020) without correction. Both methods result in equivalent optical depths after continuum removal.

The next step is to fit and remove the H_2O ice features. In the MIRI range, H_2O ice has two prominent and broad features, the bending mode around 6 and the libration mode at 12 µm. Similarly to the dust properties, the analysis of the H_2O ice features has been performed using a distribution of grain-shape corrected spectra adopting the DHS approach and different temperatures to account for the temperature gradient of the source. The result is presented in Figure F.2. The fit using particles ranging from 0.1 to 1.0 µm in size is indicated by the gray line. Despite the good fit to the short wavelength range of the 12 µm band, it leaves a strong absorption excess unexplained at longer wavelengths. For this reason, we considered an additional size distribution of larger grains, ranging from 1.0 to 2.0 µm. In particular, we assumed that the hot ice (160 K) component is dominated by smaller grains, whereas the cold ice (15 K) is represented by larger grains. In this combined case, the fit is equally good at short wavelengths and reduces the excess at longer wavelengths.

The fit to the various ice features in the 7–9 µm range is presented in Figure 22. The fit to the 6.85 µm feature, consisting of both NH_4^+ and CH_3OH ice, is contained in Figure F.4. Following Slavicinska et al. (2025a), ammonium hydrosulfide salt NH_4SH provides the best fit to the feature; the adopted band strength is 3.6×10^{-17} cm molecule^{-1}. This allows us to quantify the N-budget in ices. In this calculation, the overall N abundance is assumed to be 6.3×10^{-5} (Przybilla et al. 2008) and the total hydrogen column along the line of sight $N_{\rm H}$ = 3.6×10^{23} cm^{-2} based on the above extinction A_V=263 mag and $N_{\rm H}/A_V$ = 1.37×10^{21} cm^{-2} mag^{-1} (Evans et al. 2009).

Table F.1 summarizes the column densities of the molecules used to produce the fit in Figures 22 and F.4. The column density used to fit the newly detected 8.38 µm feature will be presented in a future paper dedicated to the analysis of this band (Rocha et al., in prep.).

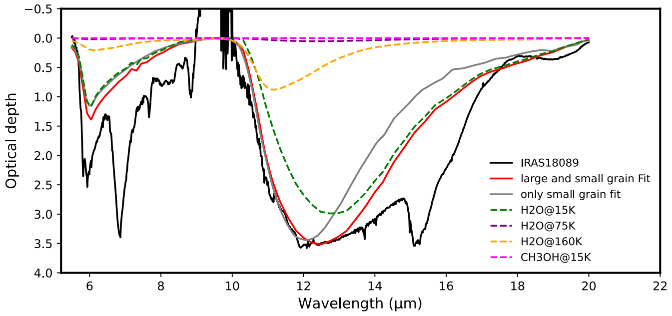

Fig. F.2. Simplified H_2O ice model for IRAS 18089 after subtraction of the global continuum and silicate band. The small-grain only fit is indicated by the gray line, and the combined (large and small) grain population is shown by the red line. The dashed lines show the H_2O ice components for the combined population model.

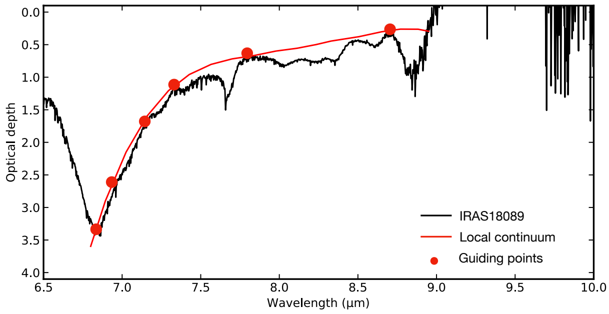

Fig. F.3. Local continuum fit and guiding points for the 7–9 µm range of the IRAS 18089 spectrum, after subtraction of the global continuum, silicate feature and water libration band.

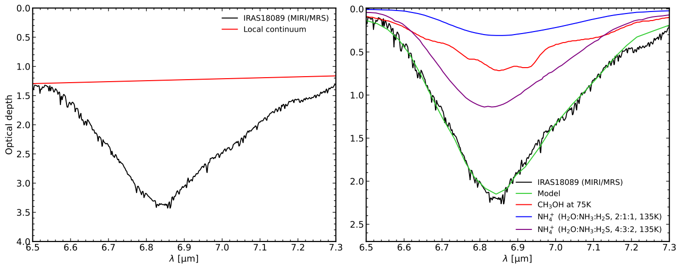

Fig. F.4. Ice features at 6.85 µm toward IRAS18089. The left panel shows the local continuum subtraction, and the right panel displays the best fit and the individual NH_4^+ components and warm CH_3OH ice.

Appendix G: Extinction determinations

Most lines and diagnostics require a correction for extinction, which is substantial for these deeply embedded sources. As discussed in detail by van Gelder et al. (2024b,a) the correction consists of two parts: (i) an absolute extinction ($\tau_{\rm dust}$) based on an extinction law; and (ii) differential extinction caused by various ice absorption bands and silicates ($\tau_{\rm ice,silicates}$) at specific wavelengths.

Several formulations of the extinction law exist in the literature (e.g., Weingartner & Draine 2001; Gordon et al. 2023); they are usually optimized for diffuse cloud dust from UV to infrared and include already some form of silicate absorption. The JOYS+ papers to date use either the McClure (2009) law or the

Table F.1. Ice column densities corresponding to the best fit of the IRAS 18089 spectrum.

Species	Name	N (10^{17} cm^{-2})
H_2O	water	282.3 ± 70.5
CH_4	methane	5.3 ± 1.3
SO_2	sulfur dioxide	0.3 ± 0.1
OCN^-	cyanate ion	5.3 ± 1.5
NH_4^+	ammonium ion	33.0 ± 4.0
$HCOO^-$	formate ion	1.1 ± 0.3
H_2CO	formaldehyde	28.2 ± 7.1
CH_3OH	methanol	50.4 ± 12.7
HCOOH	formic acid	2.9 ± 0.7
CH_3CHO	acetaldehyde	1.9 ± 0.5
CH_3CH_2OH	ethanol	4.2 ± 1.1
CH_3OCHO	methyl formate	0.9 ± 0.2
CH_3COOH	acetic acid	<2
CH_3OCH_3	dimethyl ether	2.8 ± 0.7
CH_3COCH_3	acetone	0.7 ± 0.2

Pontoppidan et al. (2024a) law (KP5), which have been developed for the mid-infrared extinction due to dust in dense clouds. The KP5 relation contains also some generic ice features and has a deeper silicate absorption than the McClure (2009) law.

In the JOYS+ papers, the local ice extinction is usually estimated from the observed spectrum itself and can be substantial: for example, the gaseous CO_2 $P-$branch lines can be fully extincted by the CO_2 ice band, but this does not hold for the $R-$branch lines (Francis et al. 2024). This example also illustrates that the appropriate extinction to use depends on the origin of the emission. For example, hot core emission from molecules such as CO_2 and H I recombination lines originating close to the protostellar embryo experience more extinction than lines coming from an outflow cavity.

One way to determine the absolute extinction in units of A_K or A_V is to use one of the above global extinction laws, following the procedure as described in, for example, Appendix C of van Gelder et al. (2024b). There are at least three other methods that can and have been adopted. The first method is to measure just the optical depth of the silicate feature at 9.7 µm, $\tau_{9.7}$, which represents the total extinction along the line of sight to the dust sublimation radius, very close to the protostellar embryo. Its relation with A_K has been well calibrated by comparing $\tau_{9.7}$ from *Spitzer* spectra against extinction measurements of reddened background stars behind dense clouds. Boogert et al. (2013) (their equations (4) and (5)) find that the relation changes between diffuse cloud ($A_V \lesssim 10$ mag) and dense cloud dust in the Lupus star-forming region. These relations have more recently been confirmed for other clouds by Madden et al. (2022). Assuming A_V/A_K=7.7 as appropriate for $R_V = 5.5$ (Cardelli et al. 1989), the Boogert et al. (2013) diffuse cloud relation leads to $A_V = 18.5 \times \tau_{9.7}$. For dense cloud dust, it becomes $A_V = 28.6 \times \tau_{9.7}$. The latter relation is appropriate for deeply embedded low-mass Class 0 and high-mass sources, and has indeed been used for IRAS 18089 in Appendix F. Class I sources have lower extinctions but generally still well above 10 mag. However, use of the dense cloud relation has been found to lead to unreasonably high accretion rates, and hence the diffuse cloud relation is adopted for Class I sources in Sect. 4.2.

A second, related method is to use the observed relations of ice optical depths with A_V (Whittet et al. 2001; Boogert et al. 2015). The best-known relation is that of the 3 µm water ice feature, $\tau_{3.0}$, versus A_K calibrated by Boogert et al. (2013); Madden et al. (2022) for dense clouds. Since the 3 µm ice band is often saturated in the most deeply embedded JOYS+ sources, an alternative is to use the 15 µm CO_2 ice band τ_{15} (Bergin et al. 2005; Whittet et al. 2009) which can now be readily observed with JWST. Further calibration of the τ_{15} versus A_K relation for dense clouds is warranted.

A third measure of the extinction can be obtained from the excitation of H_2: rotational diagrams using lines in the MIRI wavelength range show that the S(3) line flux at 9.66 µm clearly falls below that of the neighboring H_2 lines due to enhanced silicate extinction, as has also been found in ISO and *Spitzer* data. Various papers show how both the extinction and the H_2 OPR can be fitted simultaneously to H_2 rotation diagrams to obtain a value of $\tau_{S(3)}$ which can then be converted to A_V using an extinction law (e.g., Neufeld et al. 2006; Giannini et al. 2011; Francis et al. 2025; Okoda et al. 2025). This extinction value should be appropriate for any emission lines originating from the outflow and its cavity. If NIRSpec data are available, one can add higher excitation H_2 lines at shorter wavelengths to this analysis.

A more effective way to use NIRSpec data may, however, be to obtain an extinction estimate from atomic or molecular lines lines that originate from the same upper level; the MIRI range does not contain line pairs that can readily be used for this purpose. The intrinsic ratio of these line pairs depends only on their Einstein A values and frequencies, so the difference between observed and theoretical flux ratios directly gives the local reddening at the corresponding wavelengths. For H_2, the 1–0 S(1) line at 2.12 µm and 1–0 O(5) line at 3.23 µm are a well-known line pair that can be used for this purpose: entire outflow extinction maps can even be obtained using narrow-band filters containing these lines with NIRCam (Ray et al. 2023; Caratti o Garatti et al. 2024). Similarly [Fe II], H I or other atomic lines originating from the same upper level in the 0.4–2 µm range can be useful extinction tracers in regions that are not too extincted (e.g., Giannini et al. 2015). We note that for JOYS+ sources, high spectral resolution NIRSpec data are limited to >3 µm. Assani et al. (2025) have recently introduced a procedure for comparing extinction estimates from [Fe II] NIRSpec and MIRI data that warrants further exploration.

As noted in Appendix F, no extinction correction is applied to absorption features of ices or silicates since they directly measure the column along the line of sight. Molecular absorption lines originating in hot core gas lying interior to the outer icy envelope would require an extinction correction, but in practice only the differential correction due to ices (e.g., the CO_2 gas + ice case) has been applied in the JOYS papers (e.g., van Gelder et al. 2024a). Also, a covering fraction of unity by the absorbing material is assumed (see also Sect. 3.5). Since the main interest is in relative column density ratios, rather than absolute ones, this should not change significantly any conclusions unless the lines are heavily saturated.

In this paper all of these methods to determine extinction have been used, often to be consistent with earlier JOYS papers. A systematic comparison between them is left for a future study. It should be noted that differences in absolute values of, most notably, accretion rates can be substantial depending on the adopted method.